UNIVERSITÄT ZU LÜBECK

From the Institute of Robotics and Cognitive Systems
of the University of Lübeck
Director: Prof. Dr. rer. nat. habil. Floris Ernst

Force Sensitive Robotic Ultrasound for Diagnostics and Therapy of Peripheral Arterial Disease

Dissertation
for Fulfillment of
Requirements
for the Doctoral Degree
of the University of Lübeck

from the Department of Computer Sciences and Technical Engineering

Submitted by
Jonas Osburg
from Waiblingen

Lübeck, 2025

First Referee: Prof. Dr. rer. nat. habil. Floris Ernst

Second Referee: Prof. Dr. Georg Schildbach

Date of oral examination: 24th November 2025

Approved for printing. Lübeck, 25th November 2025

KURZFASSUNG

Die periphere arterielle Verschlusskrankheit (pAVK) ist eine der häufigsten Herz-Kreislauf-Erkrankungen, von der weltweit mehr als 230 Millionen Menschen betroffen sind. Dabei handelt es sich um eine Gefäßerkrankung, bei der die Arterien, meist in den Beinen, durch Ablagerungen verengt oder verschlossen sind. Dies führt zu einer reduzierten Durchblutung, was im weiteren Verlauf Gewebeschäden verursachen kann. Eine frühzeitige Diagnose ist entscheidend, um das Fortschreiten der Erkrankung zu verhindern, die Lebensqualität der Patienten zu erhalten und schwerwiegende Komplikationen zu vermeiden. Die Prävalenz der pAVK nimmt mit zunehmendem Alter stark zu, was insbesondere in Industrieländern mit einer alternden Bevölkerung zu einem steigenden Bedarf an präventiven und nachsorgenden Untersuchungen der pAVK führt. Zur Diagnose wird Ultraschallbildgebung am häufigsten eingesetzt, da diese eine schnelle, nichtinvasive, strahlungs- und schmerzfreie Untersuchung der Gefäße ermöglicht. Diese Ultraschalluntersuchungen sind jedoch komplex und zeitaufwendig, weshalb sie spezialisierte Fachkräfte erfordern. Der fortschreitende Personalmangel im klinischen Bereich lässt erwarten, dass zukünftig ein Versorgungsdefizit bei der Durchführung dieser Untersuchungen entsteht. Daher wurde im Rahmen dieser Arbeit ein kraftsensitives robotisches Ultraschallsystem entwickelt, das automatisierte vaskuläre Untersuchungen ermöglicht und somit zu einer zuverlässigen Patientenversorgung in der Zukunft beitragen kann. Untersucht wurden dabei sowohl vorbereitende Maßnahmen der Untersuchung, wie die optimale Roboter-Patienten-Positionierung, als auch die sichere Bewegungsführung der Sonde während des robotischen Scanvorgangs.

Zunächst wurde analysiert, wie die Geometrie der Schallkopfhalterung am Endeffektor die optimale Positionierung der Roboterbasis beeinflusst, sodass eine möglichst gute Erreichbarkeit des Zielbereichs vorliegt. Durch die Berechnung anwendungsspezifisch angepasster Schallkopfhaltergeometrien konnte die Anzahl optimal geeigneter Basisplatzierungen deutlich erhöht werden. Dieser Vorteil war besonders stark in Szenarien ausgeprägt, in denen ein Teil des verfügbaren Untersuchungsraums durch Hindernisse eingeschränkt war.

Anschließend wurde die automatisierte Durchführung robotischer Ultraschallscans der Femoralarterie im Rahmen einer Probandenstudie validiert. Eine angepasste Interaktionsregelung mit definierter Sondenkontaktkraft gewährleistete eine hohe Bildqualität und die Sicherheit des Patienten. Während des Scans entlang des Beins wurde die Arterie kontinuierlich zentriert im Ultraschallbild gehalten. Doppler Ultraschall erwies sich hierbei als effektive Methode zur Arterienverfolgung, da die Visualisierung des Blutflusses eine zuverlässige Unterscheidung zwischen Arterien und Venen ermöglichte. Nachfolgend wurden zur Steigerung der Funktionalität des robotischen Ultraschallsystems mehrere Zusatzfunktionen entwickelt. Diese umfassten einen Ansatz zur automatischen Anpassung der Orientierung der Sonde, um das automatische Scannen stark gekrümmter Oberflächen zu ermöglichen. Darüber hinaus wurde das Auftragen von Ultraschallgel, das für US-Untersuchungen zwingend notwendig ist, automatisiert.

Abschließend wurde die Genauigkeit des am Endeffektor des Roboters erfassten Wrenches, also der wirkenden Kräfte und Momente, untersucht. Eine möglichst präzise Schätzung des Wrenches stellt die Grundlage für eine sichere Interaktion zwischen Roboter und Patient dar. Daher wurde eine Methode präsentiert, bei der ein neuronales Netz auf die Abhängigkeiten zwischen den gemessenen Gelenkmomenten in den Roboterachsen und den auf den Endeffektor wirkenden Kräften und Momenten trainiert wurde. Die Genauigkeit und Robustheit der Schätzung des Wrenches konnten somit stark verbessert werden, insbesondere durch die Verringerung extremer Ausreißer, die im Standartmodell des Herstellers auftraten, wenn sich der Roboter in der Nähe von Singularitäten bewegte.

Zusammengefasst werden in dieser Arbeit neuartige Methoden für die Entwicklung eines robotischen Ultraschallsystems vorgestellt. Die gewonnenen Erkenntnisse stellen einen Schritt in Richtung zukünftiger vollautomatischer Ultraschalluntersuchungen dar. Besonders im Kontext der Diagnostik und Überwachung der pAVK bietet das System Potenzial, durch standardisierte, automatisierte Bildgebung die Patientenversorgung erheblich zu verbessern.

ABSTRACT

Peripheral arterial disease (PAD) is one of the most common cardiovascular diseases, affecting more than 230 million people worldwide. It is a form of peripheral atherosclerosis involving the narrowing or blockage of arteries, most commonly in the legs, due to plaque buildup. This reduces blood flow and can lead to tissue damage. The early diagnosis of PAD is crucial to prevent the progression of the disease, maintain the quality of life of patients, and avoid serious complications. The prevalence of PAD increases sharply with age, resulting in an increasing demand for pre- and post-examination of PAD, particularly in industrialized countries with an aging population. Ultrasound imaging (US) is most commonly used as a diagnostic tool, as it enables a fast, non-invasive, radiation-free, and painless examination of vessels. However, the time-consuming and complex nature of US, combined with the growing shortage of clinical staff, is expected to create a gap in its availability in the future. Thus, a force sensitive robotic US system was developed in this thesis, which will enable automatic vascular US examinations for diagnostic purposes, ensuring reliable patient care in the future. Several challenges in the development of such a system have been addressed. This included the investigation of preparatory aspects prior to the examination, such as optimal robot-patient positioning, as well as the safe guidance of the probe during the robotic scanning process.

Firstly, the relationship between the geometry of the probe holder and the positioning of the robot's base in relation to the patient was investigated. By determining adapted use-case specific probe holder geometries, optimal reachability of the anatomical region to be examined (e.g. the femoral artery) was ensured. The use of an appropriate probe holder geometry strongly increased the number of potential base placements with high reachability, especially in scenarios where obstacles restricted a part of the available space.

Subsequently, a volunteer study was conducted to validate the feasibility of robotic US scans of leg arteries. An adapted interaction control scheme that also accounts for probe contact force was implemented to ensure patient safety. During the scan along the leg, the artery was automatically kept in the center of the US image for optimized image quality. Doppler ultrasound proved to be an effective solution for arterial tracking in this context, allowing for reliable differentiation between arteries and veins based on blood flow visualization. Moreover, additional specific features have been developed to further enhance the system. An approach to automatically adjust the orientation of the probe has been developed to enable automatic scanning of highly curved surfaces. Furthermore, the US gel application, which is essential for US examinations, was automated.

Finally, the accuracy of the robot's wrench estimation was investigated. Accurate wrench estimation of the robot is essential to ensure the safety of the system, especially in contact with the patient. Thus, a learning approach was proposed in which a neural network was trained on the dependencies between the joint torques in the robot's axes and the forces and moments acting on the end effector. This strongly increased the accuracy and robustness of the wrench estimation model of the robot, in particular by reducing extreme outliers that occurred in the manufacturer's model when the robot moved close to singularities.

In summary, this thesis presents novel methods for the development of a robotic US system. The findings of this work represent a step towards future fully automated US examinations. Especially in the context of PAD diagnosis and monitoring, the system has the potential to considerably improve patient care through standardized and automated imaging.

ACKNOWLEDGEMENTS

Firstly, I would like to thank my supervisor, Prof. Dr. Floris Ernst, for his guidance, encouragement, and support throughout my doctoral studies. He gave me the opportunity to work on this fascinating subject and to realize my ideas freely. I could always rely on his full support whenever I needed it - both academically and personally, which I greatly appreciate.

Furthermore, I would also like to say a big thank you to all my colleagues from the Institute of Robotics and Cognitive Systems - it was a pleasure to work with you! In particular, I would like to thank Cornelia Rieckhoff, who was always available for any kind of organizational support during my time at the institute.

I also want to thank Marco Horn and Alexandra Scheibert, involved in the RoGUS-PAD project from the Division for Vascular and Endovascular Surgery of the UKSH Lübeck for their clinical expertise as well as their professional support in the realization of our studies. Moreover, I would also like to thank Christian Damiani from the TH Lübeck for preparing our phantoms, which were essential for the experimental work and the system's development.

And last but not least, another huge thank you to my friends, my family, and particularly my wife Magda for their support and encouragement throughout my studies. Having such a supportive social circle is anything but self-evident, and I am truly grateful for it.

CONTENTS

MATHEMATICAL NOTATION

The following mathematical notation conventions apply in this work. Scalars are represented by lowercase italic letters, i.e. $a \in \mathbb{R}^1$, while vectors are denoted by bold lowercase letters (e.g. $\mathbf{g} \in \mathbb{R}^3$). Matrices are represented by bold capital letters, i.e. $\mathbf{M} \in \mathbb{R}^{7x7}$. A homogenous transformation matrix from coordinate frame j to i is denoted by ${}^{\mathrm{j}}\mathbf{T}_{\mathrm{i}} \in \mathbb{R}^{4\times4}$. It represents the transformation that expresses the positions and orientations of frame i relative to frame j.

1

INTRODUCTION

Peripheral arterial disease (PAD) is one of the most common cardiovascular diseases, affecting more than 230 million people worldwide [1]. It is characterized by partial or complete obstruction of one or more peripheral arteries due to atherosclerosis. This results in a restriction of blood flow in the arteries that supply the extremities and the abdominal aorta. In most cases, PAD affects the lower extremities and typically develops gradually. Initially, most people are asymptomatic. However, over time, the legs' arteries narrow progressively, leading to ischemia, leg pain, and an increased risk of heart attack and stroke. Early diagnosis of PAD is therefore crucial in order to prevent the progression of the disease, maintain the quality of life of patients and avoid serious complications. For diagnosis, ultrasound (US) imaging is most commonly used, as it enables fast, noninvasive, radiation-free and painless examination of the vessels [2]. Another advantage is the possibility of using Doppler ultrasound to assess not only the anatomy of the vessels but also the hemodynamics, as the flow velocity of the blood cells changes with a reduced diameter based on Bernoulli's principle. This means that even minor vessel narrowing and resulting changes in blood flow in the arteries can be visualized before clinical symptoms occur. The prevalence of PAD increases sharply with age, as can be seen in Figure 1.1.

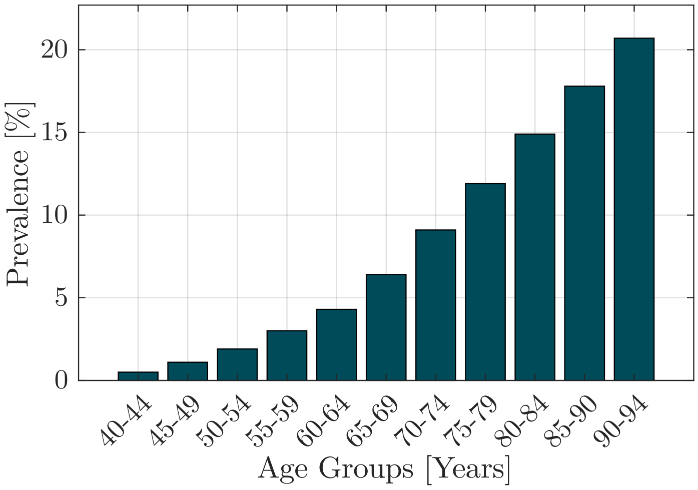

Figure 1.1: Global prevalence of peripheral arterial disease depending on age. The data are based on [3].

Consequently, the number of patients requiring pre- and post-examination for PAD continues to grow, particularly in industrialized countries with an aging population. However, extensive US examinations require a lot of time (up to 45 minutes per patient [4]) and highly qualified specialists to carry them out. As the general shortage of staff in clinics is increasing at the same time, this will lead to a gap in the availability of these examinations in the future [5]. Robotic US systems could provide a potential solution for the automation of vascular scans and thus reliably support future patient care. By combining US imaging and a robot through the attachment of an US probe to the end effector, precise and repeatable US images can be acquired in an automated manner, while ergonomically relieving sonographers and counteracting staff shortages.

1.1 Goal of this Thesis

The aim of this thesis is the development of a force sensitive robotic system that enables automatic vascular US examinations for diagnostic procedures. There are several challenges in the realization of such a system that will be addressed in this work. This includes the investigation of preparatory aspects prior to the examination, such as optimal robot-to-patient positioning, as well as the safe guidance of the probe during the robotic scanning process.

Firstly, to ensure a successful examination, accurate positioning of the robot relative to the patient is essential, as improper placement can lead to incomplete scans or difficulties in moving the probe in the target area, as the robot's working range is limited. Thus, an appropriate robot-patient positioning must be ensured in the pre-scanning phase of the examination, i.e. before the robot starts scanning the vessel (Figure 1.2). This ensures that all target poses on the patient that are to be scanned by the US probe attached to the robot can be reached with maximum freedom of movement, also referred to as reachability. The reachability of the target

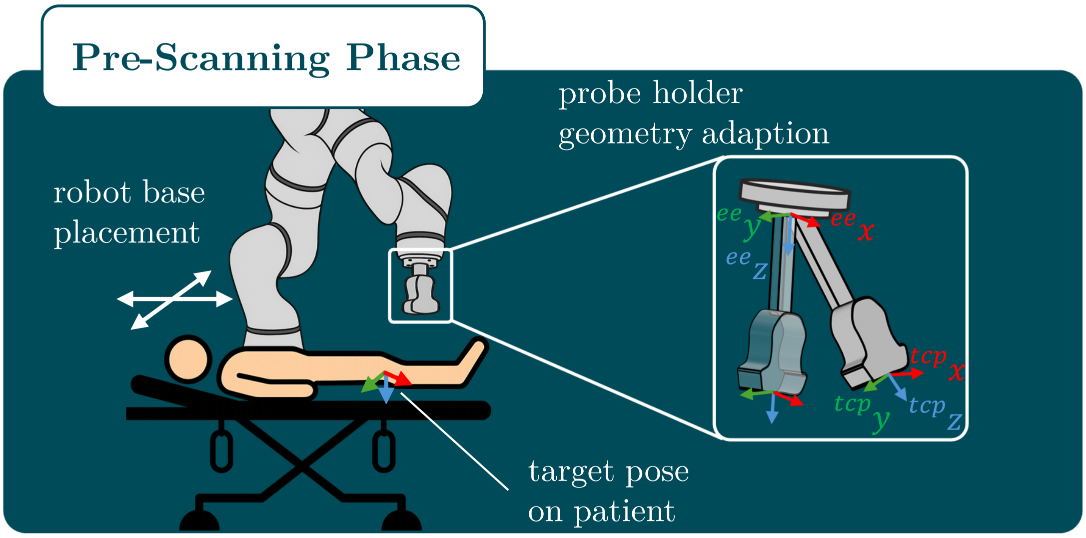

Figure 1.2: Optimized robot-patient positioning in the pre-scanning phase depends on the robot's base placement, its working range, and the geometry of the probe holder, which defines the transformation from the end effector to the probe's tool center point. The images of the robot and patient were generated by ChatGPT [6].

poses for a specific robot depends on two factors, the actual placement of the robot's base and the geometry of the probe holder used to attach the US probe to the robot's end effector (Figure 1.2). This relationship is studied with the aim of determining an optimal probe holder geometry and base placement by addressing the following research question:

> **Research Question 1**
> How can a probe holder be designed to maximize the reachability of target poses?

Once the robot has been placed appropriately, the scanning phase of the procedure (Figure 1.3) can follow. As part of this work, an automatic femoral artery scan for medical screening and follow-up examinations for the diagnosis and therapy of PAD is presented. The robot must therefore guide the US probe along the patient's leg vessel. For high quality US imaging, essential for reliable diagnostics, the robotic system must fulfill the following requirements:

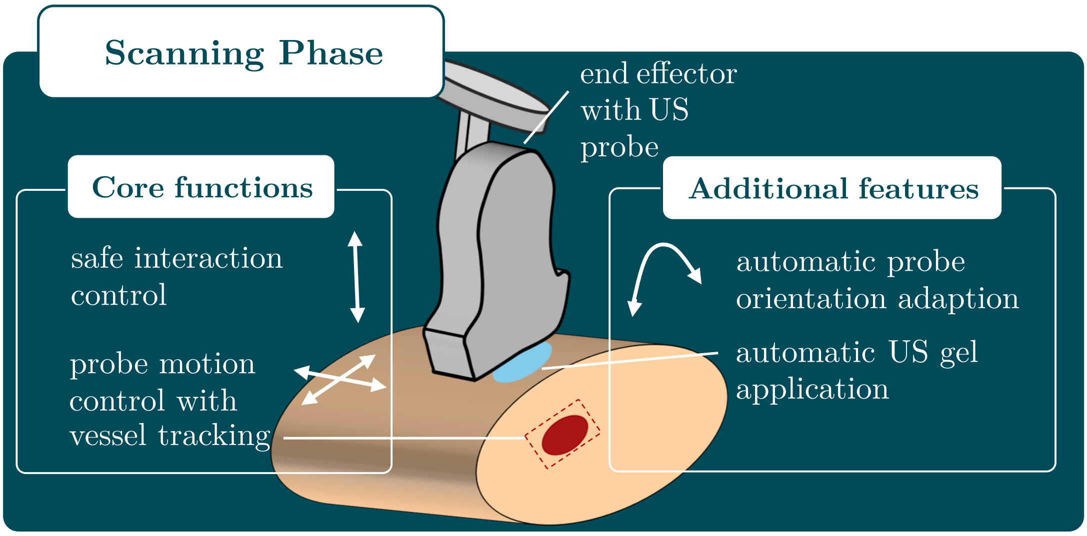

Figure 1.3: Challenges for an automatic robotic US examination of vessels during the scanning phase. The US probe must be applied with a defined contact force, while it's position and orientation can be adapted, e.g. according to the vessel being tracked. Furthermore, acoustic coupling must be achieved through the application of US gel.

1. **Compliance:** The robot must behave compliantly, ensuring patient safety.

2. **Consistent Contact Force:** The probe must be applied with a defined contact force.

3. **Probe Orientation Adaption:** While moving the probe, full contact with the surface must be maintained.

4. **Probe Position Adaption:** The vessel must be tracked in the US image and the position of the probe must be corrected accordingly.

5. **Acoustic Coupling:** US gel must be supplied to enable acoustic coupling. This can be done either manually, e.g. prior to examination, or automatically while scanning.

The corresponding requirements are met by the solutions proposed in this work. The requirements are classified into two categories, namely *core functions* and *additional features*. The core functions represent the essential functions of the robotic US system to perform an automatic examination of the leg artery. These include a safe interaction control of the robot, which combines robot compliance with the application of a defined probe contact force. In addition, motion control is essential to move the probe to a defined position and orientation. In particular, to ensure that the entire leg artery can be scanned, it is necessary to automatically adjust the position of the probe according to the detected vessel position. Thus, to enable a basic system for performing robotic US scans, the following research question will be answered:

> **Research Question 2**
> How can the essential core functions of the robotic system be realized to enable a straightforward automatic US examination of the femoral artery?

To this end, a feasibility study is presented to validate the core functions of the robotic system to automatically scan the leg arteries of volunteers.

The additional features of the robotic US system include the automatic adjustment of the probe's orientation according to the surface and the automatic supply of US gel. Although these features are not absolutely necessary to perform a robotic US scan, they do extend the range of applications and increase the degree of automation. This leads to the following research question:

> **Research Question 3**
> How can additional features of automatic probe orientation adaption and US gel supply be integrated into the robotic US system?

For this purpose, methods are presented for the respective fulfillment of these additional features. An approach for determining a probe orientation correction based on 3D US volumes is introduced. This allows the probe orientation to be adjusted during the scan, thus always ensuring full probe contact, even on highly curved surfaces. In addition, a control strategy is proposed incorporating the robot's nullspace to automatically supply US gel via a passive mechanism.

Finally, an approach to improve the accuracy and robustness of the robot's contact wrench estimation model using its internal torque sensors is presented. Although the proposed method can be applied to automatic vessel scans, it has generic relevance in robotic tasks that require precise wrench estimation. A separate chapter therefore discusses the fourth research question of this work:

> **Research Question 4**
> How can the accuracy of the robot's wrench estimation as well as the robustness be increased in quasi-static scenarios?

The proposed method allows forces and moments acting on the end effector during quasi-static movements to be captured more reliably, especially in poorly configured positions of the robot, thereby increasing system safety.

1.2 Structure of this Thesis

This thesis is structured as follows. To provide a better understanding for the reader, the medical and technical background is first explained in Chapter 2. Subsequently, the previously outlined research questions are investigated in self-contained chapters, each contributing to the development of an automatic robotic US examination of the leg vessels, as visualized in Figure 1.4. Chapter 3 addresses **RQ1**, the optimization of robot base placement and probe holder design, which belong to the pre-scanning phase of the automatic robotic US vessel examination. The development and validation of the core functions of the robotic US system in the scanning phase to enable automatic leg artery examinations, as considered in **RQ2**, are presented in Chapter 4. Potential methods for implementing additional features mentioned in **RQ3**, i.e. automatic probe alignment and automation of US gel supply, are presented in Chapter 5. This is followed by Chapter 6, which provides a learning approach to improve the wrench estimation accuracy and robustness of the robot, addressing **RQ4**. Finally, Chapter 7 contains a summarizing discussion and outlook.

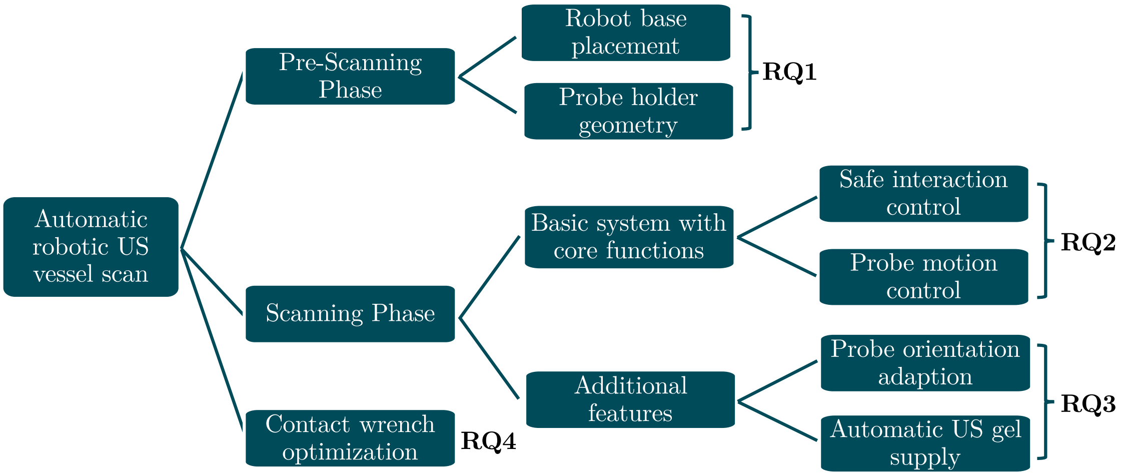

Figure 1.4: Structure of the thesis. The essential topics required for automatic robotic US examination are addressed in individual chapters.

2 MEDICAL AND TECHNICAL BACKGROUND

This chapter provides an overview of the fundamental knowledge required for the topics covered in this thesis. It begins with a medical introduction to the pathology of PAD, which represents an exemplary application for the usage of the robotic US system. Then, the technical background of the components used for the robotic system is described, including an US station and a collaborative robot. The chapter concludes with a theoretical introduction to robot dynamics, workspace and reachability.

2.1 Peripheral Arterial Disease

PAD is a common disorder of the circulatory system that affects more than 230 million people worldwide [1]. PAD is caused by atherosclerosis. Atherosclerosis is a disease that leads to hardening and narrowing of the arteries as plaque builds up in their walls, as shown in Figure 2.1, resulting in reduced blood flow to the extremities. This ischaemia usually manifests as pain in the thigh or calf, affecting mainly the lower extremities. PAD usually affects the large arteries of the lower limbs, including the abdominal aorta, iliac and femoral arteries. It's particularly noticeable during physical activity when the demand for oxygen and nutrients in the muscles is high, causing ischemic symptoms that improve at rest. PAD is a progressive disease with a high risk of complications in advanced stages, including critical limb ischaemia, gangrene and amputation. Cardiovascular morbidity and mortality is considerably increased in patients with PAD as they have a similar risk profile to patients with coronary artery disease. Prognosis of PAD depends on early diagnosis, effective risk management and adherence to treatment [7].

PAD is diagnosed through a combination of patient history, physical exam and objective tests like the ankle brachial index (ABI). The ABI is a simple, commonly used non-invasive test to evaluate the flow of blood into the lower limbs using differences in blood pressure between arms and ankles. Normal values for the ABI are between 0.9 and 1.3. An ABI <0.9 indicates PAD and very low values (i.e., <0.5) indicate severe disease, often with ischemic rest pain or tissue loss [7]. Additional imaging such as Doppler US, computed tomography angiography (CTA) or magnetic resonance imaging (MRI) can be used to assess the vessels more accurately [8], though Doppler US has become the prioritized tool [2]. However, the rate of false negative PAD diagnoses is high because patients either show no symptoms or have atypical ones, thus preventing timely intervention.

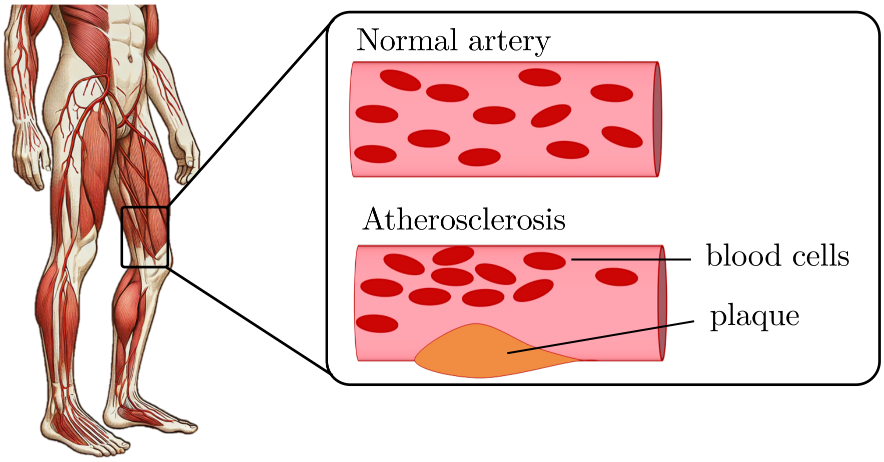

Figure 2.1: Comparison of a healthy femoral artery and an artery with atherosclerosis, as occurs in PAD. The decreased cross-section of the vessel results in reduced blood flow to the extremities. The image of the body model was generated by ChatGPT [6].

In addition to the usual risk factors for atherosclerotic diseases such as smoking, diabetes, obesity and high blood pressure, age is an important factor, as the prevalence of PAD strongly increases with age [3]. The industrialized countries are confronted with an increasingly aging society and therefore a corresponding increase in prevalence values. For example, in Germany, the average prevalence of patients over 40 years of age increased from 1.85 % in 2009 to 3.14 % in 2018, demonstrating the growing extent of the disease [9]. More efficient, automated diagnostic processes could increase early detection and thus improve the treatment and prognosis of affected patients.

2.2 Ultrasound Imaging

US imaging or sonography is a non-invasive diagnostic technique in which high-frequency sound waves are used to visualize internal structures of the body. It is the most frequently used diagnostic imaging procedure in clinics worldwide and offers several advantages for diagnostic and interventional procedures [10]. These include freedom from ionizing radiation, good soft tissue contrast, low cost, high flexibility and real-time image acquisition [11].

2.2.1 Physical Principle

The basic principle of this technique is the interaction of sound waves with various tissues and their subsequent reflection. US waves are generated with the use of piezoelectric crystals. These crystals are electrically energized, which causes them to deform mechanically and generate longitudinal sound waves. When an US wave is transmitted into the body, it hits different types of tissue, each with unique acoustic properties. As a result, the US wave is attenuated to varying extents depending on the tissue. The main mechanisms involved are absorption, reflection, and refraction, scattering and divergence, with reflection being the most important for image generation in order to obtain anatomical-morphological information of tissues and organs. An important parameter that influences the propagation of sound waves is the acoustic impedance z, which is determined by the product of tissue density ρ and sound velocity c:

$$z = \rho \cdot c. \tag{2.1}$$

At the boundaries between tissues (e.g. fat, muscle, organ boundary) with different acoustic impedance, part of the sound wave is reflected. The reflectivity is characterized by the reflection coefficient r

$$r = \frac{(z_1 - z_2)^2}{(z_1 + z_2)^2}. \tag{2.2}$$

The greater the difference between the impedance of two tissues or structures, the stronger the reflection. This leads to almost complete reflection when the sound waves enter bone or air due to their high or low acoustic impedance, respectively, compared to the tissue. Consequently, the structures behind them cannot be imaged. This effect also occurs when the probe is placed on the body surface. For this reason, US gel is required to ensure coupling of the waves into the body. The gel has nearly the same acoustic impedance as the human skin. Therefore, sound reflections are avoided and the US waves can enter the tissue, ensuring high-quality US images [12].

The reflected sound waves are picked up by the transducer elements, and the distance to the reflecting surface is calculated from the time that elapses between the emission and reception of the impulse. Assuming a constant sound velocity $c = 1540 \ \frac{m}{s}$ in human tissue [13], the depth of the reflecting structure can be determined. The intensity of the reflected echoes is coded as grayscale values to generate an image, which is why it is also referred to as B-mode (B for brightness modulation) US [11]. Areas with high acoustic impedance, such as bone, reflect a large portion of the sound wave, resulting in strong echoes and bright areas in the image. Tissues with low acoustic impedance, such as soft tissue, on the other hand, transmit most of the sound wave, resulting in weaker echoes and darker areas.

2.2.2 2D, 3D and 4D Ultrasound

US imaging capabilities have advanced substantially over the years, evolving from 2D to 3D and 4D modalities. In conventional 2D US imaging, a single linear array of piezoelectric elements in the transducer probe is used to generate and receive sound waves (Figure 2.2A). As a result, a cross-sectional image of the tissue is created. While 2D US is inexpensive and widely used, it has limitations in terms of the ability to visualize complex 3D structures. In order to generate 3D US volumes, there are various options. Conventional 2D US images from different angles can be stuck together, and thus a volume of the tissue can be reconstructed. However, applying 3D reconstruction methods can be time-consuming and computationally intensive [14]. In addition, the relative geometry of the imaging plane and the axis of rotation must be accurately known to avoid artifacts [15]. These drawbacks can be overcome by using 2D matrix phased array transducers. Examples for these probes

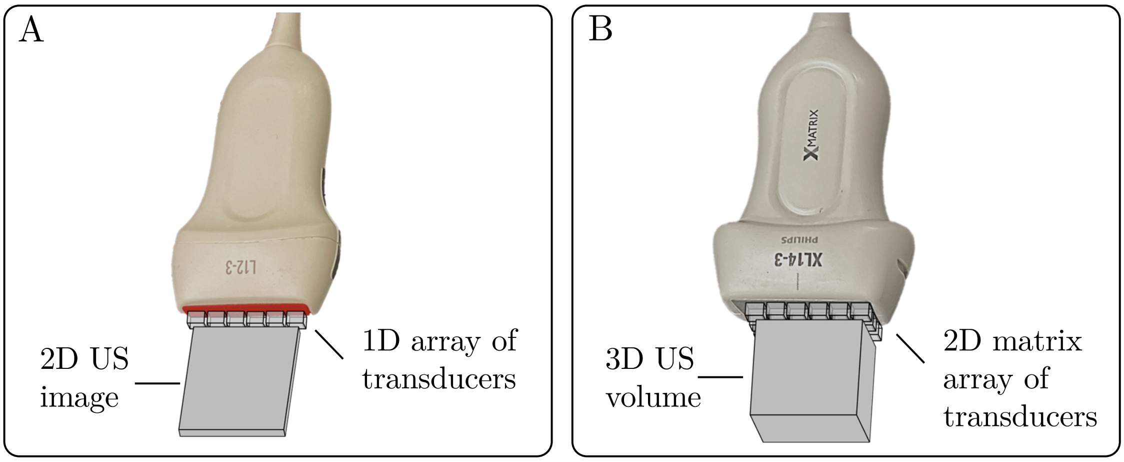

Figure 2.2: Example of two US probes for vascular applications. The *Philips L12-3* probe, which provides 2D US images, is shown on the left (A). In contrast, 3D US volumes can be recorded directly with the *Philips XL14-3* probe (B).

are shown in Figure 2.2B. With this transducer type, 3D US volumes can directly be generated, allowing for real-time visualization of three-dimensional structures, also referred to as 4D US, incorporating the dimension of time [11]. By using 4D US, an improved dynamical assessment can be enabled, which can be useful for a variety of medical applications, e.g. in the field of cardiac and vascular diagnostics.

2.2.3 Doppler Ultrasound

In addition to the anatomical-morphological information about tissues and organs in the body, US can also be used to provide the examiner with additional information about the kinetics of blood flow. This is known as Doppler US, as it is based on the physical principle of the Doppler effect.

Physical Principle

The Doppler effect is a physical principle where the frequency of sound waves changes when they reflect off moving objects. The sound frequency shifts depending on the motion of an object relative to the observer. In the medical application of US, this refers to sound waves reflecting off moving red blood cells within vessels. Stationary objects like tissue do not cause any frequency change when sound waves get reflected. Contrary, moving objects like blood cells cause a frequency shift. If blood cells are moving toward the transducer, the reflected sound has a higher frequency than the transmitted one, as shown in Figure 2.3. If they are moving away from the transducer, the frequency is lower. This frequency shift f_D is directly proportional to the velocity of blood flow and be calculated by

$$\begin{aligned} f_D &= f_r - f_t \\ &= \frac{2 v_b f_t}{c} \end{aligned} \tag{2.3}$$

where f_t is the transmitted frequency of the US waves. The frequency of the reflected sound waves is given by f_r. The velocity of the blood is denoted as v_b, and the Speed

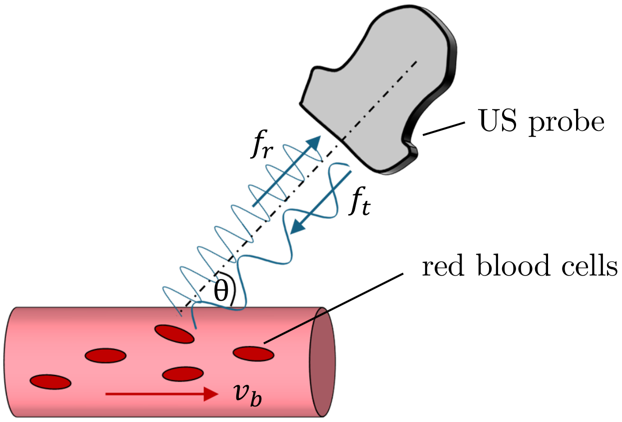

Figure 2.3: Schematic representation of the physical principle of Doppler US. The blood cells reflect the US waves that are emitted from the US probe with frequency f_t. As the blood cells move towards the probe with a certain velocity v_b, the frequency f_r of the reflected sound waves increases. The angle between the US beam and the blood flow is denoted as Doppler angle θ [11].

of Sound in the tissue is c [16], [17].

Typically, the Doppler beam is applied non-invasively and therefore not directed straight into the oncoming blood flow. Instead, it is angled externally to the blood vessel at an angle θ relative to the vessel's longitudinal axis. In this case, the expression for the frequency shift becomes:

$$f_D = \frac{2 f_t v \cos(\theta)}{c}. \tag{2.4}$$

By measuring the frequency shift, the flow velocity of the blood can be determined. As Eq. (2.4) indicates, perpendicular probe positioning to the vessel results in diminishing frequency shift and should therefore be avoided. Finally, the blood flow can be visualized in different ways with respect to the chosen mode. The different Doppler modalities are briefly explained in the following.

Doppler Modalities

The different Doppler modalities include continuous wave (CW) Doppler, pulsed wave (PW) Doppler, color Doppler as well as power Doppler. CW Doppler (Figure 2.4A) determines frequency shifts along a path using separate transmit and receive transducers. It continuously transmits and receives sound, filtering for shifted frequencies. These shifts are plotted as velocity over time. CW Doppler measures high velocities but lacks depth information, making it unable to localize the origin of these velocities [18].

In contrast to this, with PW Doppler (Figure 2.4B), the transmission and reception mode is analogous to the pulse-echo principle, which enables depth assignment of the flow information. However, PW Doppler cannot achieve a sufficient sampling rate to avoid aliasing. Aliasing occurs when the speed of movement, measured in pulses per second (e.g., blood flow), exceeds half the sampling rate of the pulsed Doppler waves, potentially causing misinterpretation of the flow direction [19].

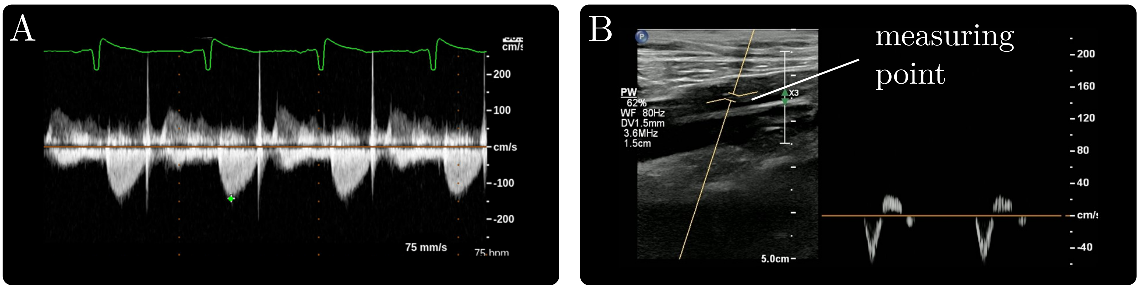

Figure 2.4: Doppler Modalities. **A:** Exemplary CW Doppler spectrum, where blood flow velocities of up to 1 $\frac{m}{s}$ were recognized while examining the heart (Figure adapted from [20]). **B:** PW Doppler examination of the femoral artery. The blood flow velocity is measured at a defined point and visualized over time.

PW Doppler can be combined with conventional US imaging, which is referred to as color Doppler or Duplex Sonography (Figure 2.5A) [21]. This enables the simultaneous visualization of anatomical structures and the blood flow within these structures. Duplex sonography allows physicians not only to assess blood flow dynamics but to simultaneously perceive the morphologic context of the organ (e.g. heart or vessels), providing a more comprehensive insight into the areas being examined. This is crucial, for example, in the assessment of hemodynamically relevant vascular constrictions, which is why duplex sonography has become the preferred diagnostic tool in the diagnosis and aftercare of vascular pathologies [2], [21]. Typically, flows towards the transducer are shown in red and flows away from the transducer in blue in the US image. The magnitude of the relative average velocities is coded according to the color tone: the lighter the color tone, the greater the speed of the corresponding blood cells. Color Doppler is useful for qualitative information about the blood flow, as there is no precise absolute measurement [22].

Power Doppler (Figure 2.5B) is a Doppler imaging technique that overlays information about the amplitude (or power) of returning Doppler signals onto an US image. This differs from color and spectral Doppler, which focuses on frequency information. In power Doppler, a pulsed interrogation is performed over a sample volume, and echoes with shifted frequencies due to blood flow are identified. However, instead of analyzing the frequency information, power Doppler only considers the amplitude of these echoes. The amplitudes are then mapped to a color scale, typically shades of orange, with higher amplitude signals appearing as lighter shades. These shades represent the strength or power of the returning signals and do not provide information about flow direction or velocity. An increase in signal strength is generally attributed to a larger volume of moving blood, but other factors like shear rates and the number of scatterers within the sample volume can also contribute. One major advantage of power Doppler is its reduced sensitivity to Doppler angle θ. This means it can detect a flow that is closer to perpendicular to the US beam, which can be challenging for traditional color and spectral Doppler. Additionally, Power Doppler is less susceptible to noise from surrounding tissues, making it more sensitive to low-flow states [22].

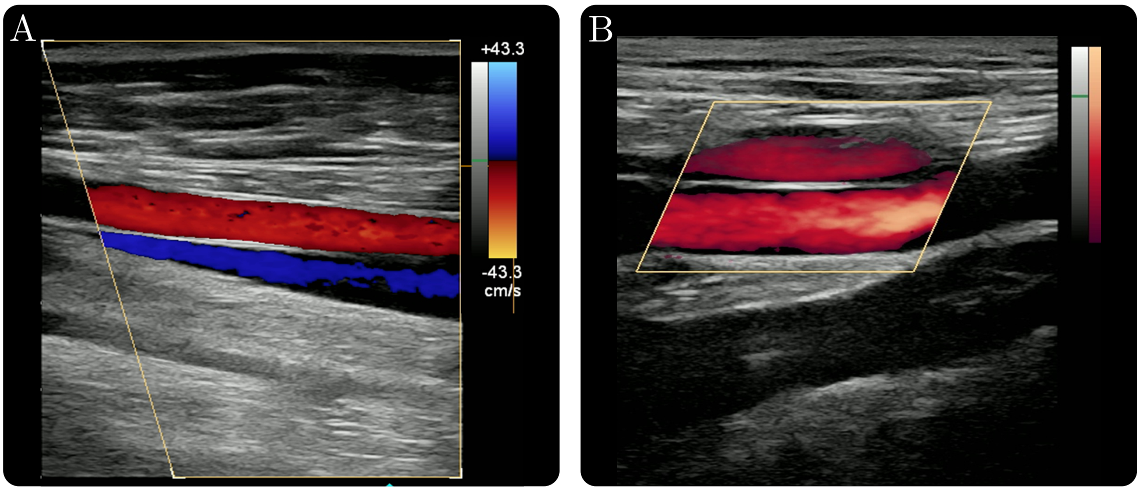

Figure 2.5: Doppler modalities. **A:** Colored representation of the blood flow in the femoral artery (red) and vein (blue), which is also referred to as color Doppler or Duplex Sonography. Blood flowing in the direction of the transducer is displayed in red, and blood flowing in the opposite direction of the transducer is shown in blue. **B:** Example of an examination of a vessel with power Doppler. The faster the blood flows, the brighter the color shown, whereby no conclusion can be given about the flow direction.

2.3 Collaborative Robots

Collaborative robots are a specialized type of robotic system designed to work safely and efficiently alongside human operators in shared workspaces. Unlike traditional industrial robots that are confined to safety cages, collaborative robots are equipped with safety features that allow for direct interaction with humans, making them well suited for medical applications such as robotic US [23].

2.3.1 Robot Design

The possibility of using collaborative robots in direct contact with humans requires a specific mechatronic design. The movement of the robot's joints is generated by specially developed direct current (DC) motors with low speed and high torque. The torque of the motor is then transmitted to the following link via a strain wave gear, which is also referred to as *Harmonic Drive*, with a large reduction ratio of between 100:1 and 160:1. A joint position sensor and a torque sensor are located on the gear output. With the help of these torque sensors installed in the robot's joints, safety functions such as the detection of external forces and collisions can be realized [24]. The robots used in this work are the LBR iiwa 7 R800 and LBR iiwa 14 R820 (KUKA, Augsburg, Germany). These are two versions of the same robot model, which differ only in their maximum working range (800 vs. 820 mm) and payload capability (7 kg vs. 14 kg). While detailed specifications of the LBR iiwa are not publicly available, the robot's design is based on the predecessor model LWR III, which was developed by the German Aerospace Center (DLR). The respective electronics and mechanics are well documented in literature, for more detailed information please refer to [25], [26].

A design feature of this robot type is its kinematic redundancy. The robot

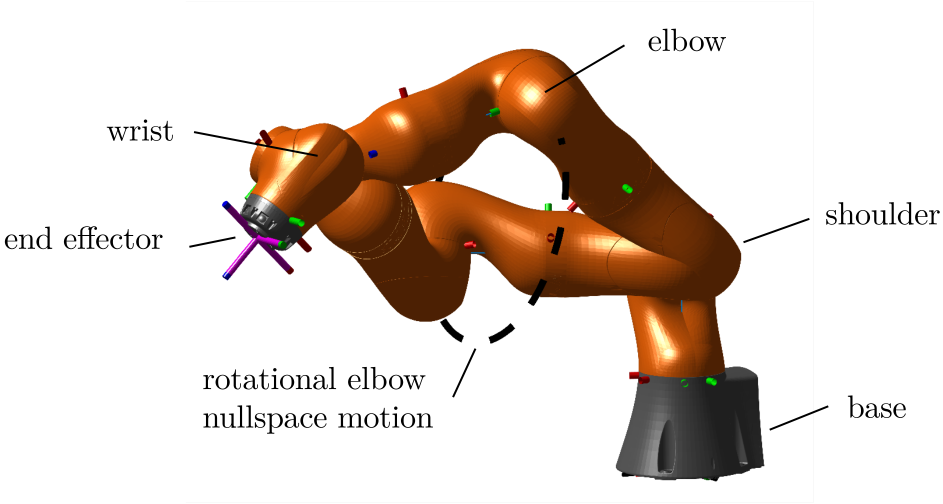

Figure 2.6: The LBR iiwa 7 has been designed with a spherical-revolute-spherical configuration. Due to the seventh Dof, the robot's elbow can be rotated without changing the end effector position. The figure was created using the Robotics System Toolbox for Matlab Simulink [27].

consists of seven motorized joints, resulting in seven degree of freedoms (DoF) in total. Accordingly, the robot is kinematically redundant, as it possesses more than six degrees of freedom, which are sufficient to define a pose in the task space of the robot, represented by the Special Euclidean group $SE(3)$. This group describes all rigid body transformations in three-dimensional space, i.e., the combination of translation and rotation. The additional seventh DoF of the redundant robot can be used to reconfigure the robot without changing the end effector pose, which is also referred to as a nullspace motion. This represents a rotation of the robot's elbow, as visualized in Figure 2.6, that can be used to avoid obstacles, singularities, or joint limits. The structure of most collaborative redundant robots is modelled on the human arm as a kinematic chain consisting of seven revolute joints. Adjacent axes are usually arranged orthogonally to each other, also known as a spherical-revolute-spherical configuration. Due to the anthropomorphic joint structure of the robot, parts of the robot are also referred to as the shoulder, elbow, and wrist. The shoulder represents the intersection of the first three axes (see Figure 2.6) and the wrist the intersection of axes five, six, and seven. The elbow is typically defined as the joint that provides the primary bending motion in the middle of the serial manipulator, thus in most cases it is the fourth joint.

2.3.2 Dynamics and Wrench Estimation

The integrated torque sensors in the joints allow an estimation of the external forces and moments acting on the end effector. This is particularly useful for medical applications such as robotic US, where contact occurs between the robot and its environment, e.g. the patient's skin. The theoretical foundations for estimating the external forces and moments are briefly explained below. For a more detailed description of the proprietary robot control architecture of flexible joint robots, please refer to [24], [26], [28].

A collaborative robot with a serial open-loop kinematic chain consists of n rotary joints connecting adjacent links. Its dynamic model maps the joint actuator torques $\boldsymbol{\tau} \in \mathbb{R}^n$ to the motion of the manipulator, represented by the joint positions and their respective time derivatives $\mathbf{q}, \dot{\mathbf{q}}, \ddot{\mathbf{q}} \in \mathbb{R}^n$. The joint space dynamics model is given by

$$\mathbf{M}(\mathbf{q})\ddot{\mathbf{q}} + \mathbf{C}(\mathbf{q}, \dot{\mathbf{q}})\dot{\mathbf{q}} + \mathbf{g}(\mathbf{q}) + \boldsymbol{\epsilon}(\mathbf{q}, \dot{\mathbf{q}}, \ddot{\mathbf{q}}) = \boldsymbol{\tau} - \boldsymbol{\tau}_{\mathrm{ext}}. \tag{2.5}$$

$\mathbf{M}(\mathbf{q}) \in \mathbb{R}^{n \times n}$ represents the symmetric and positive-definite inertia matrix in joint space, which describes the robot's inertia for a specific joint-space configuration q. The matrix $\mathbf{C}(\mathbf{q}, \dot{\mathbf{q}}) \in \mathbb{R}^{n \times n}$ captures the Coriolis and centripetal forces, which are functions of the joint positions $\mathbf{q}$ and velocities $\dot{\mathbf{q}}$. The term $\mathbf{g}(\mathbf{q})$ accounts for the torques generated by gravitational effects at any given configuration $\mathbf{q}$. Nonlinear backlash and friction effects can be represented by $\boldsymbol{\epsilon}(\mathbf{q}, \dot{\mathbf{q}}, \ddot{\mathbf{q}})$ [29]. External forces and moments acting on the end effector, which are induced from payloads or environmental influence, are included with the term $\boldsymbol{\tau}_{\mathrm{ext}}$. These external forces and moments are also referred to as wrench $\mathbf{w}_{\mathrm{ext}} \in \mathbb{R}^6$, which is defined as

$$\mathbf{w}_{\mathrm{ext}} = \begin{pmatrix} \mathbf{f}_{\mathrm{ext}} \\ \mathbf{m}_{\mathrm{ext}} \end{pmatrix}, \tag{2.6}$$

consisting of contact forces $\mathbf{f}_{\mathrm{ext}} \in \mathbb{R}^3$ and moments $\mathbf{m}_{\mathrm{ext}} \in \mathbb{R}^3$. By using the transposed geometric Jacobian $\mathbf{J}(\mathbf{q})$ of the end effector, the external joint torques can be calculated as

$$\boldsymbol{\tau}_{\mathrm{ext}} = \mathbf{J}^{\mathrm{T}}(\mathbf{q})\mathbf{w}_{\mathrm{ext}}. \tag{2.7}$$

Finally, by including Eq. (2.7) in the general robot dynamics from Eq. (2.5) and rearranging it, the external end effector wrench can be calculated as

$$\mathbf{w}_{\mathrm{ext}} = \mathbf{J}^{\mathrm{T}}(\mathbf{q})^{-1}\Big(\mathbf{M}(\mathbf{q})\ddot{\mathbf{q}} + \mathbf{C}(\mathbf{q}, \dot{\mathbf{q}})\dot{\mathbf{q}} + \mathbf{g}(\mathbf{q}) + \boldsymbol{\epsilon}(\mathbf{q}, \dot{\mathbf{q}}, \ddot{\mathbf{q}}) - \boldsymbol{\tau}\Big). \tag{2.8}$$

When performing robotic US examinations, the movements of the robot are usually slow and continuous. This is also described as quasi-static motion, in which velocities $\dot{\mathbf{q}}$ and accelerations $\ddot{\mathbf{q}}$ tend towards zero. Thus, the influence of inertial, centrifugal, and Coriolis forces is reduced to a level where they can be neglected. This simplifies the model for external wrench estimation to

$$\mathbf{w}_{\mathrm{ext}} = \mathbf{J}^{\mathrm{T}}(\mathbf{q})^{-1}\Big(\mathbf{g}(\mathbf{q}) + \boldsymbol{\epsilon}(\mathbf{q}, \dot{\mathbf{q}}, \ddot{\mathbf{q}}) - \boldsymbol{\tau}\Big). \tag{2.9}$$

2.3.3 Workspace and Reachability

The workspace of a manipulator refers to the reachable area in Cartesian space accessible by its end effector. Depending on the capabilities of the manipulator, this area can be a three-dimensional volume or a two-dimensional surface. The kinematic structure of the manipulator, defined by the arrangement and type of joints, determines the geometric constraints that shape the workspace. These constraints are further restricted by the mechanical limits of each joint, defining the maximum range of motion for each link.

The term reachability has its origin in describing the ability of a robot, if certain target poses can be reached at all or not [30]. This allows to extract areas that can be

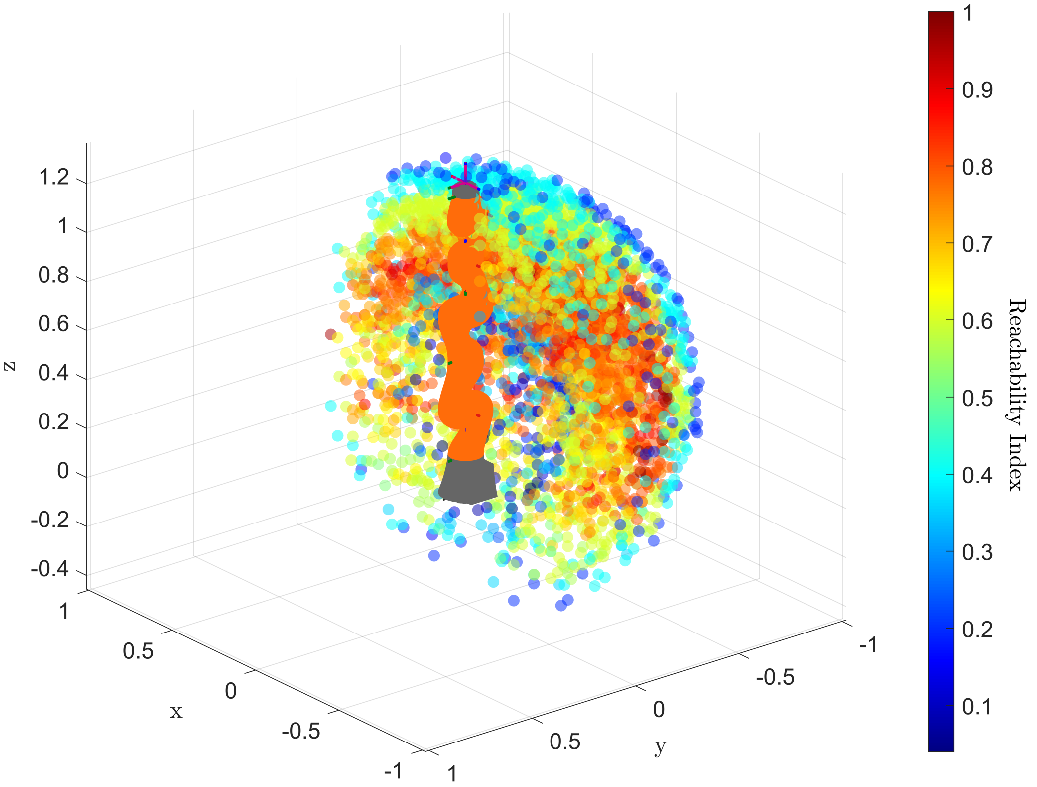

Figure 2.7: Exemplary visualization of a reachability map of the LBR iiwa 7. The map was generated with the Reachability Map toolbox for Matlab Simulink [35]. For better visibility, only half of the map is shown.

accessed within the robot's workspace for a specific scenario, e.g. in the presence of obstacles. In addition, reachability is often used in combination with a score, which provides an indication of how well the respective target pose can be reached. This score can be determined, for example, from the number of available solutions for the inverse kinematics. Another metric to quantify the reachability was introduced by Yoshikawa and referred to as manipulability index. This is a quality measure for redundant manipulators [31], describing the distance to singular configurations [32]. In other words, it can be quantified how easily the position and orientation of the end effector can be adjusted in a certain configuration [33]. The manipulability index is defined as a scalar value w given by

$$w = \sqrt{\det(\mathbf{J}(\mathbf{q}) \cdot \mathbf{J}(\mathbf{q})^{\mathrm{T}})}, \tag{2.10}$$

where $\mathbf{J}(\mathbf{q})$ is the Jacobian to a joint configuration $\mathbf{q}$. If a reachability value is calculated for each point in the workspace of a robot, a reachability map (RM) can be generated. This is a voxelized grid, either in 3D (only the positions of the end effector) or in 6D (positions and orientations of the end effector), with information on how well the corresponding voxels of the grid can be reached by the robot [34]. An exemplary RM is shown in Figure 2.7. The grid voxels are represented as colored spheres ranging from blue, through green and yellow to red, with blue representing low reachability and red representing high reachability.

The evaluation of the manipulability or reachability of a robot are well-known methods to assess the ability to maneuver in a given workspace [36], [37]. Thus, it offers a benefit for a number of applications in the field of robot manipulation. It is applied, for example, to support decision-making processes such as the selection of appropriate grasping poses in mobile or humanoid robotics [36] or appropriate positioning of a workpiece in a manufacturing cell [38], [39].

3 ROBOT-PATIENT POSITIONING[1]

An important aspect for successful robotic US examinations is the correct robot-patient positioning in the pre-scanning phase. On the one hand, this ensures that all target poses on the patient that are to be scanned with the US probe are within the robot's working range and therefore can be reached at all. On the other hand, optimized robot-patient positioning can increase the maneuverability of the robot at defined target poses. This refers to the ability to change the pose of the end effector, also known as reachability. A higher reachability means a greater range of possible movements in this specific configuration, which is beneficial for the robot's motion planning and force estimation capabilities. Optimal robot-patient positioning with respect to high reachability depends on two factors, the actual placement of the robot's base itself in relation to the patient and the transformation from the robot's flange to the tool center point (TCP) of the probe (see Figure 3.1).

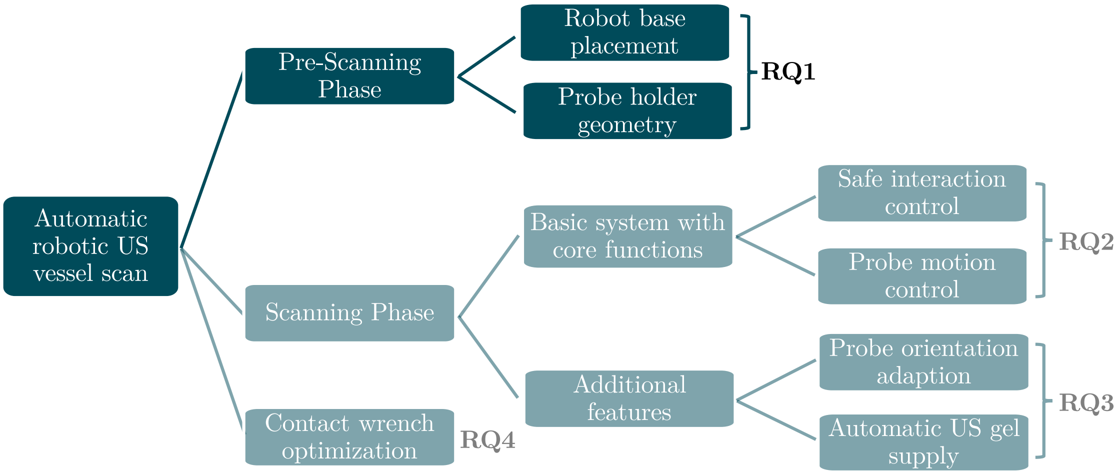

Figure 3.1: Structure of the thesis. The essential topics required for an automatic robotic US examination are addressed in individual chapters, with the content of this chapter highlighted in dark blue.

The transformation from the robot's flange to the probe's TCP results from the geometry of the probe holder, which can be adapted. The following research question is therefore investigated:

---

[1] Parts of this chapter have been published in [40].

Research Question 1
How can a probe holder be designed to maximize the reachability of target poses?

In the following sections, a method is proposed to determine an improved tool geometry. This increases the reachability of the target poses and allows a more favorable base positioning of the robot.

3.1 Related Work - Robot Base Placement

The determination of suitable placements of a robot base for defined TCP paths is achieved using reachability inversion. For this purpose, reachability maps (RMs), which describe how well a robot can reach different poses in its environment (see Section 2.3.3), are inverted. The results are referred to as inverse reachability maps (IRMs) [34], [41]. IRMs characterize the reachability of a given TCP pose relative to the robot base pose as defined in the TCP's reference frame. By using IRMs, optimal base positions of mobile manipulators [41], [42] or stance placements of humanoids [43] can be identified. Moreover, orientation-based reachability maps were introduced, which allow incorporating different tool geometries and task paths specified in the tool frame [44]. Other constraints, such as the surface geometry, can also be included, as shown in [45]. Further current research can be found in the field of industrial robotics. Here, the optimal positions of either the robot base or the workpiece must be determined, as they are essential to optimize the execution of robotic tasks. Precise workpiece positioning ensures that the available joint capabilities meet or exceed task requirements, particularly in collaborative robots with reduced motion capacities. For instance, in [38] the optimum positioning of a workpiece in the robot's workspace is determined in order to fulfil specified surface machining tasks that require the lowest possible joint speeds for execution. Another work presents a non-linear optimization algorithm. This can be used to determine the optimal workpiece pose that allows a robot to perform surface machining tasks with configurations that minimize joint torque requirements while maximizing manipulability [39]. In [46] a strategy for the placement of mobile manipulators is developed on the basis of different manipulability measures. With respect to specific demands of different tasks, such as the need for high-speed movements, large forces, high accelerations, or increased stiffness, a suitable base position can be determined. Further approaches for automated robot arrangement in manufacturing cells are presented for pick-and-place sequences [47], [48] and Tailored Forming [49]. Moreover, a multi-robot car-painting scenario is considered in [50]. Two cost functions are developed that explicitly represent the objectives of maximizing paint coverage and minimizing collision risk. These cost functions are then used to define a multi-objective optimization problem that can be solved using a multi-objective optimizer. An approach for co-optimization of robot, environment and tool design concerning motion planning is described by Toussaint et al.[51] Depending on the application, the geometry of the robot and the design of the tool can be adapted, thus increasing the effectiveness of the execution of the corresponding task. However, the resulting robot geometries are currently only theoretically possible, as custom link shapes are required. In the context of robotic US, a kinematic optimization for the design of a collaborative robotic end effector for tele-echography is presented [52]. The optimum base position and the tool geometry of a robot are determined with respect to a manipulability measure based on optimization. As a result, one optimal value was obtained for the base placement and tool geometry. However, in a realistic setup, it could be beneficial if there were several good options in terms of base placement and tool geometry instead of one perfect option, as the optimization is only valid for one specific case. Thus, the following sections propose an approach to calculate distributions of all possible base positions for defined target poses in the context of robotic US. These distributions could be used to simplify the placement of a robot. Furthermore, it is analyzed how the reachability of the target poses can be increased by an improved geometry of the probe holder.

3.2 Experimental Setup

The experimental setup is shown in Figure 3.2 and involves a patient lying on a couch, while a seven DoF redundant robot is moving an US probe attached to the end effector by a custom-developed probe holder. The robot used in the experiments is the LBR iiwa 7. Different target poses to be scanned are defined to investigate various applications. Firstly, a general case is considered in which *target pose 1*, *target pose 2*, and *target pose 3* are different transducer poses arranged around the patient. The target poses are located on the patient's semi-cylindrical safety shell, with the target orientation being the surface normal, as shown in Figure 3.3. These target poses describe a potential application of a robotic US examination of the organs in the upper body, such as the liver, for which the probe is placed either centrally on the patient's abdomen (like *target pose 3*) or laterally on the rib cage (like *target poses 1* and *2*). In a more advanced scenario, robotic US could be used in radiotherapy of liver tumors [53], [54]. Due to the irradiation, no staff can be present in the treatment room, therefore a robot is ideal for holding the US probe. It is important that the correct positioning of the robot is planned in advance to avoid interrupting the treatment. In addition, a 20 cm long path is considered for robotic US scanning of the femoral artery, inspired from the volunteer study described in Chapter 4. The path consists of three poses arranged in sequence with the same orientation and is referred to as *vessel path*.

The safety shell around the patient in Figure 3.2 represents the area in which no part of the robot, except for the US probe holder, must be located. Two scenarios for potential robot placements are considered. In scenario 1, both sides of the patient are available for robot positioning. In scenario 2, the possible locations for the robot are reduced due to the consideration of a forbidden translucent red box as shown in Figure 3.2 which represents an area for other medical equipment (e.g. a linear accelerator (LINAC)) or medical staff on one patient's side. Thus, the target pose must be approached from the other side of the patient, which makes it more difficult to reach the pose.

The probe holder's geometry is defined by the transformation ${}^{\mathrm{ee}}\mathbf{T}_{\mathrm{tcp}}$ from the end effector to the TCP. The reference probe holder geometry is defined as a pure translational extension of 0.1 m in the z-direction of the end effector (see Figure 3.4A).

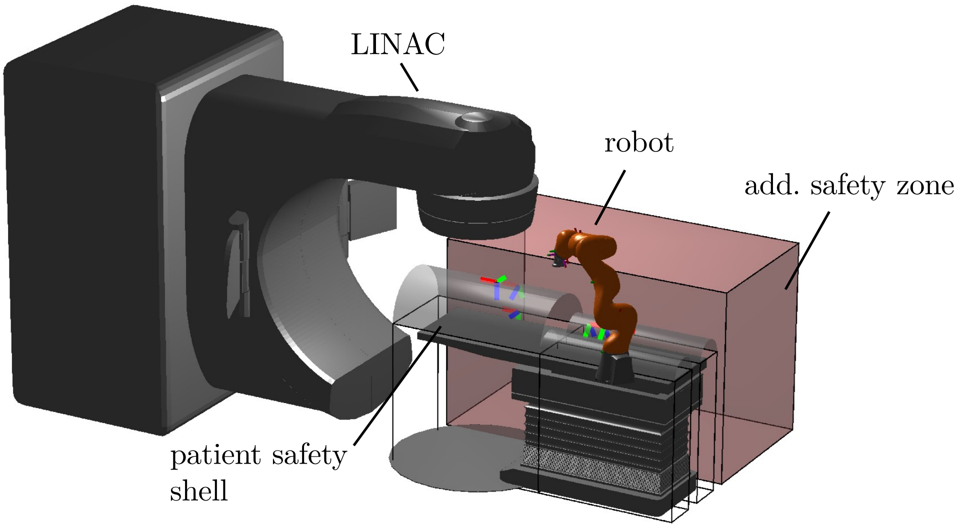

Figure 3.2: Experimental setup consisting of a patient couch and a redundant robot. For optimal robot base placement, two scenarios are considered, where in scenario 1 the robot can be positioned on both sides of the patient. In scenario 2, one patient side is restricted, e.g. by other medical equipment or staff, represented by the translucent red box. For example, the rotating irradiation unit of a LINAC could occupy one side of the patient to irradiate a certain target in the body, which is tracked using robotic US. The figure was created using the Robotics System Toolbox for Matlab Simulink [27] and a 3D model of the LINAC from [55].

The length of 0.1 m of the probe holder represents the minimum possible length for the straight attachment of the experimental US probe to the end effector. This setting allows us to use a small probe, but the cable must be bent for mounting. For the adapted tool geometries, the tool length is held constant, but it is attached to the end effector at a variable angle, represented by a rotation matrix $\mathbf{R}_{\text{tool}}$ (see Figure 3.4B). Thus, the probe holder geometry for a target pose j is defined by the following transformation matrix:

$$ {}^{\text{ee}}\mathbf{T}_{\text{tcp}} = \begin{pmatrix} & & & 0 \\ & \mathbf{R}_{\text{tool}} & & 0 \\ & & & 0 \\ 0 & 0 & 0 & 1 \end{pmatrix} \cdot \begin{pmatrix} 1 & 0 & 0 & 0 \\ 0 & 1 & 0 & 0 \\ 0 & 0 & 1 & 0.1 \\ 0 & 0 & 0 & 1 \end{pmatrix} = \begin{pmatrix} \mathbf{R}_{1,1} & \mathbf{R}_{1,2} & \mathbf{R}_{1,3} & 0.1\ \mathbf{R}_{1,3} \\ \mathbf{R}_{2,1} & \mathbf{R}_{2,2} & \mathbf{R}_{2,3} & 0.1\ \mathbf{R}_{2,3} \\ \mathbf{R}_{3,1} & \mathbf{R}_{3,2} & \mathbf{R}_{3,3} & 0.1\ \mathbf{R}_{3,3} \\ 0 & 0 & 0 & 1 \end{pmatrix}. \quad (3.1) $$

3.3 Generation of Reachability and Inverse Reachability Map

The approach presented to determine suitable robot base placements with high reachability for a defined target pose is based on an IRM. The IRM is created from a RM, which needs to be calculated first. The respective steps are explained below.

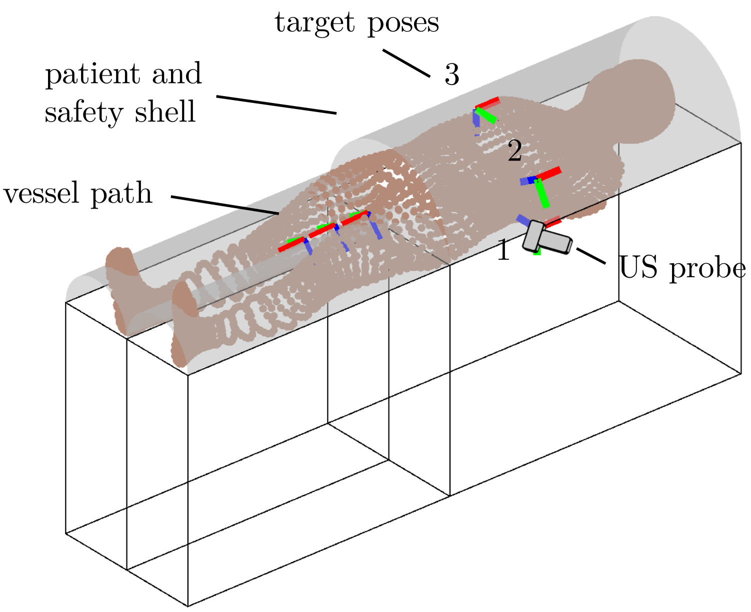

Figure 3.3: Visualization of the target poses on the patient to be scanned by the US probe. *Target poses 1, 2,* and *3* describe a potential robotic US examination of the organs in the upper body, such as the liver. In addition, the *vessel path* is considered for robotic US scanning of the femoral artery.

3.3.1 Workspace Sampling

The desired reachability map to be generated is a 6D map that represents the values for the reachability of every end effector pose in the workspace of the robot. First, a 3-dimensional grid with a resolution of 0.1 m is created as visualized in Figure 3.5A, resulting in 2,601 voxels. Every voxel is represented by a unit sphere whose center is the end effector position. To achieve a uniform distribution of the end effector orientations, 50 points are evenly distributed on the surface of each unit sphere by minimizing the electrostatic potential energy of a system of charged particles [56]. The direction from any point on the surface to the center of the sphere represents the direction of the ${}^{ee}z$-axis, as shown in Figure 3.5B. The ${}^{ee}x$- and ${}^{ee}y$-axes are tangential to the sphere surface. Each of these end effector orientations is additionally rotated around its ${}^{ee}z$-axis in a range from -180° to 150° in 30° steps, which results in a variation of the directions of the ${}^{ee}x$- and ${}^{ee}y$-axes. For the sake of clarity, only three of these 12 rotated poses belonging to one ${}^{ee}z$-axis orientation are shown in Figure 3.5C. In summary, for each of the 2,601 end effector positions, 600 different orientations are considered. This leads to a total number of 1,560,600 sampled poses, for which reachability values must be calculated and stored in the RM.

3.3.2 Measure of Reachability

To calculate values for reachability corresponding to the sampled poses, all poses are searched for valid solutions for inverse kinematics. Since a redundant robot is used, the elbow angle is specified as an additional varying parameter to take the nullspace into account. The elbow angle is defined as the angle which describes the

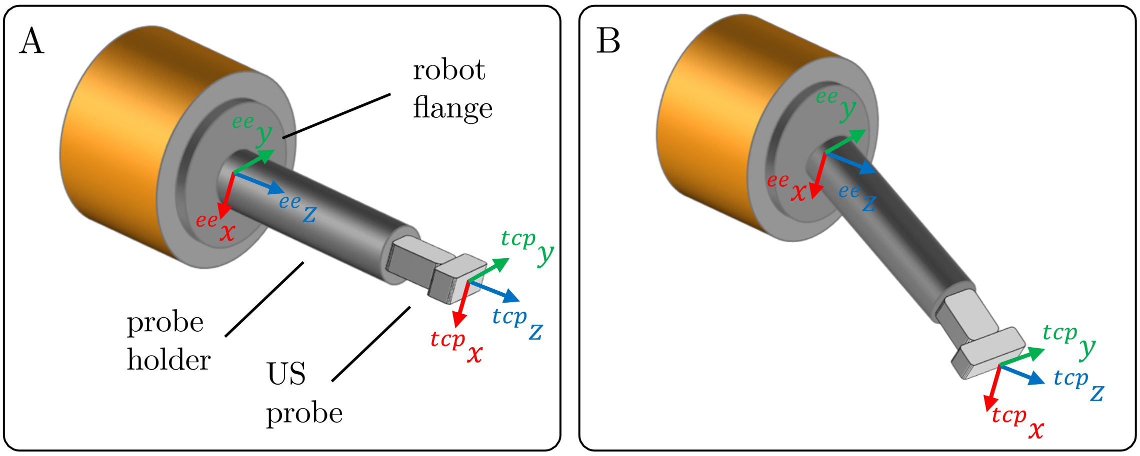

Figure 3.4: **A:** Reference probe holder geometry, which is a simple translational extension to the end effector by 0.1 m. **B:** Example of an adapted probe holder geometry, where a rotation $\mathbf{R}_{\mathrm{tool}}$ is applied to the reference tool geometry, resulting in an adjusted transformation matrix ${}^{\mathrm{ee}}\mathbf{T}_{\mathrm{tcp}}$ from the robot's flange to the probe's TCP.

rotation of the elbow around the axis from the shoulder to the wrist. Thus, each of the 1,560,600 poses is checked for solutions of inverse kinematics, varying the angle α_{n} of the elbow uniformly in 15 steps of 24° between 0° and 336°. The joint configurations $\mathbf{q}_{\mathrm{i},\alpha_{\mathrm{n}}}$, resulting from the analytical inverse kinematics calculation [57] for all elbow configurations α_{n} with $n \in \{1, \ldots, 15\}$ belonging to a sampled pose i are checked for joint limits and self-collisions and stored. The reachability value for each 6D entry of the RM is calculated as follows:

$$d_i = \sum_{n=1}^{15} \sqrt{\det(\mathbf{J}_{\mathrm{q_i},\alpha_{\mathrm{n}}} \cdot \mathbf{J}^{\mathrm{T}}_{\mathrm{q_i},\alpha_{\mathrm{n}}})}. \tag{3.2}$$

In Eq. 3.2, $\mathbf{J}_{\mathrm{q_i},\alpha_{\mathrm{n}}}$ represents the Jacobian of the configuration $\mathbf{q}_{\mathrm{i},\alpha_{\mathrm{n}}}$, where i is the respective grid pose and α_{n} the robot's elbow angle. The sum of Yoshikawa's manipulability indices $\sqrt{\det \mathbf{J} \cdot \mathbf{J}^{\mathrm{T}}}$ for all possible configurations to reach a defined pose i is calculated. Yoshikawa's manipulability index represents a measure of how well an adjustment is possible in the respective configuration [31], [36]. Thus, high values of d_{i} represent high reachability of the robot at the corresponding pose i in the RM.

3.3.3 Reachability Inversion

The reachability of the robot flange from Section 3.3.2 is defined with respect to a fixed robot base pose. The RM consists of tuples $(\mathbf{T}_{\mathrm{i}}, d_{\mathrm{i}})$, where $\mathbf{T}_{\mathrm{i}}$ are base-to-flange transformations and d_{i} are corresponding reachability values. Inverting the reachability data will lead to potential base poses for a fixed flange pose in the workspace. To generate an IRM, a second voxelized data grid is filled by tuples $(\mathbf{T}_{\mathrm{i}}^{-1}, d_{\mathrm{i}})$, where $\mathbf{T}_{\mathrm{i}}^{-1}$ represents the inverted poses of the RM, i.e. the flange-to-base transformation [41].

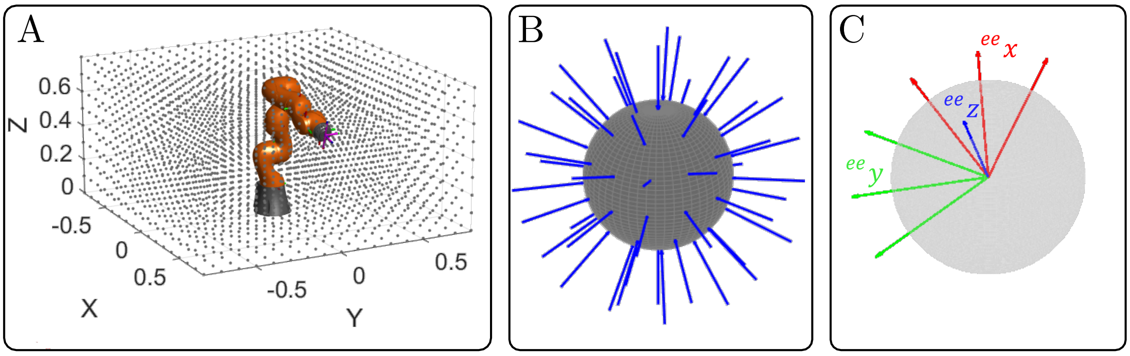

Figure 3.5: **A:** Considered workspace of the robot, consisting out of 2,601 positions represented by the centers of unit spheres. The dimensions of the workspace are $x \in [-0.8, 0.8]$, $y \in [-0.8, 0.8]$ and $z \in [0, 1]$, the resolution is 0.1 m. The figure was created with support of the Robotics System Toolbox for Matlab Simulink [27]. **B:** 50 orientations of the ${}^{ee}z$-axis (shown in blue), defined by the direction from uniformly distributed points on the surface to the center of the sphere. **C:** Each of these 50 orientations is additionally rotated by 30° steps in a range from -180° to 150° to include all possible rotations around the ${}^{ee}z$-axis. To provide a better overview, only three rotations are shown. The ${}^{ee}x$-axes are red, while ${}^{ee}y$-axes are represented by green arrows.

3.4 Robot Base Placement

The procedure for finding safe and valid robot base poses is illustrated in Figure 3.6. First, the IRM is used to determine all potential robot base poses (see Section 3.4.1) which also include those with an oblique base. In a realistic use case, the orientation of the robot's base is fixed and upright, and hence, the poses with an upright base are extracted from the set of all potential poses. For the remaining inclined robot bases, the required rotation matrix of the tool transformation is calculated so that the robot base is aligned upright and the transformation from the base to the end effector remains the same (see Section 3.4.2). Finally, all robot configurations used to calculate the reachability values belonging to the upright base positions are checked for collisions with the safety zone (see Section 3.4.3). If collisions are detected, these joint configurations are not possible and corresponding reachability values must be reduced accordingly.

3.4.1 Potential Robot Base Poses

The IRM was generated for end effector poses (see Section 3.3.3). This means that end effector poses must also be provided to use the IRM for determining potential robot base poses. For this purpose, the end effector target poses $\mathbf{P}_{\mathrm{target,ee,j}}$ associated with the TCP target areas (*target poses 1, 2, 3, vessel path*) are calculated by

$$\mathbf{P}_{\mathrm{target,ee,j}} = \mathbf{P}_{\mathrm{target,tcp,j}} \cdot {}^{\mathrm{tcp}}\mathbf{T}_{\mathrm{ee,ref}} \tag{3.3}$$

where j is the corresponding goal pose index and ${}^{\mathrm{tcp}}\mathbf{T}_{\mathrm{ee,ref}}$ represents the transformation from the TCP to the end effector for the reference probe holder geometry without any rotation at the end effector (see Figure 3.4A). All potential robot base poses $\mathbf{B}_{\mathrm{i,j}}$ for the end effector target pose $\mathbf{P}_{\mathrm{target,ee,j}}$ can then be determined by

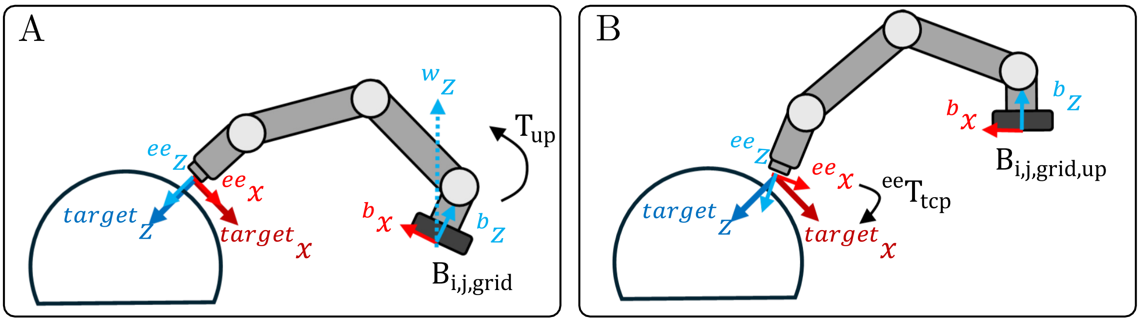

Figure 3.6: Base Placement Process. **A:** Exemplary potential robot base pose $\mathbf{B}_{\mathrm{i,j,grid}}$, where the ${}^{base}z$-axis is aligned obliquely. **B:** The oblique base was aligned upright by applying transformation $\mathbf{T}_{\mathrm{up}}$ and shifted accordingly so that the end effector position is retained. The resulting base position is referred to as $\mathbf{B}_{\mathrm{i,j,grid,up}}$.

multiplying the end effector target pose with the transformations $\mathbf{T}_{\mathrm{i}}^{-1}$ of the IRM:

$$\mathbf{B}_{\mathrm{i,j}} = \mathbf{P}_{\mathrm{target,ee,j}} \cdot \mathbf{T}_{\mathrm{i}}{}^{-1}. \tag{3.4}$$

Each of the potential robot base poses is assigned the corresponding reachability value d_{i} (see Eq. 3.2) from the tuple $(\mathbf{T}_{\mathrm{i}}^{-1}, d_{\mathrm{i}})$ of the IRM. The potential base poses are allocated to a five-dimensional grid consisting of three translational and two rotational parameters. The translational resolution for the x-, y-, z-coordinates of the grid points is 0.1 m. For each grid point, 25 different directions of the ${}^{base}z$-axis are considered, covering a half-sphere with a maximum inclination angle of 90°, so no robot bases hanging downwards are considered. Again, the ${}^{base}z$-axis orientations are defined by the direction from uniformly distributed points on the surface to the center of a unit-sphere. A nearest neighbor algorithm is used to assign each of the potential base poses $\mathbf{B}_{\mathrm{i,j}}$ to the nearest entry in this five-dimensional grid, referred to as $\mathbf{B}_{\mathrm{i,j,grid}}$. The respective reachability values belonging to a grid entry are averaged and referred to as $d_{\mathrm{i,j,grid}}$.

To represent the reachability of a whole path, consisting of multiple target poses reached sequentially, the potential base positions $\mathbf{B}_{\mathrm{i,j,grid}}$ for the different target poses are combined. For each grid point, the respective reachability value is represented by the mean value of the entries for the different target poses $j \in \{1, \ldots, k\}$.

$$d_{\mathrm{i,path,grid}} = mean(d_{\mathrm{i,j,grid}})_{j=1}^{k}. \tag{3.5}$$

So far, no constraints have been applied to the potential robot base poses. This means that any position and inclination of the ${}^{base}z$-axis of the robot is possible, exemplarily shown in Figure 3.6A.

3.4.2 Compensation of Base Orientation Constraint by Tool Geometry

In the considered scenario, the robot base position can be varied in x-,y- and z-directions as long as it does not fall within the range of the safety zone. Moreover, it is assumed that the base is oriented in an upright position, with rotations around its ${}^{base}z$-axis possible. This assumption is made because it represents a realistic scenario, with a robot available in the treatment room, mounted upright on a mobile platform. Thus, the robot's base position can be varied in x- and y-direction and rotated around its ${}^{base}z$-axis. Furthermore, the height of the patient couch can be adjusted, and thus the relative displacement between the robot base and the patient in z-direction.

Out of all possible base poses $\mathbf{B}_{\mathrm{i,j,grid}}$ of the robot, there are only a few for which the ${}^{base}z$-axis is already aligned in the direction of the ${}^{world}z$-axis. Many base poses with high reachability values are orientated obliquely. For this reason, the goal is to calculate a tool transformation to compensate for oblique orientations of the robot's ${}^{base}z$-axis and thus be able to improve the reachability of an upright-oriented robot for specific target poses. For this purpose, the necessary rotation matrices are calculated to rotate the obliquely oriented robot bases $\mathbf{B}_{\mathrm{i,j,grid}}$ to be upright. This is done by determining the axis $\mathbf{u}$ and angle θ between the oblique ${}^{base}z$-axis $\mathbf{z}_{\mathrm{i,j,obl}}$ and the upright ${}^{world}z$-axis $\mathbf{z}_{\mathrm{up}}$:

$$\mathbf{u}_{\mathrm{i,j}} = \frac{\mathbf{z}_{\mathrm{i,j,obl}} \times \mathbf{z}_{\mathrm{up}}}{||\mathbf{z}_{\mathrm{i,j,obl}} \times \mathbf{z}_{\mathrm{up}}||} \tag{3.6}$$

$$\theta_{\mathrm{i,j}} = \cos^{-1}\left(\frac{\mathbf{z}_{\mathrm{i,j,obl}} \cdot \mathbf{z}_{\mathrm{up}}}{||\mathbf{z}_{\mathrm{i,j,obl}}|| \cdot ||\mathbf{z}_{\mathrm{up}}||}\right). \tag{3.7}$$

The robot is rotated by the transformation matrix $\mathbf{T}_{\mathrm{i,j,up}}$ corresponding to the rotation by axis $\mathbf{u}_{\mathrm{i,j}}$ and angle $\theta_{\mathrm{i,j}}$, which results in the following robot's base pose:

$$\widetilde{\mathbf{B}}_{\mathrm{i,j,grid,up}} = \mathbf{T}_{\mathrm{i,j,up}}(\mathbf{u}, \theta) \cdot \mathbf{B}_{\mathrm{i,j,grid}}. \tag{3.8}$$

The base of the robot is now aligned upright, but the pose of the end effector has changed to $\widetilde{\mathbf{T}}_{\mathrm{i,j,ee}}$ as a consequence of the rotation. The translational shift between the end effector pose before ($\mathbf{T}_{\mathrm{ee}}$) and after ($\widetilde{\mathbf{T}}_{\mathrm{i,j,ee}}$) the rotation is calculated and expressed as a transformation matrix $\mathbf{T}_{\mathrm{i,j,err}}$. Then, this shift is compensated for by relocating the base $\widetilde{\mathbf{B}}_{\mathrm{i,j,grid,up}}$ accordingly:

$$\mathbf{B}_{\mathrm{i,j,grid,up}} = \mathbf{T}_{\mathrm{i,j,err}} \cdot \widetilde{\mathbf{B}}_{\mathrm{i,j,grid,up}}. \tag{3.9}$$

The corrected base pose $\mathbf{B}_{\mathrm{i,j,grid,up}}$ ensures that the end effector is positioned as before (Figure 3.6B). However, there is still a difference in the desired end effector orientation. This difference is compensated for by a corresponding rotation $\mathbf{R}_{\mathrm{i,j,tool}}$ applied to the tool geometry, as shown in Eq. 3.1 and Figure 3.4B. The required tool rotation $\mathbf{R}_{\mathrm{tool}}$ is calculated by:

$$\mathbf{R}_{\mathrm{i,j,tool}} = \widetilde{\mathbf{R}}^{-1}_{\mathrm{i,j,ee}} \cdot \mathbf{R}_{\mathrm{j,ee}}. \tag{3.10}$$

$\widetilde{\mathbf{R}}_{\mathrm{i,j,ee}}$ represents the orientation of the end effector after the robot has been rotated by $\mathbf{T}_{\mathrm{up}}(u, \theta)$ to ensure an upright base alignment and $\mathbf{R}_{\mathrm{j,ee}}$ is the desired end effector orientation for the target pose j. The number of compensating tool rotations calculated in this manner therefore corresponds to the number of possible different base orientations $\mathbf{B}_{\mathrm{i,j}}$. The tool rotations $\mathbf{R}_{\mathrm{i,j,tool}}$ are clustered with the corresponding base rotations to be compensated and the mean value is determined. This results in 25 different tool geometries ${}^{\mathrm{tcp}}\mathbf{T}_{\mathrm{ee,t,i}}$ in the example shown, where t is the index of the tool geometry and i the target pose. Thus, the five-dimensional distribution of all potential base poses $\mathbf{B}_{\mathrm{i,j,grid}}$ can be reduced to 25 different three-dimensional distributions $\mathbf{B}_{\mathrm{i,j,grid,up}}$ of upright base poses with respective tool transformations.

3.4.3 Collision Check

The calculation of the reachability value d_i associated with a pose $\mathbf{T}_\mathrm{i}^{-1}$ in the IRM is based on the sum of Yoshikawa's manipulability indices of all possible configurations that can be used to approach this pose (see Eq. (3.2)). The angle of the elbow is varied in discrete steps. The more positions of the robot's elbow are possible, the higher the reachability value. However, this does not take into account the fact that a robot configuration may not be possible due to obstacles, which would reduce the reachability value. For that reason, all robot configurations used to calculate the reachability values belonging to the upright base poses $\mathbf{B}_\mathrm{i,j,grid,up}$ are checked for collisions with the safety zone. To do this, the positions of all robot joints are evaluated to determine whether they are located inside the patient safety zone. If collisions are detected, these joint configurations are not possible and corresponding reachability values are reduced accordingly. The corrected reachability values for the upright base poses $\mathbf{B}_\mathrm{i,j,grid,up}$ are denoted as $d_\mathrm{i,cor}$.

3.4.4 Base Poses Visualization

The adapted base positions $\mathbf{B}_\mathrm{i,j,grid,up}$ and their associated reachability values $d_\mathrm{i,cor}$ are finally assigned to the corresponding closest voxels of a 3-dimensional grid. For each grid voxel, the reachability values $d_\mathrm{i,cor}$ of the closest base positions are averaged. Thus, a grid voxel with its associated reachability value describes the probability of how suitable this position is for placing the upright robot base to reach the TCP target poses. To facilitate comparability, the reachability values associated with base positions are normalized to the highest occurring value of the respective target in scenario 1. For visualization purposes, the grid voxels are represented as colored spheres (e.g. see Figure 3.7). The colors range from blue, through green and yellow to red, with blue representing low reachability and red representing high reachability.

3.5 Results

The aim of this approach is to automatically determine the selection of an adapted tool geometry and thus increase the number of potential base positions with high reachability of an upright-orientated robot. Thus, distributions of upright base positions $\mathbf{B}_\mathrm{i,j,grid,up}$ for respective tool transformations $\mathbf{T}_\mathrm{i,j,tool}$ (see Section 3.4.2) were calculated for three defined target areas *target pose 1*, *target pose 2*, and *target pose 3* in two different scenarios. For evaluation purposes, the number of base positions with a high reachability value that can be realized by applying a corresponding tool transformation was counted. In the example presented, there are therefore 25 different distributions of upright base positions per target pose. In the following, the best distribution for each target pose and the scenario under consideration is shown. The distributions of the base positions without adapted tool geometry (${}^\mathrm{tcp}\mathbf{T}_\mathrm{ee,ref}$) are used for comparison.

3.5.1 Scenario 1: No Additional Workspace Restriction

In scenario 1, the robot's base can be located on both sides of the patient as long as the safety box is not violated. The respective distributions with the largest number of base positions having a reachability value greater than 0.75 are shown in Table 3.1 and compared to the values derived from the base positions without corrected tool geometry (${}^{\text{tcp}}\mathbf{T}_{\text{ee,ref}}$). In addition, the base positions are visualized in Figure 3.7, Figure 3.8, Figure 3.9 and Figure 3.10. The resulting optimized tool geometries ${}^{\text{tcp}}\mathbf{T}_{\text{ee,max}}$ are shown in Figure 3.11 and Figure 3.12.

For *target pose 1*, the number of base positions with a reachability value higher than 0.75 could be increased from 58 to 89 by using an adapted tool geometry, which is an increase of about 52 %. The respective base positions are visualized in Figure 3.7 as the larger reddish spheres. In Figure 3.7B, many more large reddish spheres can be seen, as an adapted tool geometry is used compared to Figure 3.7A, where the reference tool geometry is taken. This is confirmed by the histogram showing higher bars for high reachability values. Furthermore, it can be seen that reaching the target pose from the other side of the patient can now be achieved by using the adapted tool geometry (Figure 3.7B). This is possible due to the corresponding tool geometry, which has a mounting angle at the end effector of about 49.2° (Figure 3.11A), as this allows the robot to approach the target area without excessively tilting its effector over the patient.

For *target pose 2*, 90 base positions of high reachability can be realized with an adapted tool geometry, as shown in Table 3.1 and Figure 3.8B. This is an improvement of 29 % w.r.t the usage of the standard tool geometry, which only provides 70 positions, as shown in Figure 3.8A. The increase can also be seen in the histogram bars of high reachability values next to the base distributions, although not as clearly as for *target pose 1*. *Target pose 2* can also only be achieved from the other side of the patient with an adapted tool transformation. The corresponding tool geometry has a mounting angle of about 23.3° (3.11B), which is smaller than for *target pose 1*, as it requires less angulation of the end effector to reach *target pose 2* from the other side of the patient compared to *target pose 1*.

In contrast, for *target pose 3* the tool transformation that leads to the largest number of base positions with a reachability value of more than 0.75 is the same as the reference tool geometry (Figure 3.12A), which is why the same distributions can be seen in Figure 3.9A and Figure 3.9B. In addition, it can be observed, that *target pose 3* can easily be reached from both sides of the patient (Figure 3.9).

For the *vessel path*, a strong increase in base placements with high reachability can be achieved. Using an adapted tool geometry, 68 instead of 21 potential base positions using the reference tool can be obtained. This represents the largest relative increase compared to the other target poses. However, the absolute number of base positions with high reachability is much smaller for the *vessel path*, even for the adapted tool geometry. This is particularly noticeable for the reference tool, where only 21 possible base positions can be achieved compared to 58, 70, and 86 for the other target poses, respectively. The optimized tool geometry for the *vessel path* (Figure 3.12B) has a mounting angle of 39.4°. The tilt direction of this tool geometry is opposite to that of *target poses 1* and *2*, as the orientations of the poses of the *vessel path* are also reversed compared to *target poses 1* and *2*.

Table 3.1: Maximum number of possible base positions with a reachability value $d_{\mathrm{i,cor}} > 0.75$ for the corresponding optimized tool transformation ${}^{\mathrm{tcp}}\mathbf{T}_{\mathrm{ee,max}}$ for scenario 1. In addition, the maximum and mean of the considered reachability values are specified for each target pose. The values for the reference tool geometry ${}^{\mathrm{tcp}}\mathbf{T}_{\mathrm{ee,ref}}$ are given for comparison.

	No. of Bases		**Mean**		**Max**	
Target area	${}^{\mathrm{tcp}}\mathbf{T}_{\mathrm{ee,ref}}$	${}^{\mathrm{tcp}}\mathbf{T}_{\mathrm{ee,max}}$	${}^{\mathrm{tcp}}\mathbf{T}_{\mathrm{ee,ref}}$	${}^{\mathrm{tcp}}\mathbf{T}_{\mathrm{ee,max}}$	${}^{\mathrm{tcp}}\mathbf{T}_{\mathrm{ee,ref}}$	${}^{\mathrm{tcp}}\mathbf{T}_{\mathrm{ee,max}}$
Target Pose 1	58	89	0.82	0.83	0.97	0.94
Target Pose 2	70	90	0.82	0.82	0.95	0.96
Target Pose 3	86	86	0.83	0.83	0.98	0.98
Vessel Path	21	68	0.85	0.81	0.96	0.95

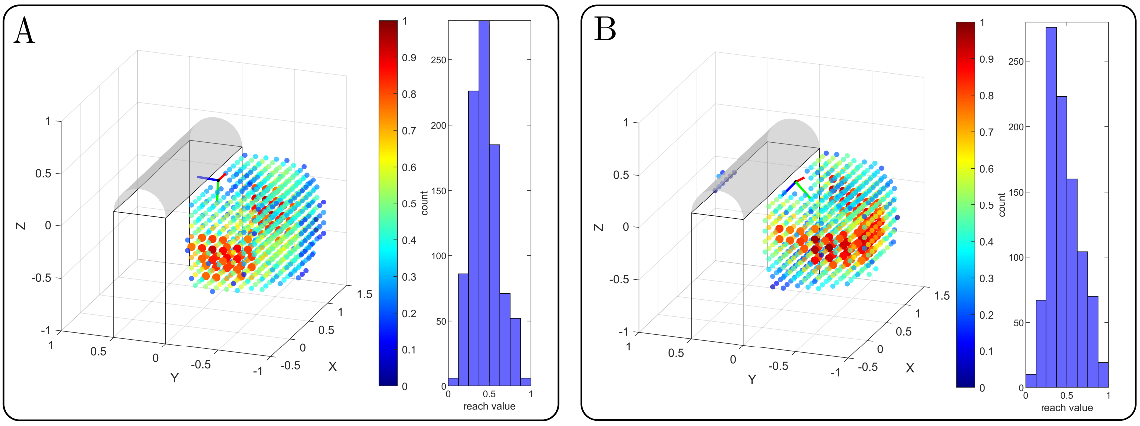

Figure 3.7: Visualization of upright base positions for *target pose 1* in scenario 1. **A** shows the base positions without adapted tool geometry (${}^{\mathrm{tcp}}\mathbf{T}_{\mathrm{ee,ref}}$). The potential base positions are represented by colored spheres, with the color indicating the reachability value. The base positions with a value of more than 0.75 are shown as larger spheres. Moreover, histograms of the respective distributions are shown. The visualized coordinate systems consisting of a red x-axis, green y-axis, and blue z-axis, represent the end effector target poses to be reached. In **B**, the distribution of base positions for the adapted tool geometry ${}^{\mathrm{tcp}}\mathbf{T}_{\mathrm{ee,max}}$, resulting in the maximum number of base positions with a reachability value $d_{\mathrm{i,cor}}{>}0.75$, is shown. Since an adapted tool geometry was used in **B**, the resulting flange target pose differs from **A**, where the reference geometry was applied without any rotation.

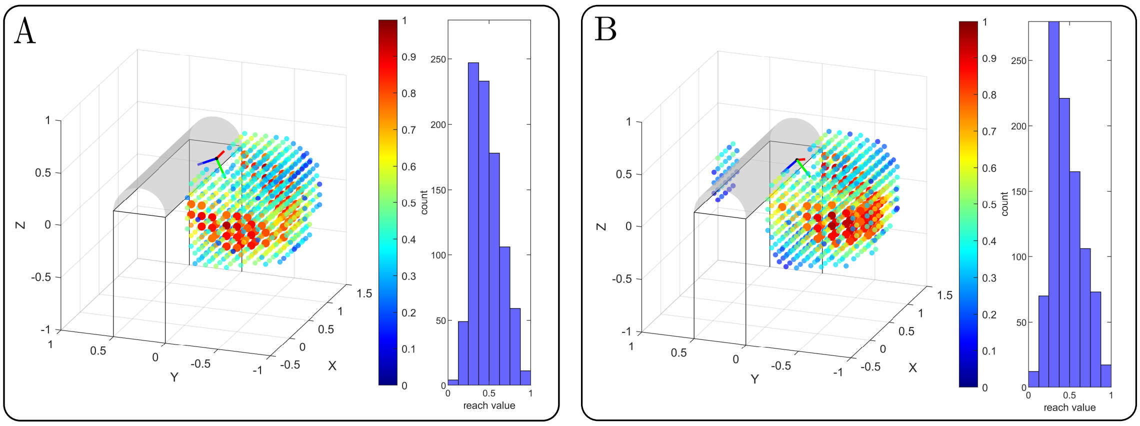

Figure 3.8: Visualization of upright base positions for *target pose 2* in scenario 1. In **A**, the base positions without adapted tool geometry ($^{\text{tcp}}\mathbf{T}_{\text{ee,ref}}$) are shown for comparison. In **B**, the distribution of base positions for the adapted tool geometry $^{\text{tcp}}\mathbf{T}_{\text{ee,max}}$, resulting in the maximum number of base positions with a reachability value $d_{\text{i,cor}}$>0.75, is shown.

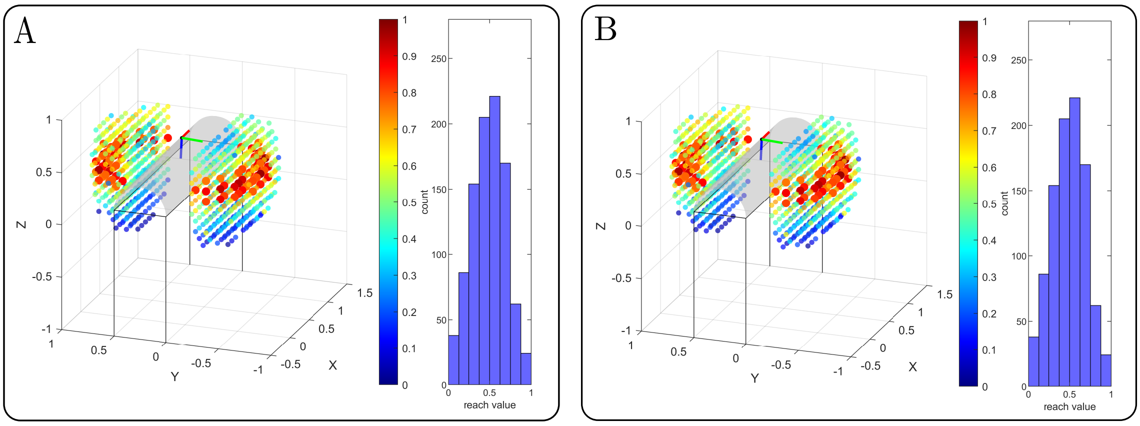

Figure 3.9: Visualization of upright base positions for *target pose 3* in scenario 1. In **A**, the distribution of base positions without adapted tool geometry ($^{\text{tcp}}\mathbf{T}_{\text{ee,ref}}$) is presented. It can be seen that this is the same distribution as in **B**, where the distribution of base positions for the adapted tool geometry $^{\text{tcp}}\mathbf{T}_{\text{ee,max}}$, resulting in the maximum number of base positions with a reachability value $d_{\text{i,cor}}$>0.75, is shown. Thus, for *target pose 3*, base positioning cannot be improved by an appropriate tool geometry.

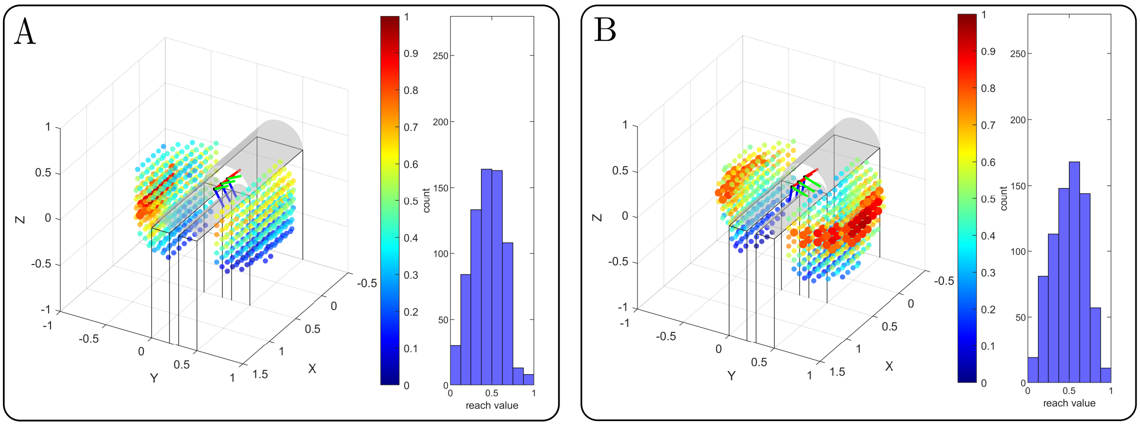

Figure 3.10: Visualization of upright base positions for the *vessel path* in scenario 1. In **A**, the base positions without adapted tool geometry (${}^{\text{tcp}}\mathbf{T}_{\text{ee,ref}}$) are shown for comparison. In **B**, the distribution of base positions for the optimized tool geometry ${}^{\text{tcp}}\mathbf{T}_{\text{ee,max}}$, resulting in the maximum number of base positions with a reachability value $d_{\text{i,cor}}$>0.75, is shown.

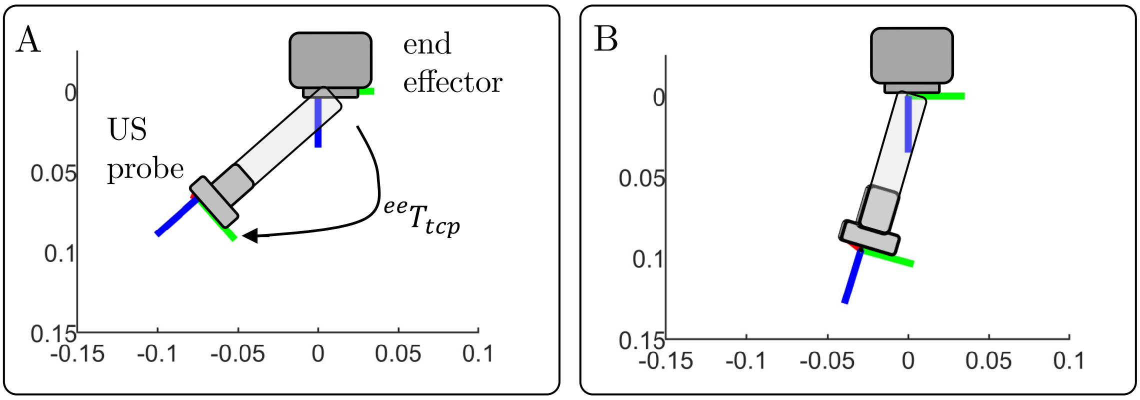

Figure 3.11: Visualization of resulting tool geometries ${}^{\text{tcp}}\mathbf{T}_{\text{ee,max}}$ in scenario 1. **A:** For *target pose 1* the rotation angle of ${}^{\text{tcp}}\mathbf{T}_{\text{ee,max}}$ is 49.2° with a rotation axis of $(0.99, 0, -0.16)^T$. **B:** The respective rotation angle of ${}^{\text{tcp}}\mathbf{T}_{\text{ee,max}}$ for *target pose 2* is 23.3° with an axis of $(0.69, 0.36, -0.63)^T$.

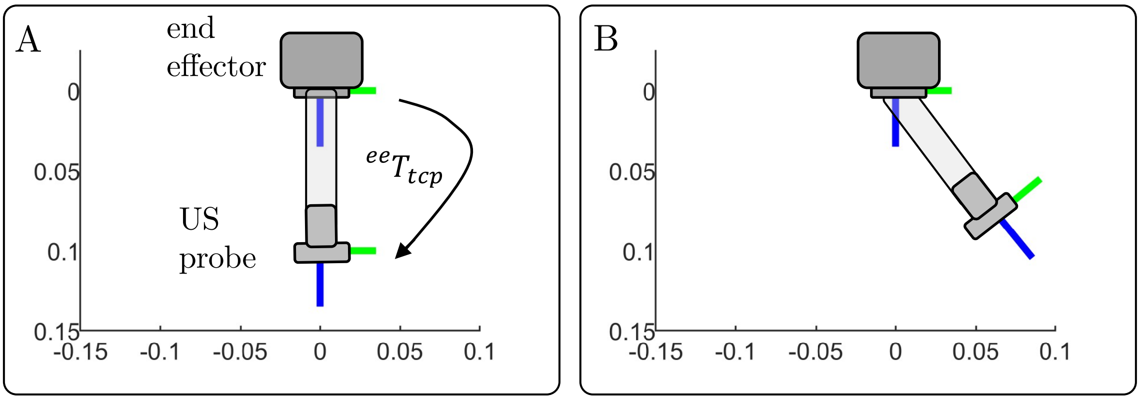

Figure 3.12: Visualization of resulting tool geometries ${}^{\text{tcp}}\mathbf{T}_{\text{ee,max}}$ in scenario 1. **A:** For *target pose 3*, base positioning cannot be improved by an adapted tool geometry. Thus, the best tool geometry is the reference tool geometry, which is simply a translational extension of the end effector. **B:** For the *vessel path* the rotation angle of ${}^{\text{tcp}}\mathbf{T}_{\text{ee,max}}$ is 39.4° with a rotation axis of $(-0.99, 0.06, -0.19)^T$.

3.5.2 Scenario 2: Additional Workspace Restriction

As can be seen from Figure 3.7A and Figure 3.8A, *target pose 1* and *target pose 2* can only be reached from one side unless a customized tool geometry is used. To further investigate that problem, another scenario is considered, where the preferred side is restricted and thus not available for placing the robot's base. For this scenario, the respective tool transformations are redetermined to enable most base positions on the other side of the patient with a reachability value $d_{\mathrm{i,cor}}>0.25$ for *target pose 1* and *target pose 2*. The limit value was reduced, as almost no base placements with reachability values in the very high range as previously analyzed ($d_{\mathrm{i,cor}}>0.75$) are possible for these two target poses. The resulting distribution for *target pose 1* is shown in Figure 3.13B and for *target pose 2* in Figure 3.14B. The number of possible base positions has been greatly reduced compared to scenario 1, as a large part of the possible range has now been restricted, which is shown by the translucent red boxes. Nevertheless, using adapted tool geometries, new base placements are found which helps to reach the target poses from the other side of the patient. This was previously not possible for both *target pose 1* and *target pose 2* without an adapted tool geometry, which is shown in Figure 3.13A and Figure 3.14A, where no colored spheres can be recognized. By mounting the US probe with a custom probe holder geometry on the robot, four base positions for *target pose 1* and 82 base positions for *target pose 2* with reachability $d_{\mathrm{i,cor}}>0.25$ can be found, also represented by the larger spheres in Figure 3.13B and Figure 3.14B. In addition, this is illustrated by Table 3.2. As expected, the average and maximum reachability values were lower for scenario 2 than in the unrestricted case of scenario 1. The resulting tool geometries are shown in Figure 3.17. It can be seen that the large angle (almost 90°) with which the probe is attached to the end effector increases the range of the robot. Thus, the target poses can be reached more easily, as the end effector no longer has to be tilted so much over the patient.

For *target pose 3*, there is a slight improvement from 42 to 55 potential base positions with a reachability value $d_{\mathrm{i,cor}}>0.75$ (see Table 3.2). Again, this can also be derived from the histograms in Figure 3.15. As the reachability of *target pose 3* was already very good with the reference tool (see Figure 3.15A), only a slight angulation can be recognized for the geometry of an adapted tool, shown in Figure 3.18A. An increase in base positions with high reachability can also be achieved for the *vessel path*. Similar to *target pose 3*, the probe is only slightly angled at the end effector (Figure 3.18B), but in the other direction. With this optimized tool geometry, 32 instead of 21 possible base positions with high reachability $d_{\mathrm{i,cor}}>0.75$ can be achieved, as is shown in Table 3.2 and Figure 3.16. In addition, it can be seen from Table 3.2 that the mean and maximum reachability values remain at a level similar to that without the adapted tool geometry for *target pose 3* as well as the *vessel path*.

Table 3.2: Maximum number of possible base positions with a reachability value $d_{\mathrm{i,cor}} > 0.25$ for *target pose 1* and *target pose 2* as well as $d_{\mathrm{i,cor}} > 0.75$ for *target pose 3* and the *vessel path* for the corresponding optimized tool transformation ${}^{\mathrm{tcp}}\mathbf{T}_{\mathrm{ee,max}}$ in scenario 2. The area for the robot to be placed is additionally restricted. In addition, the maximum and mean of the considered reachability values are specified. The values for the reference tool geometry ${}^{\mathrm{tcp}}\mathbf{T}_{\mathrm{ee,ref}}$ are given for comparison.

	No. of Bases		**Mean**		**Max**	
Target area	${}^{\mathrm{tcp}}\mathbf{T}_{\mathrm{ee,ref}}$	${}^{\mathrm{tcp}}\mathbf{T}_{\mathrm{ee,max}}$	${}^{\mathrm{tcp}}\mathbf{T}_{\mathrm{ee,ref}}$	${}^{\mathrm{tcp}}\mathbf{T}_{\mathrm{ee,max}}$	${}^{\mathrm{tcp}}\mathbf{T}_{\mathrm{ee,ref}}$	${}^{\mathrm{tcp}}\mathbf{T}_{\mathrm{ee,max}}$
Target Pose 1	–	4	–	0.31	–	0.34
Target Pose 2	–	82	–	0.49	–	0.72
Target Pose 3	42	55	0.82	0.83	0.98	0.96
Vessel Path	21	32	0.85	0.85	0.96	1.00

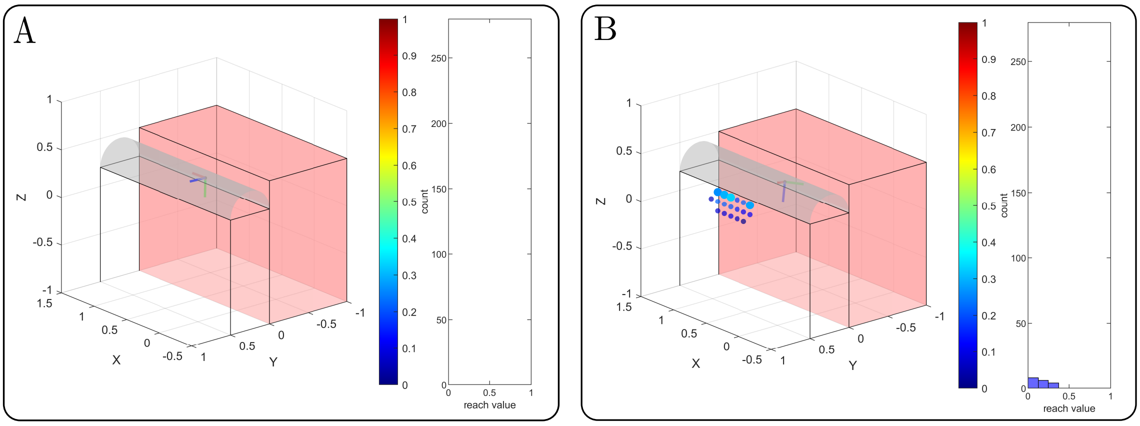

Figure 3.13: Visualization of upright base positions for *target pose 1* for scenario 2, where the area for potential base placements is strongly restricted, represented by the translucent red boxes. In **A**, no base positions can be found if no customized tool geometry is applied. The target flange pose cannot be reached from the other patient's side. However, this is possible if an adapted tool geometry is used. This can be seen in **B**, where the distribution of base positions for the optimized tool geometry, resulting in the maximum number of base positions with a reachability value $d_{\mathrm{i,cor}}$>0.25, is shown. The base positions with a value of more than 0.25 are shown as larger spheres.

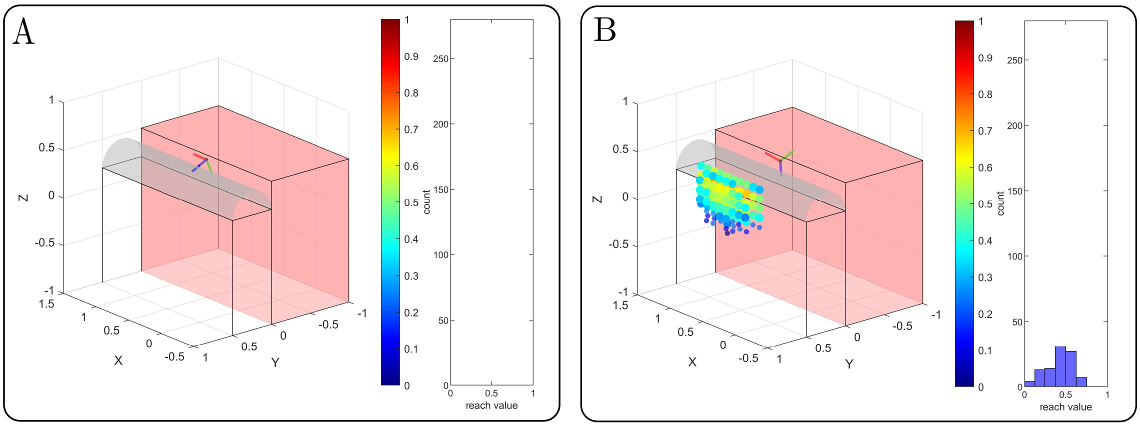

Figure 3.14: Visualization of upright base positions for *target pose 2* for scenario 2. In **A**, no base positions can be found if no adapted tool geometry is applied. In **B**, the distribution of base positions for the adapted tool geometry, resulting in the maximum number of base positions with a reachability value $d_{\mathrm{i,cor}}>0.25$, is shown. Due to the optimized tool geometry, the target pose can now be reached from the other side of the patient.

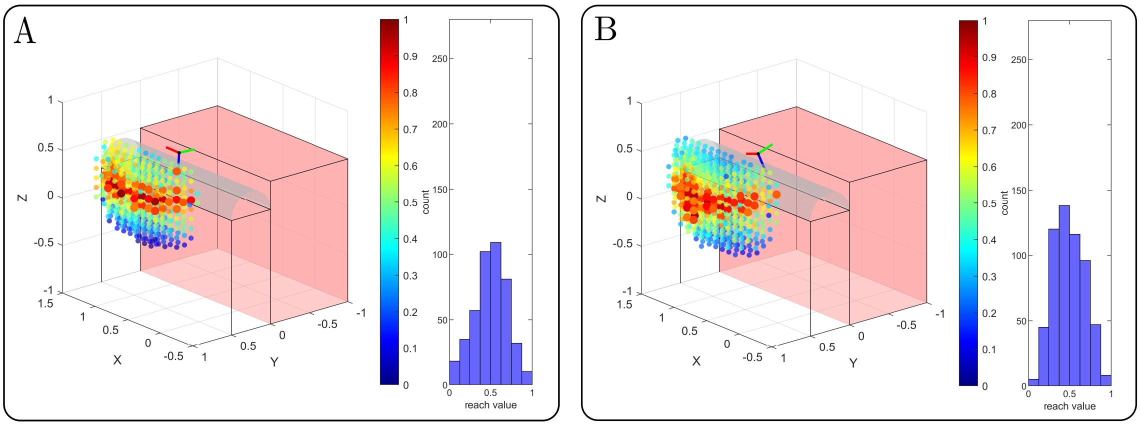

Figure 3.15: Visualization of upright base positions for *target pose 3* for scenario 2. **A** shows the base positions when no adapted tool geometry is applied. In **B**, the distribution of base positions for the optimized tool geometry, resulting in the maximum number of base positions with a reachability value $d_{\mathrm{i,cor}}>0.75$, is shown.

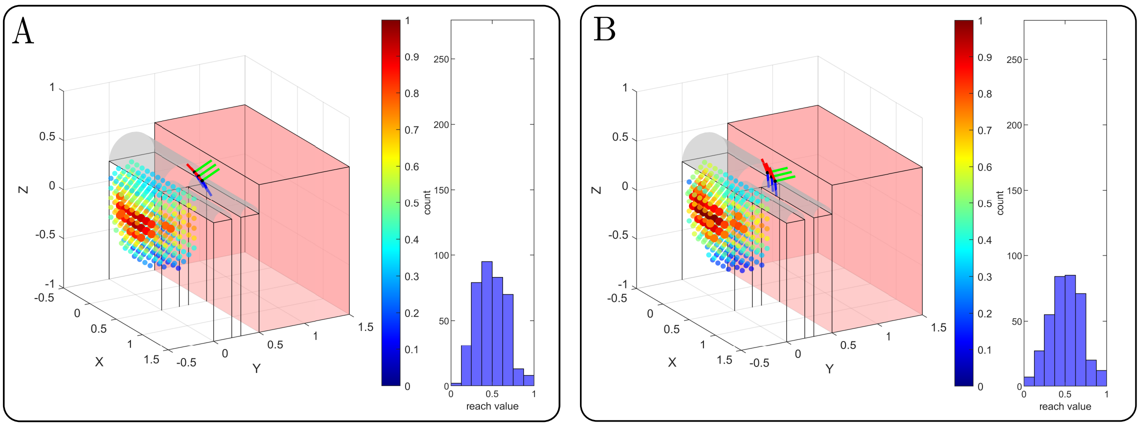

Figure 3.16: Visualization of upright base positions for the *vessel path* for scenario 2. **A** shows the base positions when no adapted tool geometry is applied. In **B**, the distribution of base positions for the optimized tool geometry, resulting in the maximum number of base positions with a reachability value $d_{\mathrm{i,cor}}$>0.75, is shown.

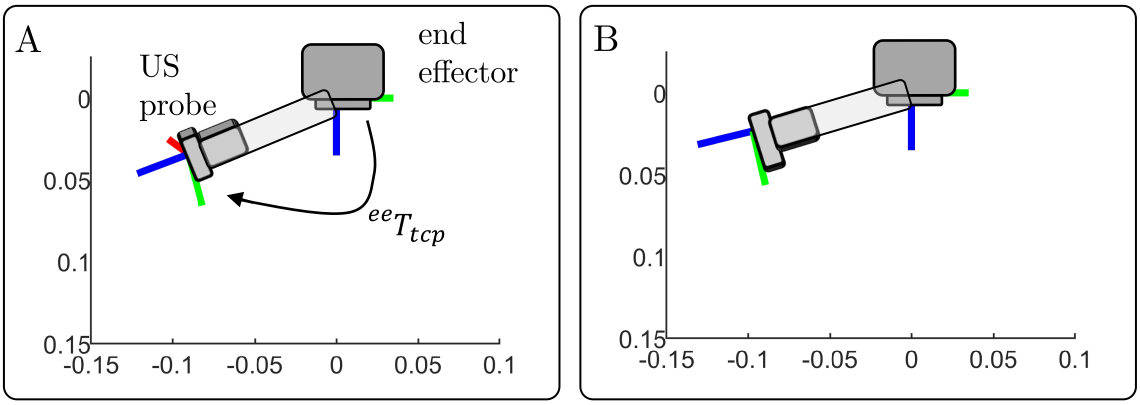

Figure 3.17: Visualization of resulting tool geometries ${}^{\mathrm{tcp}}\mathbf{T}_{\mathrm{ee,max}}$ in scenario 2 for *target pose 1* (**A**) and *target pose 2* (**B**). For *target pose 1* the rotation angle is 76.2° with an axis of $(0.93, 0, -0.37)^T$. For *target pose 2* the rotation angle is 78.1° with an axis of $(0.98, -0.11, 0.19)^T$.

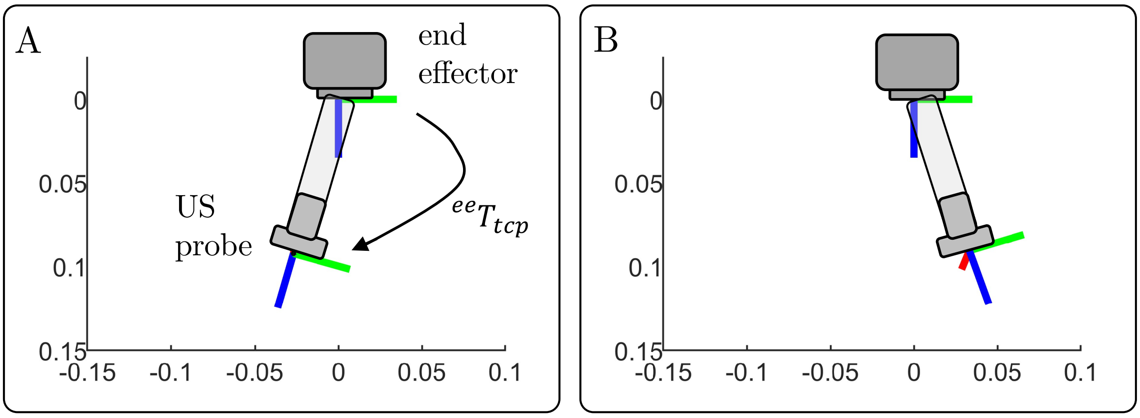

Figure 3.18: Visualization of resulting tool geometries ${}^{\mathrm{tcp}}\mathbf{T}_{\mathrm{ee,max}}$ in scenario 2 for *target pose 3* (**A**) and the *vessel path* (**B**). For *target pose 3* the rotation angle is 22.6° with an axis of $(0.70, 0.71, 0)^T$. For the *vessel path* the rotation angle of the adapted tool is 26.7° with an axis of $(-0.67, -0.63, -0.39)^T$.

3.6 Discussion

3.6.1 Evaluation of Study Results

The evaluation of the results shows that an adapted tool geometry can strongly increase the reachability of the US probe. The extent of increase varies considerably depending on the target pose and the environment. It must be noted that the percentages of improvement shown depend on the specific scenarios and the reachability threshold chosen for the base position count. Therefore, they are not generally applicable. Considering the individual targets *target pose 1*, *target pose 2*, and *target pose 3*, which represent different generic transducer orientations, which are arranged around one side of the patient, the greatest improvements were achieved for *target pose 1*. For scenario 1, the number of possible base poses with reachability higher than 0.75 could be increased by around 52 %. However, the greatest overall improvements in scenario 1 were achieved for the *vessel path*, where a path with a length of 0.2 m, represented by 3 poses, was evaluated. The number of possible base poses with reachability higher than 0.75 could be increased by 232 %. It can be seen that the poses of the *vessel path* are slightly tilted towards the base of the robot, assuming that it is located on the right side next to the patient (when looking at the patient, as shown in Figure 3.10). Due to the end effector inclination required to reach the *vessel path* from this side, the respective reachability of potential robot base positions is reduced. The adapted tool geometry compensates for the end effector inclination, allowing the end effector to be aligned straight down (see Figure 3.10B). This greatly increases the number of possible base placements with high reachability on the right side next to the patient. This effect was observed even more strongly in scenario 2, considering *target pose 1* and *target pose 2*. As it was not permitted to position the robot on one side of the patient, the probe had to be moved over the patient and tilted sharply. This meant that *target pose 1* and *target pose 2* could not be reached at all with the reference tool geometry. With an adapted tool geometry, however, it was possible to reach them.

For *target pose 3* and the *vessel path*, the distributions of base positions resulting from the reference and optimized tool look similar for the respective pose (Figure 3.16 and Figure 3.15). This matches the corresponding optimized tool geometries (Figure 3.12), which are characterized by only a slight mounting angle. Nevertheless, improvements in the number of possible base placements with a reachability value $d_{\mathrm{i,cor}}>0.75$ were 31 % and 52 %, respectively. This shows that even a small, not necessarily intuitive adjustment of the probe geometry could greatly improve the reachability of the target poses and facilitate optimal base placement. It should be noted that the results presented in Table 3.1 and Table 3.2 depend on the threshold value used for the base position count. Choosing another threshold would lead to a different percentage of improvement. However, it can be concluded that the desired inclination angle of the US probe strongly influences the possibility of improvement through a corresponding tool geometry. The more the end effector has to be tilted, the greater the potential to increase the reachability by selecting an adapted tool transformation. The reason for this is that it increases the workspace in which strongly inclined TCP target poses (i.e. pointing towards the robot base) can be reached. This means that poses can be approached for which the robot would otherwise have to be stretched out too far to reach them, as shown for *target pose 1* and *target pose 2* in scenario 2. In addition, once certain poses can be achieved, the limits of all joints except the fourth can restrict the possible rotation of the elbow, resulting in a lower reachability score. In general, the joint limits of joint 2 and joint 6 are most likely to be reached, as these are at ± 120°. In particular, if the end effector is pointing downwards and towards the base, as shown in Scenario 2, the sixth joint must be strongly bent to reach the target pose. As a result, the elbow may no longer be fully rotated as the sixth joint's limit is exceeded. If an appropriate tool transformation is used here, the sixth joint position is further away from its limit, and allows for more elbow rotation.

However, in addition to the promising results, it must also be said that the presented approach can only be applied if the orientations of the defined target area differ only slightly. This is due to the fact that different target orientations lead to different rotation matrices $\mathbf{R}_{\mathrm{j,ee}}$ (see Eq. 3.10). It follows that the resulting rotation matrices $\mathbf{R}_{\mathrm{i,j,tool}}$ of the tool geometries depend not only on the base rotations $\widetilde{\mathbf{R}}_{\mathrm{i,j,ee}}$ to ensure an upright base, but also on $\mathbf{R}_{\mathrm{j,ee}}$. This means that $\mathbf{R}_{\mathrm{i,j,tool}}$ can no longer be clustered according to the uprighting base rotations, which is the prerequisite for compensating for these base rotations by means of corresponding tool transformations. However, this does not affect the application. If the optimum tool geometry has to be calculated for a target area with different orientations, the mean value of the orientations can be calculated first. This orientation then represents the target orientation under consideration.

3.6.2 Practical Considerations

The results have shown that the optimal design of the tool geometry depends on the target pose and environment. This is a challenge in practice, as it is not possible to dynamically adjust the tool geometry during an intervention. Ideally, you would have a one-size-fits-all solution in practice. For example, a probe can be used that is attached to the end effector at an angle of 45°. This geometry represents a compromise: Even though a pure extension provides the greatest possible general flexibility in the end effector orientations that can be achieved, the angulation increases the range of the US probe, and target poses on the patient with a large angle of inclination (e.g. *target pose 1*, Scenario 2) can be reached more easily. Moreover, the guidance of the cable of the US probe is simplified. However, during various volunteer studies in which robotized US scans were carried out, it was found that this one-size-fits-all solution can be unfavorable depending on the area to be reached on the patient and resulted in some volunteers having to be repositioned. An adapted probe holder geometry for US robots that always perform the same procedure (e.g. scan of the leg artery) could therefore be feasible and useful. Alternatively, a mechanism could be considered whereby the angle of attachment can be changed manually depending on the application, e.g. using a screw that can be tightened and loosened by hand. This would allow the tool geometry to be adjusted before the respective examination. Another, more automated option would be to integrate an automatic mechanism for switching between different tool geometries.

Similar concepts have been explored in microsurgery, where automatic tool changers allow the robotic system to autonomously switch between surgical instruments during procedures [58]. Transferring this approach to robotic US systems would allow the probe holder geometry to be flexibly adapted to the scanned body region during the examination.

3.7 Conclusion

Before an automatic robotic ultrasound scan can be performed, the robot and patient must be positioned correctly in relation to each other during the pre-scanning phase. This ensures that the target region is reached safely. This chapter investigated how different probe holder geometries influence the placement of an upright robot base concerning reachability of the target poses. A redundant seven DoF serial manipulator was used to perform an US scan of three different generic target poses on the torso as well as a specific path of the leg artery on a patient. First, reachability maps as well as inverse reachability maps were generated. These were used to determine potential placements for an upright robot base, while a respective tool transformation was applied and constraints such as patient safety and an additional restricted area were taken into account. It could be demonstrated that the number of potential base placements with high reachability can be greatly increased by using an appropriate tool transformation, especially if the sixth joint of the robot has to function close to the joint's limit to reach the target position. This was particularly the case when the target pose had to be reached from the other side of the patient. The proposed method offers an automated solution for finding such an adaptation of the tool transformation. It is useful when high reachability is required at the target area, or when the robot's placement area is limited.

4

AUTOMATIC ROBOTIC DOPPLER SONOGRAPHY OF LEG ARTERIES[2]

Once the robot has been positioned appropriately, the scanning phase of the examination can be initiated. This involves a robotic US scan of a patient's femoral artery. For a successful scan, the robotic system must fulfill certain core functions (Figure 4.1). The robot must guide the US probe along the patient's leg using a defined contact force while centering the vessel to acquire high-quality images.

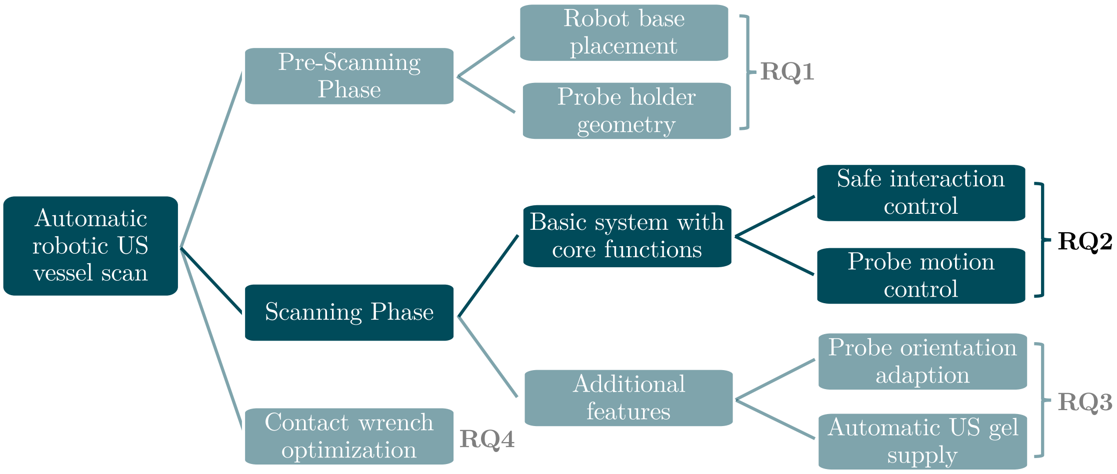

Figure 4.1: Structure of the thesis. The essential topics required for an automatic robotic US examination are addressed in individual chapters, with the content of this chapter highlighted in dark blue.

These functions represent the minimum requirements for a successful examination and are developed in this chapter by addressing **RQ2**:

> **Research Question 2**
> How can the essential core functions of the robotic system be realised to enable a straightforward automatic US examination of the femoral artery?

The required steps for system calibration, the implementation of compliant control, and the dynamic tracking of the artery's position in the US images are explained

---

[2] Parts of this chapter have been published in [59].

below. Finally, a volunteer study is presented in which the femoral artery is scanned by the robotic system, validating its core functionality in a practical setting.

4.1 Related Work - Robotic US Systems for Vascular Examinations

In recent years, many robotic systems have been developed to perform automated ultrasound scanning procedures. A comprehensive overview of robotic ultrasound systems is given in [60]–[64]. Furthermore, recent advances in machine learning and deep learning technologies to improve the intelligence and autonomy of robotic ultrasound systems are summarized by [65]. Selected robotic systems that have been specially developed for scanning vascular structures are presented in the following.

In [66], a robotic arm was used to scan the lower limb artery. The vessel lumen was segmented from the B-mode image using a fast-marching method, and the position of the probe was adjusted accordingly to keep the artery continuously in the center of the image. Haxthausen et al. also presented an approach in which a robot successfully followed the peripheral artery of a phantom automatically. The vessel center was determined either using a neural network [67] or a template-matching method [68]. This approach was further expanded into an assistance system for performing robot-assisted, ultrasound-guided endovascular stent implantation [69]. Using a phantom study, it was shown that the integration of vascular stents is possible with the aid of an US robot and that the use of X-rays can therefore be avoided. Furthermore, a fully robotic system for detecting tubular structures was developed [70], which was based on a neural network for vessel segmentation. In addition, the US probe was automatically aligned with the normal direction of the target structure, while the vessel structure was held in the center of the US view. However, all the robotic US systems described above were only evaluated based on phantom experiments. To ensure suitability for use in clinical practice, volunteer studies are necessary. In [71], an imitation learning approach based on clinical protocols was presented to automatically scan the carotid artery. Moreover, [72] presents an automated robotic carotid artery scanning system, where a yolov5 framework model [73] was used to learn the features of the carotid artery and train a recognition model by using manually labeled data. To verify the effectiveness of the proposed automated scanning systems, volunteer studies were performed. Further recent developments of ultrasound robots, with the aim of scanning the carotis, are presented in [74] and [75]. Experiments on human subjects showed the systems' feasibility in a realistic scenario. A semi-autonomous robotic examination system to diagnose deep vein thromboses is proposed in [76]. Virtual fixtures are used to allow the examiner to either move the probe along a scan path or to perform a compression-release test with minimal effort while the contact force is controlled by the robot. Furthermore, a fully autonomous robotic ultrasound system, which is able to scan thyroid regions and identify nodules, is presented in [77]. A recently published system for fully automated, robot-assisted 3D ultrasound image acquisition of arteries is presented in [78]. A neural network with a u-net structure was used to determine the vessel center, while the in-plane rotation of the probe was corrected by an US confidence

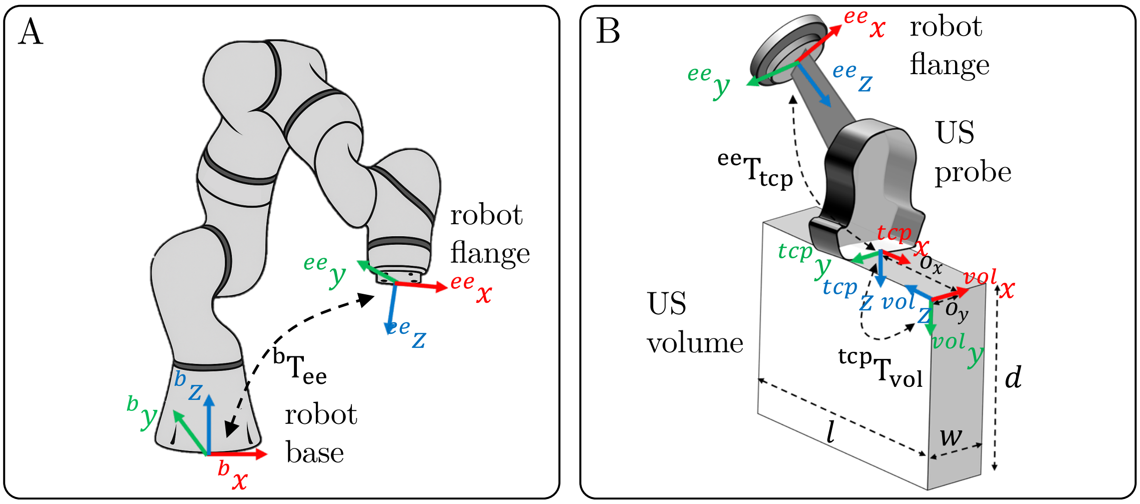

Figure 4.2: **A:** Visualization of the base and flange frames of the robot as well as the respective transformation ${}^{\mathrm{b}}\mathbf{T}_{\mathrm{ee}}$. The image of the robot was generated by ChatGPT [6]. **B:** Geometric representation of the transformation from the robot's flange to the probe's tip ${}^{\mathrm{ee}}\mathbf{T}_{\mathrm{tcp}}$ as well as the transformation from the probe's tip to the US volume ${}^{\mathrm{tcp}}\mathbf{T}_{\mathrm{vol}}$.

map.

There are only a few studies where Doppler US is used for robot-guided examinations. In [79], a robotic system to enable autonomous vascular access is presented. Duplex US is used there to predict segmentations of veins and arteries by a neural network to compensate for vessel motion, while the needle is guided into the target vessel. For diagnostic robotic US scanning, [80] demonstrates an approach where Doppler US is used to improve the accuracy and robustness of vessel segmentation. A study was performed where arm vessels of volunteers were scanned. There is thus a lack of robotic systems that perform automated acquisition of diagnostic duplex US scans of vessels. This would be particularly useful for the automated diagnosis and follow-up care of vascular pathologies, as duplex sonography has become the preferred diagnostic tool [2].

4.2 System Calibration

To control the position of the robot based on an US volume or a sectional plane of this volume, the transformation matrix ${}^{\mathrm{b}}\mathbf{T}_{\mathrm{vol}}$ must be determined. This matrix transforms pixel positions from an US volume {vol} into the base frame {b} of the robot. The frames involved in this process are shown in Figure 4.2. Consequently, the calculation of ${}^{\mathrm{b}}\mathbf{T}_{\mathrm{vol}}$ can be performed as follows:

$${}^{\mathrm{b}}\mathbf{T}_{\mathrm{vol}} = {}^{\mathrm{b}}\mathbf{T}_{\mathrm{ee}}\ {}^{\mathrm{ee}}\mathbf{T}_{\mathrm{tcp}}\ {}^{\mathrm{tcp}}\mathbf{T}_{\mathrm{vol}} \tag{4.1}$$

where ${}^{\mathrm{j}}\mathbf{T}_{\mathrm{i}} \in \mathbb{R}^{4\times4}$ is the homogeneous transformation matrix to transfer the pose from frame {i} to frame {j}. The probe tip's frame is centered on the US probe and referred to as {p}. The frame of the robot flange is denoted as {f}. The transformation ${}^{\mathrm{b}}\mathbf{T}_{\mathrm{ee}}$ can be derived from the measured joint angles and the forward kinematics of the robot. The transformation ${}^{\mathrm{ee}}\mathbf{T}_{\mathrm{tcp}}$ can be inferred from the CAD model of the probe holder and the probe attached to it. To determine the transformation ${}^{\mathrm{tcp}}\mathbf{T}_{\mathrm{vol}}$, a spatial calibration can be performed. This is done either by using customized phantoms [81]–[83] or by employing image-based methods [84]. The resulting transformation ${}^{\mathrm{tcp}}\mathbf{T}_{\mathrm{vol}}$ contains the homogeneous rigid transformation ${}^{\mathrm{tcp}}\mathbf{T}_{\mathrm{vol,rgd}}$ from the probe tip's frame to the image frame as well as the image spacing represented as an affine transformation $\mathbf{S} \in \mathbb{R}^{4\times 4}$ with spacing factors s_x, s_y, and s_z for the respective axes:

$$ {}^{\mathrm{tcp}}\mathbf{T}_{\mathrm{vol}} = \underbrace{\begin{pmatrix} & \mathbf{R} & & o_x \\ & & & o_y \\ & & & o_z \\ 0 & 0 & 0 & 1 \end{pmatrix}}_{{}^{\mathrm{tcp}}\mathbf{T}_{\mathrm{vol,rgd}}} \underbrace{\begin{pmatrix} s_x & 0 & 0 & 0 \\ 0 & s_y & 0 & 0 \\ 0 & 0 & s_z & 0 \\ 0 & 0 & 0 & 1 \end{pmatrix}}_{\mathbf{S}} . \tag{4.2} $$

The transformation ${}^{\mathrm{tcp}}\mathbf{T}_{\mathrm{vol,rgd}}$ consists of a rotation matrix $\mathbf{R}$ describing the geometric relationship between the orientation of the probe tip's frame $\{\mathrm{p}\}$ and the orientation of the US volume frame $\{\mathrm{vol}\}$ as well as a translational offset $\mathbf{o} = (o_x, o_y, o_z)^{\mathrm{T}}$ between the origins of the frames (see Figure 4.2B). However, precise spatial calibration is an error-prone, time-consuming step. In addition, precise spatial calibration is not always required. For example, methods for 3D volume reconstruction are also possible without perfect spatial calibration, either by directly merging 3D US volume data by volume-to-volume registration methods [85], or by using inertial measurement units to track the probe's orientation [86]. Furthermore, diagnostic applications such as the one shown in this study can be performed without precise spatial calibration. For this reason, a simplified option by determining an approximate transformation matrix ${}^{\mathrm{tcp}}\mathbf{T}_{\mathrm{vol,smp}}$ was used, which considerably simplifies the workflow and improves usability. The aim of robotic US scans based on visual servoing is to move the probe depending on the US volume or image. Instead of a movement to a specific position, it is often sufficient to move the probe in a certain direction, e.g. in the direction of the vessel to be tracked. Thus, the essential parameter is the rotation matrix $\mathbf{R}$ between the orientation of the probe tip's frame $\{\mathrm{p}\}$ and the US volume frame $\{\mathrm{vol}\}$. This can be determined experimentally by positioning the probe attached to the robot flange in such a way that the cross-section of the artery (or any other easy trackable structure) is visible in the ${}^{vol}xy$-plane of the US volume. Its initial position is determined by manually selecting the cross-section from the US image. The probe is then moved transversely for a small distance in the positive ${}^{tcp}y$-direction of the probe tip's frame. The displacement of the vessel in the ${}^{vol}xy$-plane can either be recognized manually by the operator or can be tracked by a template matching algorithm described in Section 4.4.1. Finally, the difference between the ${}^{vol}x$-values of the start and end position of the vessel is calculated. If the difference is positive, the ${}^{vol}x$-axis and the ${}^{tcp}y$-axis point in the opposite direction, resulting in the rotation matrix $\mathbf{R}_1 = (0,0,-1;-1,0,0;0,1,0)^{\mathrm{T}}$. Correspondingly, if the difference is negative, the ${}^{vol}x$-axis and the ${}^{tcp}y$-axis point in the same direction, resulting in the rotation matrix $\mathbf{R}_2 = (0,0,1;1,0,0;0,1,0)^{\mathrm{T}}$. The offset values $(o_x, o_y, o_z)^{\mathrm{T}}$ of the calibration matrix ${}^{\mathrm{tcp}}\mathbf{T}_{\mathrm{vol,smp}}$ can be derived geometrically as the interface of the US station provides us with the size of the US volume (length l, width w, depth d, see Figure 4.2B) in pixels as well as the corresponding image spacing s_x, s_y, and s_z. This allows us to calculate the offsets o_x and o_y between the probe and volume frames, assuming that the volume is located in the center under the probe:

$$o_x = \frac{l}{2}\, s_x \tag{4.3}$$

$$o_y = \frac{w}{2}\, s_y \tag{4.4}$$

$$o_z = 0. \tag{4.5}$$

The offset o_z is neglected since it is only a minimum distance in ${}^{tcp}z$-direction between the origin of the probe frame and the US volume frame, as defined by the arrangement of the transducer elements in the probe. This results in the following transformation matrix for the case $\mathbf{R} = \mathbf{R}_1$ as shown in Figure 4.2, B:

$$^{\text{tcp}}\mathbf{T}_{\text{vol,smp}} = \begin{pmatrix} 0 & 0 & -s_z & \frac{l}{2}s_x \\ -s_x & 0 & 0 & \frac{w}{2}s_y \\ 0 & s_y & 0 & 0 \\ 0 & 0 & 0 & 1 \end{pmatrix}. \tag{4.6}$$

The described approximate calibration method offers the advantage of requiring no additional time for spatial calibration with a phantom, as long as the probe remains attached to the end effector in the same position. All necessary values for Eq. (4.6) are obtained from the ultrasound station's interface, allowing for complete automation of the process.

4.3 Robot Control

To enable a successful examination, high-quality US images are essential while the robot guides the probe along the femoral artery in the patient's leg. For this purpose, an interaction control scheme based on the internal joint and torque sensors is employed that is adapted to the application of an US scan on a patient. The following requirements must be met, with the robotic US system designed to minimize complexity by avoiding the use of external sensors or electronics:

1. **Safe interaction control:** The robot behaves compliantly, while a defined contact force is applied with the probe. Moreover, robustness against measurement errors resulting from the robot's wrench estimation model is ensured.
2. **Probe motion control:** A specific movement of the probe is executed as commanded, guided by visual servoing inputs based on US image feedback.

4.3.1 Safe Interaction Control

To ensure the patient's safety and comfort, it must be possible to push the robot's links away at any time. This applies both to the probe attached to the end effector and to any robot links (e.g. the robot's elbow). As a result, a joint admittance control scheme is applied and defined as

$$\dot{\mathbf{q}}_{\text{ic}} = \left(\boldsymbol{\tau}_{\text{d}} + \boldsymbol{\tau}_{\text{ext}}\right)\mathbf{D}^{-1}, \tag{4.7}$$

where $\boldsymbol{\tau}_\mathrm{d}$ represents the desired and $\boldsymbol{\tau}_\mathrm{ext}$ the measured external joint torques, obtained from the robot's control interface. $\mathbf{D} \in \mathbb{R}^{7\times7}$ is a diagonal damping matrix, with damping factors d_i representing the diagonal entries. The resulting joint velocities are denoted as $\dot{\mathbf{q}}_c$. If no desired torques are applied, $\boldsymbol{\tau}_\mathrm{d} = 0$ and the robot reacts completely compliant. It therefore only compensates for its own weight and can be moved freely in space. Now, a defined contract force $\mathbf{f}_\mathrm{d}$ is applied in the direction of the probe's $z-$axis. Thus, the desired wrench is defined as $\mathbf{w}_\mathrm{d} = (0, 0, f_{\mathrm{z,d}}, 0, 0, 0)^\mathrm{T}$. Using the transposed Jacobian matrix $\mathbf{J}(\mathbf{q})^\mathrm{T} \in \mathbb{R}^{7\times6}$ for the measured joint positions $\mathbf{q}$, the desired joint torques corresponding to the defined wrench are calculated by

$$\boldsymbol{\tau}_\mathrm{d} = \mathbf{J}(\mathbf{q})^\mathrm{T}\mathbf{w}_\mathrm{d}. \tag{4.8}$$

Substituting $\boldsymbol{\tau}_\mathrm{d}$ in Eq. (4.7) by Eq. (4.8) leads to

$$\dot{\mathbf{q}}_\mathrm{ic} = \Big(\mathbf{J}(\mathbf{q})^\mathrm{T}\mathbf{w}_\mathrm{d} + \boldsymbol{\tau}_\mathrm{ext}\Big)\mathbf{D}^{-1}, \tag{4.9}$$

representing the resulting joint velocities that enable a desired probe contact force at the current position. It can be seen that there is no Cartesian force feedback used to control the contact force. This could be integrated by adding a PI-Controller with gains k_p and k_i to Eq. (4.8), resulting in an adaption of Eq. (4.9)

$$\dot{\mathbf{q}}_\mathrm{ic,fb} = \Big(\mathbf{J}(\mathbf{q})^\mathrm{T}\Big(\mathbf{w}_\mathrm{d} + k_\mathrm{p}\mathbf{w}_\mathrm{e} + k_\mathrm{i}\int \mathbf{w}_\mathrm{e}(t)\,dt\Big) + \boldsymbol{\tau}_\mathrm{ext}\Big)\mathbf{D}^{-1}, \tag{4.10}$$

whereby steady-state wrench errors $\mathbf{w}_\mathrm{e} = \mathbf{w}_\mathrm{d} - \mathbf{w}_\mathrm{ext}$ could be eliminated. The measured external wrench is defined by $\mathbf{w}_\mathrm{ext} = (0, 0, f_{\mathrm{z,ext}}, 0, 0, 0)^\mathrm{T}$ and a precise measurement is therefore essential to reduce the error between the desired and actual measured force. However, as no external force/torque sensor is used, the wrench measurement is calculated based on the general robot dynamics equation (Eq. (2.8) in Section 2.3.2). Thus, it depends on the current joint configuration of the robot and the accuracy of the estimation of the external joint torques based on the manufacturer's model. In positions close to singularities, outliers with large errors can therefore occur for $\mathbf{w}_\mathrm{ext}$. These errors could have drastic consequences, such as instability of the control or the application of falsely excessive contact forces, which could result in injury to the patient. Therefore, when employing Cartesian force feedback without an external force/torque sensor, it is crucial to ensure an optimized wrench estimation model that enables precise measurements and minimizes the occurrence of large outliers. A suitable method for this purpose is proposed in Chapter 6.

4.3.2 Probe Motion Control

The proposed interaction controller so far aims to apply a desired force $\mathbf{f}_\mathrm{d}$ in the direction of the probe's $z-$axis (one DoF). However, to enable autonomous US examinations, it is necessary to simultaneously adjust the probe's pose. First, the probe's orientation must be aligned appropriately to be placed flat on the skin. Additionally, the probe's position must be adjusted to move the probe along the leg, to always keep the vessel fully visible in the US image. To achieve this, a translational motion $\mathbf{v}_\mathrm{d} = (\dot{x}, \dot{y}, 0)^\mathrm{T}$ in the probe frame's $x-$ and $y-$axes (two DoF) as well as a rotational motion $\mathbf{w}_\mathrm{d} = (\dot{\phi}, \dot{\theta}, \dot{\psi})^\mathrm{T}$ around the $x-$, $y-$ and $z-$axes (three DoF) are defined. The joint velocities required to achieve the resulting desired twist $\boldsymbol{\nu}_\mathrm{d} = (\mathbf{v}_\mathrm{d}, \mathbf{w}_\mathrm{d})^\mathrm{T}$ are calculated using the Jacobian pseudo-inverse method [87]:

$$\dot{\mathbf{q}}_\mathrm{mc} = \mathbf{J}^\dagger \boldsymbol{\nu}_\mathrm{d}. \tag{4.11}$$

A precise motion can directly be computed, without the need for explicit inverse kinematics calculations or complex path planning. However, when the Jacobian matrix approaches singularities, the pseudoinverse amplifies small errors, causing joint velocities to spike and destabilize the system. To counteract this issue, the resulting joint velocities are limited to remain within safe and feasible ranges during motion. A more comprehensive solution is achieved by the damped least squares method, regularizing the pseudo-inversion calculation, which stabilizes the system even in the presence of singular configurations. The damped least squares method reduces the amplification of small errors by modifying the standard pseudoinverse formula with a damping term:

$$\dot{\mathbf{q}}_\mathrm{mc,dls} = \mathbf{J}^\mathrm{T} \left(\mathbf{J}\mathbf{J}^\mathrm{T} + \lambda^2 I \right)^{-1} \boldsymbol{\nu}_\mathrm{d}. \tag{4.12}$$

The damping constant λ must be chosen to stabilize the pseudo-inversion calculation by regulating small eigenvalues while remaining small enough to minimize deviations from the exact solution and maintain accuracy in well-conditioned configurations. In order to fulfil this compromise as well as possible, different approaches are provided, e.g. in [88], allowing for dynamic adaption of the damping constant.

4.3.3 Control Implementation for Volunteer Study

To conduct the volunteer study, safe interaction control without Cartesian force feedback and motion control were combined, by adding Eq. (4.11) to Eq. (4.9):

$$\dot{\mathbf{q}}_\mathrm{c} = \left(\mathbf{J}(\mathbf{q})^\mathrm{T} \mathbf{w}_\mathrm{d} + \boldsymbol{\tau}_\mathrm{ext} \right) \mathbf{D}^{-1} + \mathbf{J}^\dagger \boldsymbol{\nu}_\mathrm{d}. \tag{4.13}$$

A contact force of 5 N was applied, thus the desired wrench was set to $\mathbf{w}_\mathrm{d} = (0, 0, 5, 0, 0, 0)^\mathrm{T}$. The damping factors d_i representing the diagonal entries of the damping matrix $\mathbf{D}$ were experimentally determined and set to 5 Nms. For motion control, the pseudo-inverse method was preferred to the damped least squares method, as a more precise positioning of the probe for performing the scan was considered to outweigh the advantages of an increased numerical stability when calculating the pseudoinverse of the Jacobian. However, to ensure the safety of the control system, the calculated joint velocities $\dot{\mathbf{q}}_c$ were severely limited to 10% of the maximum possible values $\dot{\mathbf{q}}_\mathrm{max} = (9.8, 9.8, 10.0, 13.0, 14.0, 18.0, 18.0)^\mathrm{T} \frac{^\circ}{\mathrm{s}}$ of the robot. In this way, abrupt probe movements resulting from a poorly conditioned pseudoinverse Jacobian can be prevented.

The joint velocities $\dot{\mathbf{q}}_c$ are transformed into discrete joint positions $\mathbf{q}_\mathrm{c}$ for a time step t through numerical integration over the cycle time Δt by using

$$\mathbf{q}_\mathrm{c}(t + \Delta t) = \mathbf{q}_\mathrm{c}(t) + \dot{\mathbf{q}}_\mathrm{c} \Delta t. \tag{4.14}$$

The resulting joint positions $\mathbf{q}_\mathrm{c}$ are used in the target values for the robot's joint impedance controller to further increase stability during contact with the environment. The joint impedance controller was parameterized with a stiffness of 500 $\frac{\mathrm{Nm}}{\mathrm{rad}}$ and a damping ratio of 0.9.

Probe position adaption

The translational movement $\mathbf{v}_\mathrm{d} = (\dot{x}, \dot{y}, 0)^\mathrm{T}$ of the twist $\boldsymbol{\nu}_\mathrm{d}$ in Eq. (4.13) was defined to fulfill two objectives: Firstly, the probe must be guided forward along the leg, starting from the area beneath the hip and moving toward the popliteal fossa. On the other hand, a corrective movement transverse to the forward movement is required to adjust the probe's position and keep the vessel centered in the US image. The transverse correction movement must be performed when the distance e_c (see Figure 4.4) between the center of the US image and the center of the vessel exceeds 50 px to prevent the vessel from moving out of the image. Otherwise, if $e_c < 50$ px, the probe must be moved forward. The velocity at which the probe is moved in both cases is set at $c_\mathrm{trans} = 0.01\frac{\mathrm{m}}{\mathrm{s}}$, which is roughly equivalent to a manual scan by a physician. For the arrangement of the probe shown in Figure 4.2B, where the probe's ${}^\mathrm{tcp}x-$axis indicates the longitudinal direction of the vessel scan, this leads to:

$$\mathbf{v}_\mathrm{d} = \begin{cases} (0, \mathrm{sgn}(e_\mathrm{c}) \cdot c_\mathrm{trans}, 0)^\mathrm{T}, & \text{if } |e_\mathrm{c}| > 50\,\mathrm{px}, \\ (c_\mathrm{trans}, 0, 0)^\mathrm{T}, & \text{if } |e_\mathrm{c}| < 50\,\mathrm{px}. \end{cases} \tag{4.15}$$

In order to calculate the difference e_c between the center of the US image and the vessel, it is necessary to detect the vessel, which is explained in Section 4.4.

Probe orientation adaption

While scanning, the probe must be orientated accordingly to enable full probe contact with the body. Therefore, a desired probe orientation $\mathbf{R}_\mathrm{d}$ must be achieved, which can be specified depending on the task requirements. To align the probe according to the desired orientation, the error to the probe's currently measured orientation $\mathbf{R}_\mathrm{err}$ is calculated by the relative rotation matrix $\mathbf{R}_\mathrm{err}$, which describes the transformation from $\mathbf{R}_\mathrm{c}$ to $\mathbf{R}_d$ with respect to the probe's frame:

$$\mathbf{R}_\mathrm{err} = \mathbf{R}_\mathrm{c}^{-1} \cdot \mathbf{R}_\mathrm{d}. \tag{4.16}$$

The rotation angle β between $\mathbf{R}_c$ and $\mathbf{R}_d$ is calculated using the trace of the rotation matrix

$$\beta = \arccos\left(\frac{\mathrm{tr}(\mathbf{R}_\mathrm{err}) - 1}{2}\right), \tag{4.17}$$

where the trace is given by the sum of the diagonal elements:

$$\mathrm{tr}(\mathbf{R}_\mathrm{err}) = \mathbf{R}_{\mathrm{err},11} + \mathbf{R}_{\mathrm{err},22} + \mathbf{R}_{\mathrm{err},33}. \tag{4.18}$$

The rotation axis $\mathbf{a}$ is computed using the off-diagonal elements of the matrix $\mathbf{R}_\mathrm{err}$:

$$\mathbf{a} = \frac{1}{2\sin(\theta)} \begin{pmatrix} \mathbf{R}_{\mathrm{err},32} - \mathbf{R}_{\mathrm{err},23} \\ \mathbf{R}_{\mathrm{err},13} - \mathbf{R}_{\mathrm{err},31} \\ \mathbf{R}_{\mathrm{err},21} - \mathbf{R}_{\mathrm{err},12} \end{pmatrix}. \tag{4.19}$$

Finally, the twist's rotation vector $\mathbf{w}_\mathrm{d}$ is calculated, which represents a rotational movement of the probe in the direction of the desired orientation $\mathbf{R}_\mathrm{d}$:

$$\mathbf{w}_\mathrm{d} = \begin{cases} \mathbf{0}, & \text{if } \|\mathbf{a}\| = 0, \\ \beta \cdot \frac{\mathbf{a}}{\|\mathbf{a}\|}, & \text{else.} \end{cases} \tag{4.20}$$

To prevent the probe from rotating too quickly, the rotation speed is limited to a value of $c_\mathrm{rot,max} = 10\ \frac{^\circ}{\mathrm{s}}$.

In the study presented in this chapter, the probe is placed and correctly aligned by a physician before the automatic scanning procedure starts. Due to the relatively slight curvature and the elasticity of the upper leg, the initial alignment of the probe can be maintained while moving along the vessel. Thus, the initial orientation of the probe therefore represents the desired orientation $\mathbf{R}_\mathrm{d}$ during the scan. However, if there is a greater curvature of the structure being examined, the probe orientation must be automatically adjusted while being moved. This would be relevant, for example, in a scanning scenario of the rib cage, which has a greater curvature and also higher rigidity. Due to the lower compliance of the body surface, the probe will lose contact more quickly if it is not optimally aligned according to the curvature. To address this challenge, an advanced method for automatically adjusting the probe's orientation to align with the approximate surface normal is presented in Section 5.1 of Chapter 5.

4.4 Image Analysis

A two-step approach is used for artery tracking. In the first step, possible vessel positions are determined using image processing. This is done either by searching for the vessel position using template matching (see Section 4.4.1) or by extracting the red-colored blood flow in the US Doppler images (see Section 4.4.2). In the second step, the vessel positions identified are then checked for plausibility with the previous time step (see Section 4.4.3).

4.4.1 Vessel Template Matching

The procedure of the first approach, which uses a template matching algorithm to find the vessel's position, is illustrated in Figure 4.3. This involves the physician or operator of the system selecting the cross-section of the artery at the start position of the scan. This selected image section represents the template that is subsequently matched in the US images captured during the scan. At each (x, y)-position of the image $\mathbf{I}$ the similarity with the template $\mathbf{T}$ is determined by calculating the normalized correlation coefficient:

$$\mathbf{C}_\mathrm{all}(x, y) = \frac{\sum_{x',y'} (\mathbf{T}_{(x',y')} \cdot \mathbf{I}(x + x', y + y'))}{\sqrt{\sum_{x',y'} \mathbf{T}(x', y')^2 \cdot \sum_{x',y'} \mathbf{I}(x + x', y + y')^2}}. \tag{4.21}$$

Thus, the resulting matrix $\mathbf{C}_\mathrm{all}(x, y)$ contains a similarity value with the template for each (x, y) position in the source image. Possible vessel positions are represented

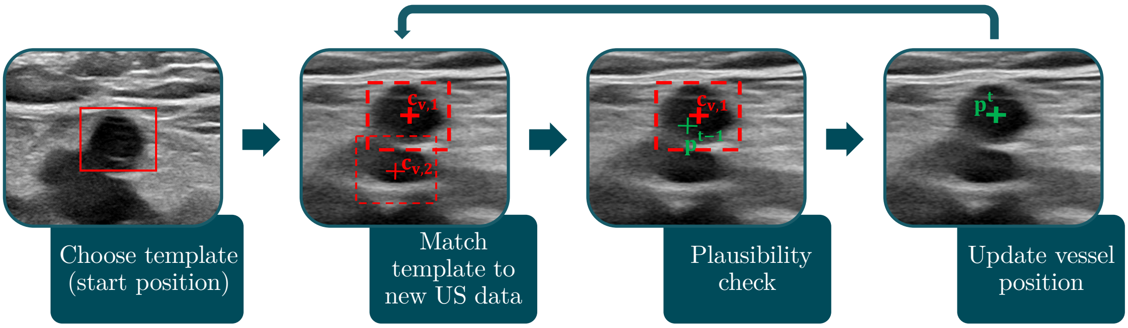

Figure 4.3: Procedure of template matching vessel tracking. The vessel template is selected at the scan's start position. This template is then searched for in the new US images during the scan. The thicker dashed red box indicates the potential position $\mathbf{c}_{\mathrm{v},1}$ with the highest correlation coefficient. This position is then compared with the vessel's position $\mathbf{p}^{\text{t-1}}$ from the previous time step.

by the best matches, which is why the values of $\mathbf{C}_{\mathrm{all}}(x, y)$ are sorted in decreasing order and then referred to as $\mathbf{C}_{\mathrm{v}}$. The second step in Figure 4.3 shows two of these matches as examples, where $\mathbf{c}_{\mathrm{v,i}}$ represents the ith value of the sorted items. Thus, $\mathbf{c}_{\mathrm{v},1}$ is considered to be the best match. It is important to prevent incorrect matches in other image regions, as otherwise the robot may be guided away from the target position. Therefore, potential vessel positions are then checked for plausibility with regard to the position $\mathbf{p}^{\text{t-1}}$ from the previous time step (third step in Figure 4.3) using the tracking algorithm in Section 4.4.3.

4.4.2 Vessel Doppler Signal

The Doppler signal, which is used to visualize blood flow, is of major importance in clinical practice for the diagnosis of vascular diseases, including peripheral arterial disease. Nevertheless, it's rarely found in robotic US interventions. As a 3D probe is used, the X-plane view of the ultrasound station can be used to enable simultaneous visualization of the longitudinal and cross-sections of the vessel (see Figure 4.4B). The procedure to find potential artery positions based on the Doppler images is illustrated in Figure 4.5. The Doppler images showing the cross-section of the artery are first converted into the HSV color space and detected flow areas are determined by filtering all red-colored areas (first step in Figure 4.5). The values of the corresponding HSV ranges are:

$$H_{red} \in [0, 10] \cup [170, 180] \tag{4.22}$$
$$S_{red} \in [50, 255] \tag{4.23}$$
$$V_{red} \in [20, 255]. \tag{4.24}$$

The resulting red areas are sorted according to their size in descending order and referred to as $\mathbf{C}_{\mathrm{all}}$. In the next step, they are grouped into clusters if they are close to each other (see Algorithm 1). For this purpose, the Euclidean distances between the largest area's center and the centroids of the remaining areas are calculated. If the distances are smaller than a threshold $r_{\mathrm{cl}} = 50$ px, which corresponds approximately to the radius of the artery in the settings used, they are combined, and the centroid

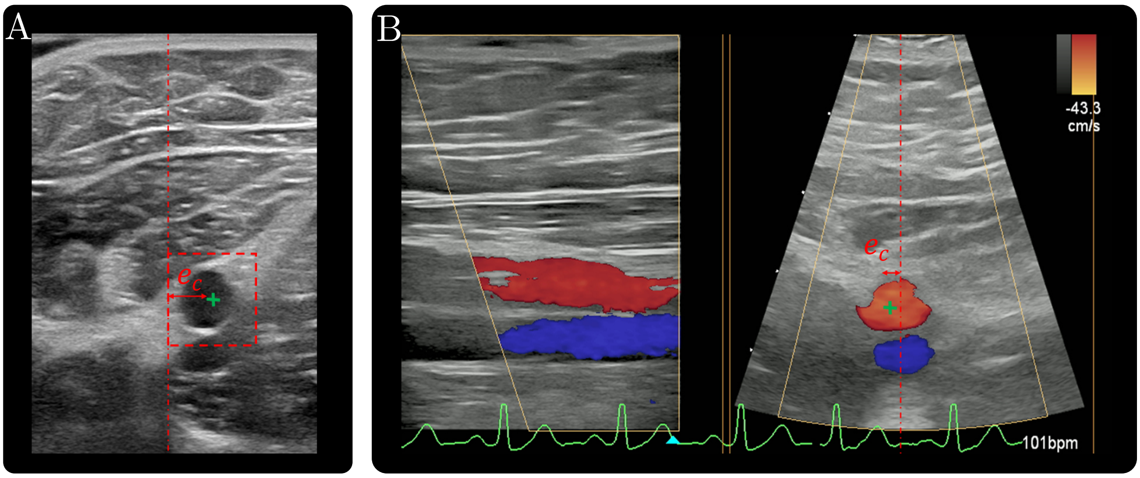

Figure 4.4: **A:** Vessel position determined by template matching. **B:** Determination of the vessel position from the Doppler X-Plane US image.

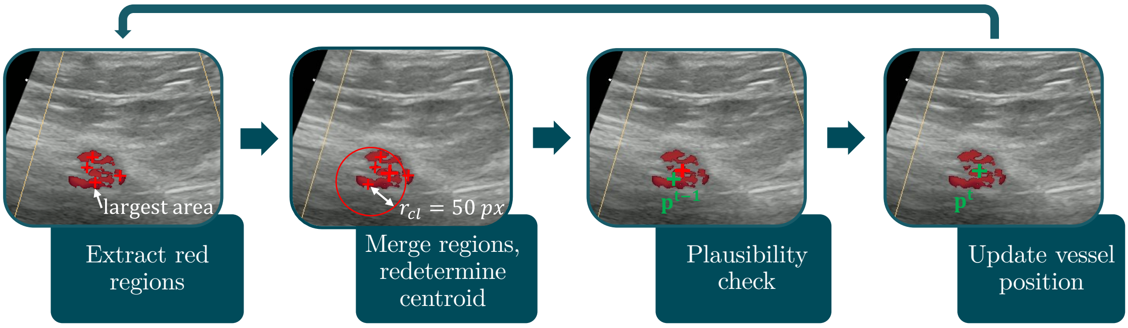

Figure 4.5: Procedure of Doppler vessel tracking. Red regions are extracted and merged into bigger clusters. The centroid of the merged cluster is indicated by the thicker red cross representing the potential vessel position $\mathbf{c}_{\mathrm{v},1}$. The vessel's position is updated following a plausibility check concerning the vessel's position $\mathbf{p}^{\mathrm{t}\text{-}1}$ of the previous time step.

is redetermined (see Figure 4.5, second step). This merging of red areas is done because the increasing or decreasing blood flow caused by the heart contraction can result in many smaller, unconnected colored areas in the Doppler US image (see Figure 4.5). The resulting merged clusters represent potential vessel positions $\mathbf{C}_{\mathrm{v}}$. Here, $\mathbf{c}_{\mathrm{v},1}$ represents the largest red cluster and is therefore regarded as the most likely match for the vessel's position. Finally, $\mathbf{c}_{\mathrm{v},1}$ is checked for plausibility in relation to the vessel's position $\mathbf{p}^{\mathrm{t}\text{-}1}$ from the previous time step.

4.4.3 Vessel Tracking

The artery to be tracked can now be determined from the potential vessel positions $\mathbf{C}_{\mathrm{v}}$ and is described in Algorithm 2, which is based on [80]. Due to the continuous nature of the tracked vessel, the corresponding vessel centers should be close to each other in successive images. Thus, the tracked vessel is updated based on the minimum Euclidian distance between the potential vessel positions $\mathbf{C}_{\mathrm{v}}$ in the current image and the detected vessel center $\mathbf{p}^{\mathrm{t}\text{-}1}$ in the last frame. In addition, a maximum distance value $d_{\mathrm{v}} = 50$ pixels is defined to avoid incorrect assignments of the vessel

Algorithm 1 Clustering and Merging Red Regions

```
Input: Sorted red areas $\mathbf{C}_{\text{all}}$
Output: Clustered red areas $\mathbf{C}_{\text{v}}$
$\mathbf{C}_{\text{v}}, usedInd \leftarrow \{\}, \{\}$
for $i = 1; i < \text{len}(\mathbf{C}_{\text{all}}); i \leftarrow i + 1$ do
    if $i \notin usedInd$ then
        $curClust, refValue \leftarrow \{\}, \mathbf{c}_{\text{i}}$
        $usedInd \leftarrow usedInd \cup i$
        for $j = 1; j < \text{len}(\mathbf{C}_{\text{all}}); j \leftarrow j + 1$ do
            if $j \notin usedInd$ & CalcEuclDist$(refValue, \mathbf{c}_{\text{j}}) \leq r_{\text{cl}}$ then
                $usedInd, curClust \leftarrow usedInd \cup j, curClust \cup \mathbf{c}_{\text{j}}$
            end if
        end for
        $\mathbf{C}_{\text{v}} \leftarrow \mathbf{C}_{\text{v}} \cup curClust$
    end if
end for
return $\mathbf{C}_{\text{v}}$
```

Algorithm 2 Vessel Tracker

```
Input: Previous tracked vessel position $\mathbf{p}^{\text{t-1}}$, vessel candidates in current image
    $\mathbf{C}_{\text{v}}$
Output: Current tracked vessel position $\mathbf{p}^{\text{t}}$
$\mathbf{p}^{\text{t}} \leftarrow \mathbf{p}^{\text{t-1}};$
$d_{\text{min}} \leftarrow \infty$
$i_{\text{min}} \leftarrow -1$
for $i = 1; i \leq \text{len}(\mathbf{C}_{\text{v}}); i \leftarrow i + 1$ do
    $d_{\text{i}} \leftarrow \text{CalcEuclDist}(\mathbf{p}^{\text{t-1}}, \mathbf{C}_{\text{v}}(i));$
    if $d_{\text{i}} < d_{\text{min}}$ then
        $d_{\text{min}} \leftarrow d_{\text{i}};$
        $i_{\text{min}} \leftarrow i;$
    end if
end for
if $d_{\text{min}} \leq d_{\text{v}}$ then
    $\mathbf{p}^{\text{t}} \leftarrow \mathbf{C}_{\text{v}}(i_{\text{min}});$
end if
return $\mathbf{p}^{\text{t}}$
```

center. If the distances of the clustered areas are all above the limit value or no vessel candidate is detected at all, the vessel center of the previous image is retained.

4.5 Volunteer Study

To validate the proposed approach, a volunteer study with seven male and healthy volunteers was performed, in which the femoral artery was scanned by a robot. All volunteers signed informed consent, and the study was approved by the local Ethics Committee of the University of Lübeck. An LBR iiwa 14 redundant robot with seven DoF, an EPIQ 7 US station (Philips, Amsterdam, Netherlands), and the XL14-3 (Philips, Amsterdam, Netherlands) probe were used. For US data acquisition, the PLUS framework [89] was used in combination with a customized Dicom Network Library provided by Philips, allowing real-time access to image and volume data. As the US station does not have a direct interface to the Doppler signal, a frame grabber Cam Link 4k (Corsair GmbH, Munich, Germany) was used to receive the colored Doppler images from the screen of the US station. The recording frequency was 10 Hz for the Doppler X-Plane images and 25 Hz for the conventional 2D US data. The image depth was set to 50 mm, the resulting image spacing was 0.098 $\frac{mm}{px}$. During the study, a physician was present constantly.

The procedure of the volunteer study was as follows: First, while the robot was in gravity compensation mode with the US probe attached to the end effector, the starting point of the scan was determined by the physician (Figure 4.6A). This was the division of the common femoral artery into the profunda femoral artery and the superficial femoral artery. Then two automatic US scans (Figure 4.6B) were performed, with each experiment being repeated three times. The maximum scan length of the superficial femoral artery was set to 20 cm. While scanning, either template matching (see Section 4.4.1) or Doppler signal tracking (see Section 4.4.2 was used to track the vessel's center. To position the probe appropriately, the distance e_c between the center of the US image showing the cross-section plane and

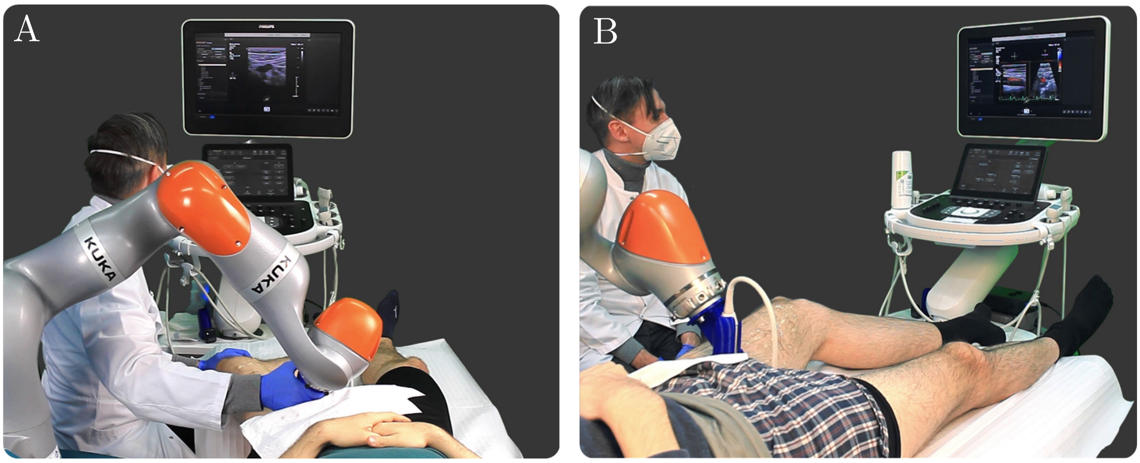

Figure 4.6: Experimental setup of the volunteer study. **A:** The physician positions the transducer to the starting point of the artery scan. **B:** The femoral artery is scanned automatically by the robot, using the Doppler signal tracking to center the vessel while moving along the proband's leg.

the tracked vessel center (Figure 4.4) was calculated. If this distance e_c exceeded the defined threshold $e_{\text{thr}} = 50$ px, the probe was moved by the robot in the direction of the vessel. Otherwise, the probe was moved forward along the vessel as defined in Eq. 4.15.

For evaluation purposes, the vessel tracking accuracy as well as the automatic vessel centering were investigated. The actual vessel centers of the recorded US data were labeled by another physician. In addition, the accuracy of the applied probe contact forces was analyzed.

4.5.1 Vessel Tracking Accuracy

The total mean vessel tracking error of all scans performed is 13.9 (± 6.4) px or 1.36 (± 0.63) mm for the template matching approach and 10.7 (± 3.1) px or 1.05 (± 0.3) mm for the Doppler tracking approach. This results in a 23 % lower error when using Doppler tracking. The difference is even more apparent when the tracking accuracy is evaluated in relation to the distance to the start pose of the scan. Figure 4.7 shows the error between the determined vessel center and the labeled ground truth, depending on the distance to the scan's start pose.

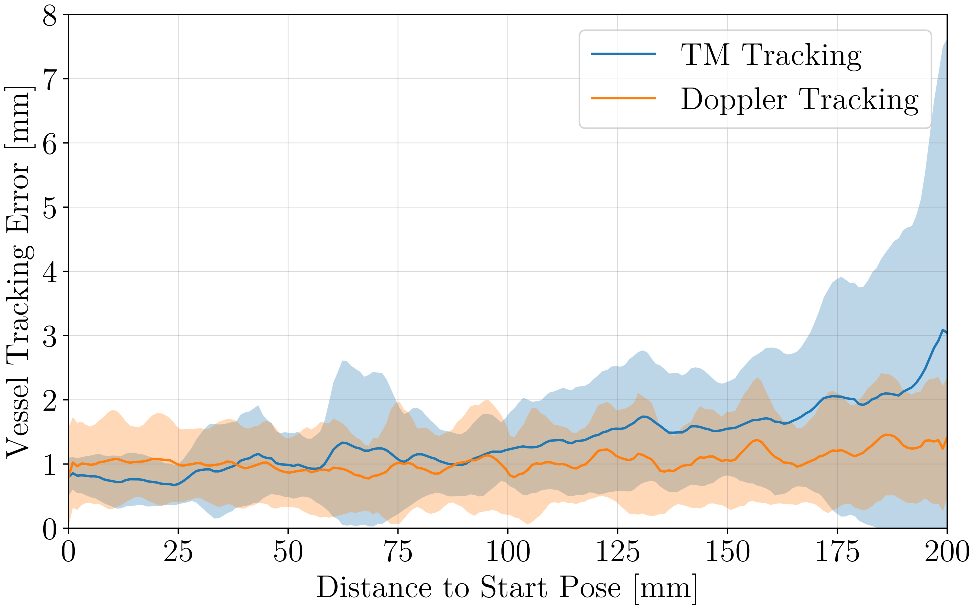

Figure 4.7: Accuracy of vessel tracking over the distance to the start pose of all scans performed. The blue line represents the mean tracking error using the template matching approach, the orange line represents the mean error using the Doppler approach. The corresponding standard deviations are indicated by the colored transparent bands around the curves.

The blue line represents the average error and the area highlighted in light blue the standard deviation of the template matching approach. The orange line represents the respective results for the Doppler tracking approach. It can be seen that the tracking errors at the beginning of the scan are at about the same level of approx. 1 mm. After a scan length of approx. 100 mm, the error of the template matching approach increases, while the error of the Doppler tracking remains constant. The more distance covered, the less accurate template matching becomes, which can also be recognized by the very large standard deviation towards the end of the scan. The reason for this is that the vessel geometry changes over the distance traveled. This makes template matching, which uses the vessel cross-section at the start of the scan as a reference image, less reliable. Especially towards the end of the scan, it is difficult even for a physician to recognize the vessel cross-section. This is where analyzing the blood flow using the Doppler signal is a great advantage, as the vessel can still be detected. It should therefore also be noted that due to the poorer visibility of the vessel towards the end of the scan, less accurate labeling could influence the results, especially of the template matching approach. Another advantage of vascular tracking using Doppler signals is the ability to differentiate between veins and arteries based on the visualized blood flow color. This means that false detections of purely image-based methods (e.g. template matching, or neural networks trained on US images) due to the similarity between artery and vein can be avoided. For future work, a combination of both methods could be considered, which combines the advantages. In some cases, no Doppler signal can be detected because the probe is not optimally aligned, even though the vessel is visible. Furthermore, in patients with severe peripheral arterial occlusive disease, the femoral arteries may no longer be sufficiently perfused, making it difficult or even impossible to obtain a Doppler signal. The combination of template matching and Doppler signal could then help to follow the course of the vessel into the periphery. To include the change in the vessel cross-section over the scan, the template should be updated repeatedly.

Some related work described in the literature achieved slightly higher vessel tracking accuracies of 0.89 mm in [67] and 0.38 mm in [78]. However, their validation was done on phantoms, and the neural networks used for recognition were trained with data from the same phantom. In addition, the scan distance in the experiment described in this chapter is 20 cm instead of 14 cm in [67] and [78], and thus much larger. Especially in the last part of the scans, the leg vessel is more difficult to see, which reduces the accuracy of vessel recognition in the realistic subject data.

4.5.2 Contact Force Accuracy

The forces acting on the end effector in the direction of the ${}^{tcp}z$-axis of the probe for all the scans performed are shown in Figure 4.8. The forces were measured using the torque sensors in the robot's joints and the force estimation model provided by the manufacturer. It can be seen that after the start of the scan, the contact force increases until the desired value of 5 N is reached. The average measured force then decreases slightly until it reaches approx. 4.4 (± 0.7) N at the end of the scan, which is 0.6 N below the desired target value. The deviation can be explained by inaccuracies in the robot model. Friction and hysteresis effects can lead to inaccuracies in the estimation of internal joint torques, particularly at slow speeds and low external forces acting on the end effector. In addition, the gravity due to the weight of the probe and the probe's cable was neglected. The inaccuracy of the estimation of the internal torques then also leads to an inaccurate estimation of the

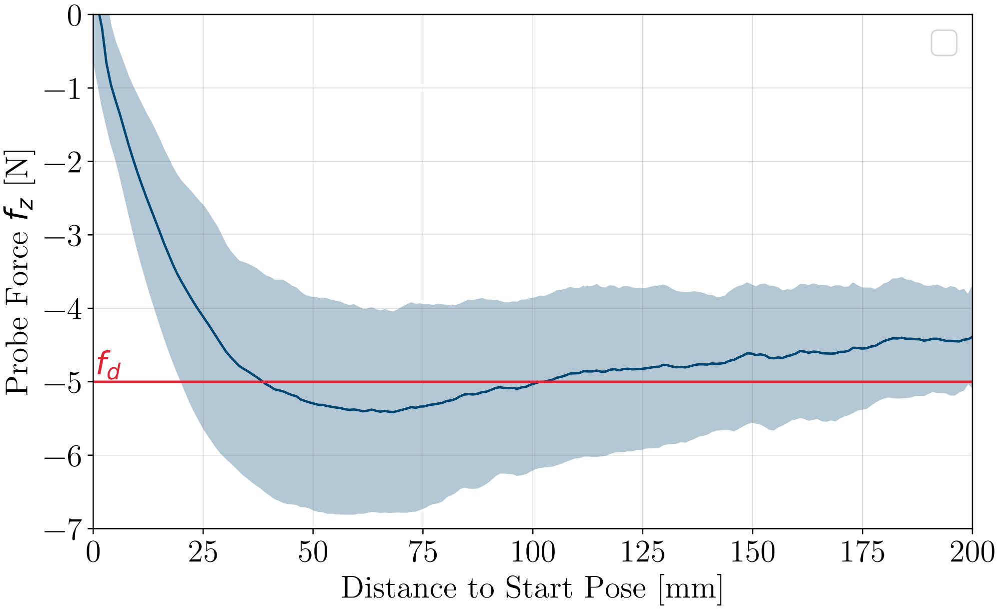

Figure 4.8: Contact forces f_z acting in the direction of the ${}^{tcp}z$-axis of the probe over the distance to the start pose for all scans. The mean forces are shown as a dark blue line, and the corresponding standard deviations are highlighted in lighter blue. The value of the desired contact force f_d is shown as a red line.

external torques $\boldsymbol{\tau}_\mathrm{ext}$, which are used for the robot's force control (see Eq. 4.13). This could affect the controller shown here, as no Cartesian force measurement is used as feedback, which might be further investigated in future work.

4.5.3 Vessel Centering

To keep the vessel centered during movement, the position of the probe must be adjusted. Figure 4.9 shows an example of the movement of the US probe in the transversal direction to the vessel's cross-section in blue. Moreover, the distance e_c between the center of the US image and the detected vessel center is shown in red. During this scan, the threshold $e_\mathrm{thr} = 50$ px is exceeded nine times, which is shown by the grey circles. Each time the threshold is reached, the probe is moved in the opposite direction, which is illustrated by the step-like blue curve. This shows that the robot follows the detected vessel cross-section. Therefore, the probe can be guided along the vessel. However, it must be noted that there are many corrective movements. This is because the compensation movement stops as soon as it falls below the threshold value. If the vascular curvature continues, another correction is required shortly afterwards, and so on. To reduce the number of required corrective movements, a further threshold value $e_\mathrm{thr,ad} < e_\mathrm{thr}$ can be introduced in future work. A commanded compensation movement (triggered by exceeding e_thr) then continues until the distance between the image center and the vessel falls below this threshold $e_\mathrm{thr,ad}$.

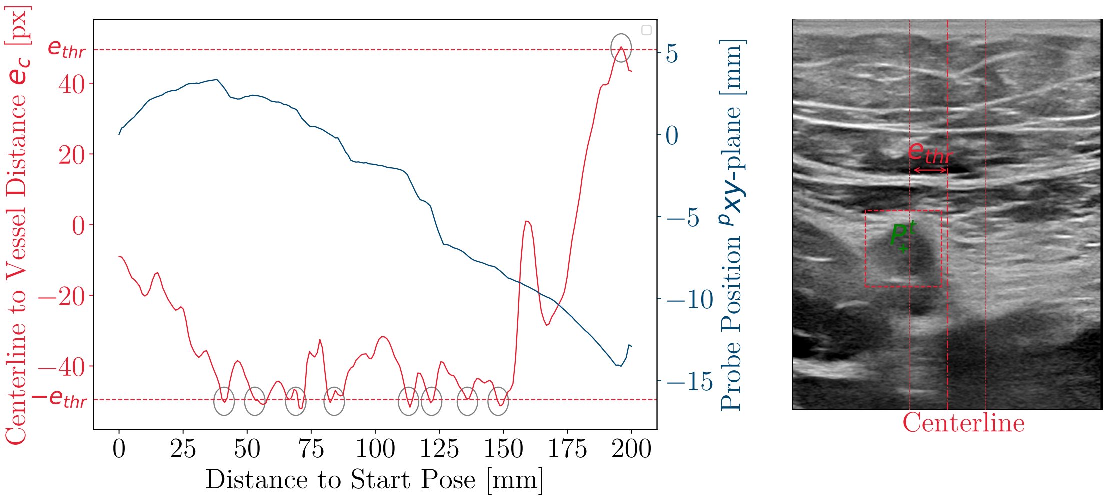

Figure 4.9: The diagram on the left shows the movement of the US probe in the transversal direction to the vessel's cross-section in blue for an experiment. The distance e_c between the centerline of the US image and the detected vessel center is represented in red. Exceeding the threshold $e_{\text{thr}} = 50$ px is indicated by the grey circles. The right-hand side of the figure shows an example of an US image in which the centerline (dot-dashed red line) to vessel ($\mathbf{p}^t$) distance e_c was higher than the defined threshold $e_{\text{thr}} = 50$. This results in a corrective movement of the probe to keep the vessel centered.

4.5.4 Scanning and Processing Times

The mean total scan time was 44.7 s for the template matching approach and 37.2 s for the Doppler tracking approach. The lower scanning times for the Doppler tracking approach are due to more precise tracking, reducing false detections and unnecessary robot movements. The acquisition of standard 2D US images took on average 40 ms (25 Hz), while the acquisition of X-Plane Doppler data took 100 ms (10 Hz), due to technical limitations of the hardware used. The template matching approach for vessel tracking required 12 ms on average, while processing and tracking Doppler images needed 10.5 ms.

From a clinical perspective, there are no fixed guidelines regarding the duration of a diagnostic US scan. Rather, the divergence between individual examiners is very strong and could be sharply reduced with the help of robotic US. An average sonographic examination of the arteries of both legs is stated in patient information forms to take around 30-60 minutes [4], [90]. Even though a direct comparison with the scan times achieved is limited as patient preparation (e.g., undressing, applying gel) was not included, the measured robotic US times are well below current clinical routine, highlighting the system's potential for increased efficiency.

4.6 Conclusion

In this chapter, a robotic system for automatic scanning of the leg artery (superficial femoral artery) was presented. Two image-based methods were tested to detect the artery and adjust the transducer position accordingly. First, template matching was employed to track the cross-section of the artery in conventional US images. In addition, the colored Doppler US signal was used for vessel tracking, which proved to be the more effective option. Compared to existing methods in literature that use neural networks for vessel detection (e.g. [80], [78]), the approach shown has two major advantages: Firstly, no training data or labeling is required. In particular, to cover different US device settings and different patient-specific vessel morphologies, an extremely large amount of training data would have to be available to ensure robust vessel detection performance. Recording this data is difficult to achieve, especially if data from patients suffering from vascular diseases is required. Secondly, the outputs of the presented vascular tracking can be easily understood as there is no black box behavior. This interpretability of the vessel tracking contributes to patient safety, as the robot navigates along a path derived from these results, preventing unexpected maneuvers.

5

ADDITIONAL FEATURES FOR ROBOTIC ULTRASOUND

In the previous chapter, it was shown that arterial scans of volunteers could be successfully performed with the robotic system, fulfilling the core functions. The following chapter deals with the development of additional features to further expand the system's capabilities. The respective topics covered are outlined in Figure 5.1.

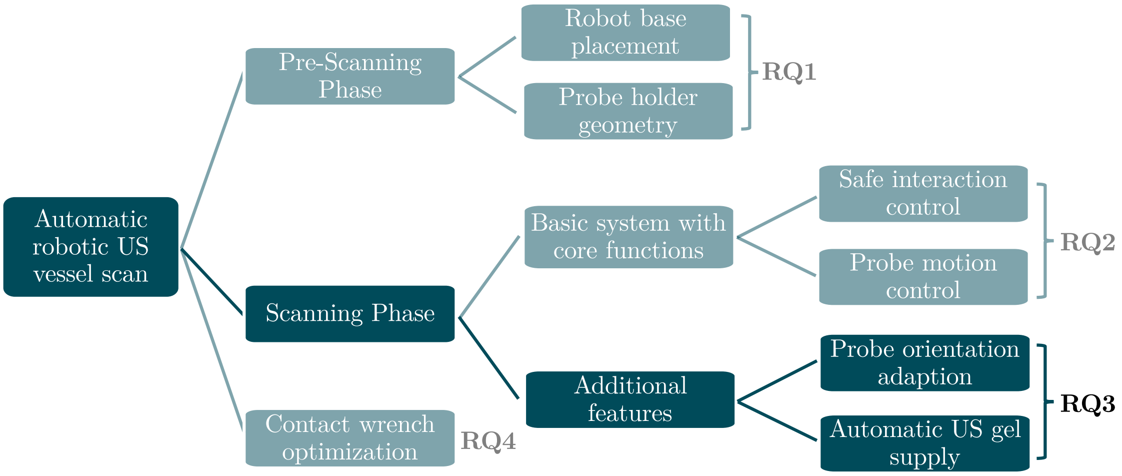

Figure 5.1: Structure of the thesis. The essential topics required for an automatic robotic US examination are addressed in individual chapters, with the content of this chapter highlighted in dark blue.

Based on this, the following research question is addressed:

> **Research Question 3**
> How can the additional features of automatic probe orientation adaption and US gel supply be integrated into the robotic US system?

An automatic adjustment of the probe's orientation can be useful to scan strongly curved surfaces with full probe contact. For that reason, a method to determine a rotational compensation movement to automatically align the probe to the approximate surface normal is proposed in the following Section 5.1. Subsequently, to further increase the system's degree of automation, an automatic US gel supply is presented in Section 5.2. The robot's seventh degree of freedom is exploited in combination with a passive mechanism, requiring no additional electronic components.

5.1 Automatic Probe Alignment[3]

Acquiring reproducible US images of high quality is challenging. The image quality mainly depends on the contact force [92] as well as the orientation of the probe [93]. While physicians can rely on their experience, robot-assisted systems must be able to automatically align the ultrasound probe with the correct orientation. It was concluded in [94] and [95] that an orientation along the normal of the surface leads to improved image quality. Several approaches in the literature focus on automated normal probe alignment based on external sensors. In [96]–[98], depth cameras were used, while [99] attached laser distance sensors to the probe holder to automatically adjust the probe's orientation to the surface normal. However, the integration of additional sensors leads to an increased system complexity. For that reason, various articles employed approaches, which are solely based on US data. For example, [95], [100], [101] use confidence maps [102], to accordingly adjust the probe's orientation. Finally, [103] combines confidence maps with the robot's estimated contact forces acting on the probe to determine the optimal orientation.

In the following, a new method to align the central axis of the probe to the surface normal at the point of contact is provided. This is done by analyzing the area of 3D ultrasound volumes directly below the transducer of the probe. A convolutional neural network (CNN) is trained to estimate the inclination of the probe towards the direction of the surface normal, such that the robot can correct the probe's orientation immediately.

5.1.1 Data Acquisition

The acquisition of training data was done with an LBR iiwa 7 robot and an EPIQ 7 US station with the XL14-3 probe at different locations on two leg phantoms and one torso phantom (see Figure 5.2). US volumes were acquired at six different locations on the torso phantom, at four different locations on the transparent leg phantom and at two locations on the red leg phantom. First, the probe is aligned by hand at a chosen location. The probe has full contact to the phantom surface and the orientation is approximately aligned to the surface normal though no ground truth is known. To acquire data with different contact angles at the contact point, in a second step, the probe orientation is varied in a range from -15° to 15° at a step size of 3° as visualized in Figure 5.3. This is done by rotating the probe around the ${}^{tcp}y$- and ${}^{tcp}x$-axes of the tcp-frame, which is located in the center of the probe as shown in Figure 5.3. $\Delta\theta_{\mathrm{IP}}$ and $\Delta\theta_{\mathrm{OP}}$ represent the angles by which the probe must be rotated to be aligned with the approximate surface normal in the in-plane and out-of-plane directions, respectively (see Figure 5.3). First, the probe is rotated around its ${}^{tcp}y$-axis by a corresponding angle of $\Delta\theta_{\mathrm{IP}}$ while $\Delta\theta_{\mathrm{OP}} = 0°$. Afterwards, the probe is rotated around its ${}^{tcp}x$-axis by a corresponding angle of $\Delta\theta_{\mathrm{OP}}$ while $\Delta\theta_{\mathrm{IP}} = 0°$. In addition, the probe pressure force onto the phantom surface is varied for each probe orientation. The probe is moved in 2 mm steps in the ${}^{tcp}z$-direction until a depth of 10 mm is reached. This varies the range of contact forces that occur

---

[3] Parts of this section have been published in [91].

with the aim of achieving higher data variability. During this process, the US data as well as the force and position data provided by the robot are stored.

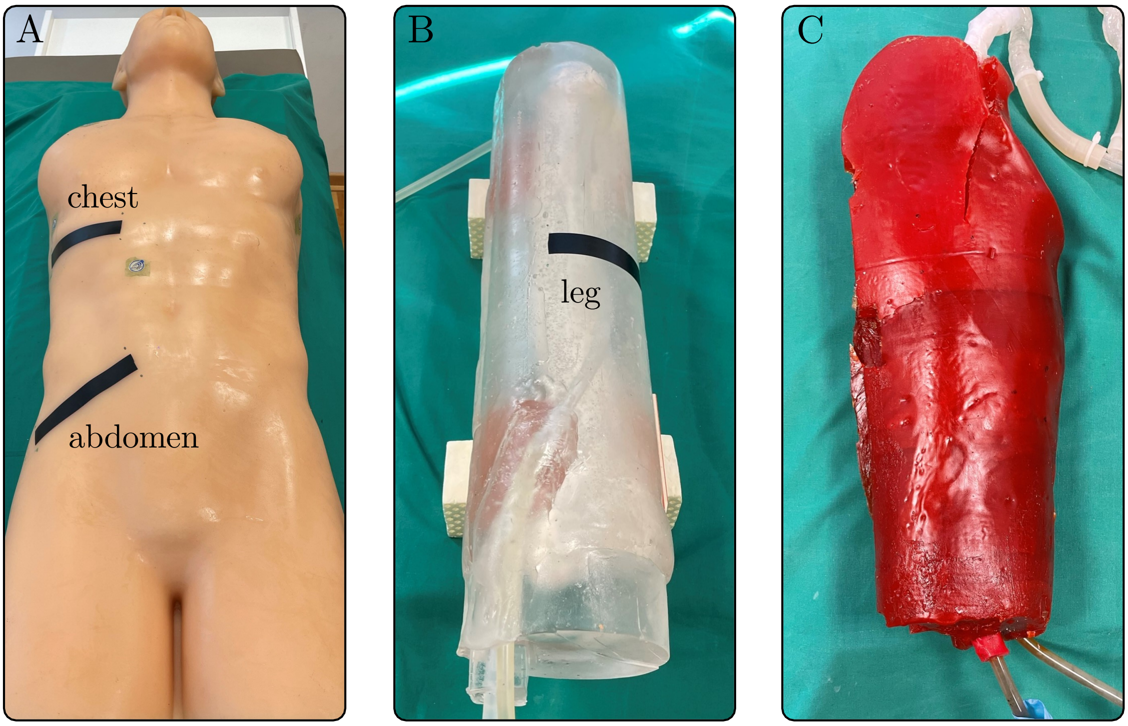

Figure 5.2: Phantoms for data acquisition and validation. **(A)**: Torso phantom. **(B)**, **(C)**: Leg phantoms. The validation scans are marked with black tape.

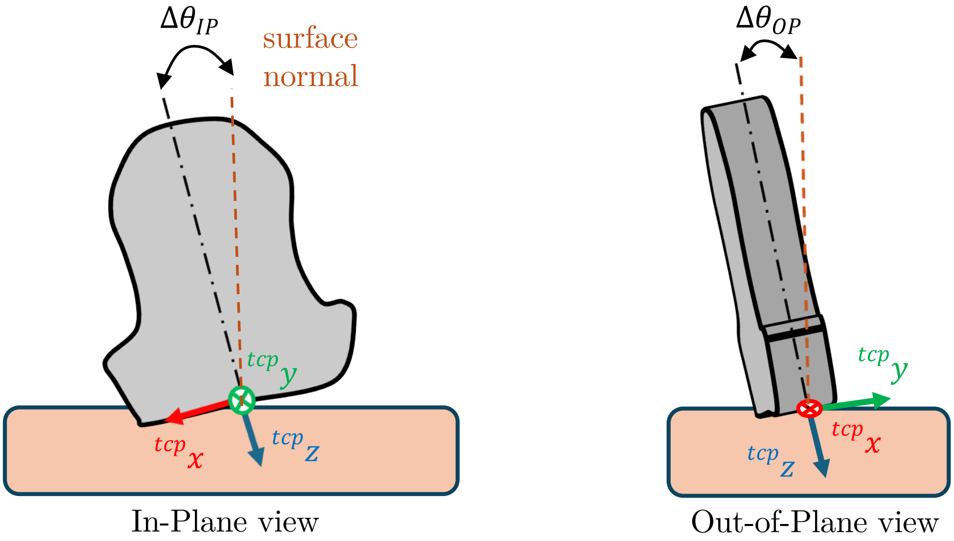

Figure 5.3: For data acquisition, the probe orientation was varied between -15° and 15° in steps of 3° in both rotation directions.

5.1.2 Data Preparation

After acquisition, the data is prepared for CNN training. The proposed approach for estimating the required US probe rotation angles $\Delta\theta_{\mathrm{IP}}$ and $\Delta\theta_{\mathrm{OP}}$ is based on both, forces and images. Depending on the area of interest, US volumes can contain highly different anatomical structures. To be invariant to this structural variability, not the whole US volume, but only the area directly under the US probe, was used. This *transducer area*, marked in Figure 5.4, has no information about the anatomical structure but about the probe-surface contact. Transducer area patches are cut out from the US volumes at a depth of 30 px as visualized in Figure 5.4.

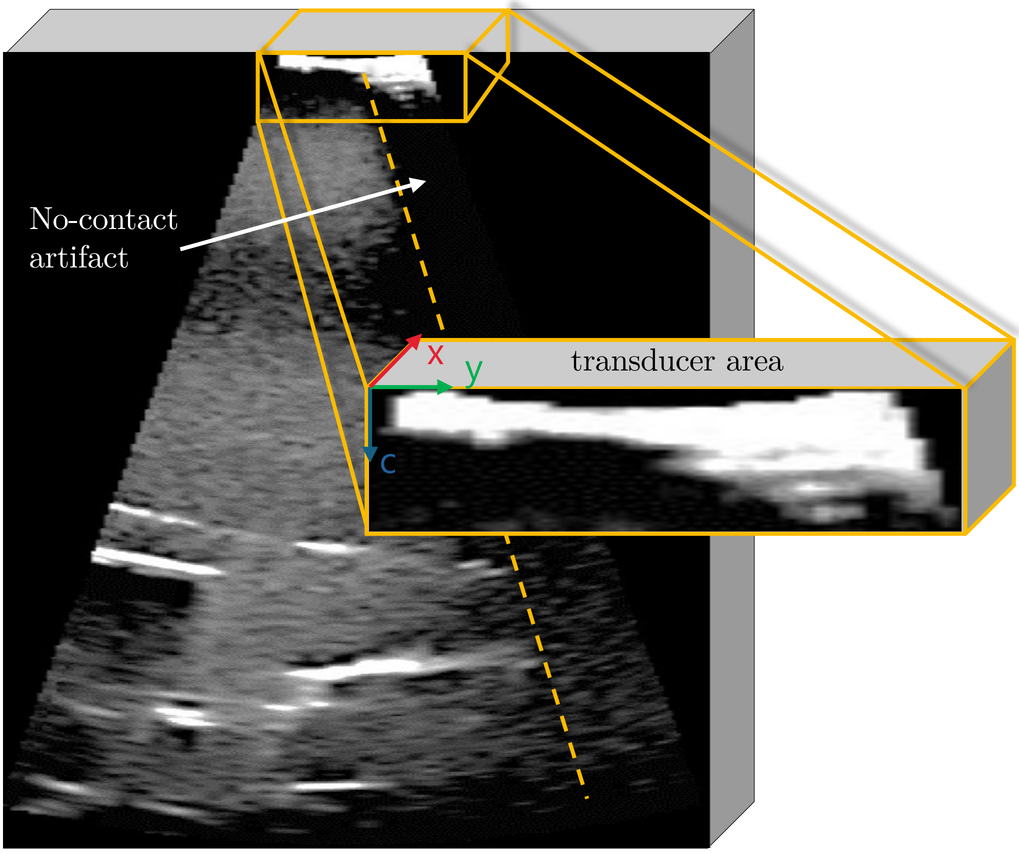

Figure 5.4: A slice of a 3D US volume acquired at a probe orientation of $\Delta\theta_{\mathrm{IP}} = 0°$, $\Delta\theta_{\mathrm{OP}} = -12°$. The transducer and the non-contact artifact are marked.

In a second step, these patches are resampled into a size of 30 px × 30 px × 30 px. To extend the available data set, random intensity rescaling is applied to the patches so that 12,548 data samples are available for training. The measured forces ${}^{\mathrm{ee}}\mathbf{f}$ are given in the end effector coordinate system. The forces ${}^{\mathrm{ee}}\mathbf{f}$ are transferred to the US probe coordinate system by applying the transformation matrix ${}^{\mathrm{ee}}\mathbf{T}_{\mathrm{tcp}}$, which is known from the CAD model of the probe holder, resulting in ${}^{\mathrm{tcp}}\mathbf{f}$. Using the probe contact force ${}^{\mathrm{tcp}}\mathbf{f}$ for angle estimation is an important aspect, since the US image quality can be affected by both, pressure and orientation due to the soft and flexible skin of humans or phantoms. In addition, a rough estimation for the rotation direction d_t is calculated by determining the US volume moment M

$$M = \sum_{x,y,z} x^i y^j z^k I(x,y,z). \tag{5.1}$$

Here, $I(x,y,z)$ is the US volume intensity at position (x,y,z). As can be seen in Figure 5.4, volumes acquired at a suboptimal probe orientation contain a shadow artifact that extends over the entire depth of the US volume. Due to that, the volume moment is shifted into the opposite direction. According to this, the parameter $d_\mathrm{t} = (d_\mathrm{t,IP}, d_\mathrm{t,OP})^\mathrm{T}$ with $d_\mathrm{t,IP} \in \{-1,1\}$ and $d_\mathrm{t,OP} \in \{-1,1\}$ is set based on the shift direction of the volume moment for the in-plane and out-of-plane angles of the ultrasound probe. It should be noted that d_t could also be received by labeling the data, determining the volume moment is done to avoid the time-consuming labeling process.

5.1.3 Convolutional Neural Network

The required probe rotation is estimated using a two-dimensional Regression CNN visualized in Figure 5.5. The CNN consists of nine convolutional layers with relu activation function, two max-pooling layers and four fully connected layers with sigmoid activation function. In the output layer, a linear activation function is used. The CNN gets a 30 px × 30 px × 30 px sized volume and the force vector ${}^{\mathrm{tcp}}\mathbf{f}$ as input. Since the CNN used is a two-dimensional model, the information along the depth axis of the US volume is handled as 30 different channels inside the CNN. Output of the model are the angle predictions $\Delta\theta_\mathrm{IP}$ and $\Delta\theta_\mathrm{OP}$ for the required rotation of the US probe. Training is performed using the rmsprop optimizer with a batch size of 128, validation split of 10 %, early stopping, exponential learning rate decay and a custom loss function, given in Eq. (5.2):

$$Loss = L_{Rotation} + L_{Direction}. \tag{5.2}$$

Here, $L_{Rotation}$ (see Eq. 5.3) calculates the difference between the predicted US probe rotation and the ground truth considering the rotation matrices $\mathbf{R}_\mathrm{p}$ and $\mathbf{R}_\mathrm{t}$ using the Frobenius norm:

$$L_{Rotation} = ||\mathbf{R}_\mathrm{p} - \mathbf{R}_\mathrm{t}||_\mathrm{F}. \tag{5.3}$$

The rotation matrix prediction $\mathbf{R}_\mathrm{p}$ is generated using the predicted angles $\Delta\theta_\mathrm{IP}$ and $\Delta\theta_\mathrm{OP}$ while $\mathbf{R}_\mathrm{t}$ is known from the data acquisition. By using $L_{Direction}$ (see Eq. (5.4)), predictions are penalized even stronger if the direction of the predicted rotation is wrong:

$$L_{Direction} = \begin{cases} 1, & \text{if } d_\mathrm{p} \neq d_\mathrm{t} \\ 0, & \text{otherwise.} \end{cases} \tag{5.4}$$

Here, $d_\mathrm{p} = (d_\mathrm{p,IP}, d_\mathrm{p,OP})^\mathrm{T}$ denotes the rotation directions of the predicted angles $\Delta\theta_\mathrm{IP}$ and $\Delta\theta_\mathrm{OP}$, where $d_\mathrm{p,IP} \in \{-1,1\}$ and $d_\mathrm{p,OP} \in \{-1,1\}$. If these predicted rotation directions do not match the directions $d_\mathrm{t} = (d_\mathrm{t,IP}, d_\mathrm{t,OP})^\mathrm{T}$ derived from the US volume moment (see Section 5.1.2), an additional penalty is applied. With this, the CNN is forced not to give rotation predictions that point into the opposite direction as required. Note, that d_t and d_p are only used for training. When the CNN is used for prediction, these calculations are not performed.

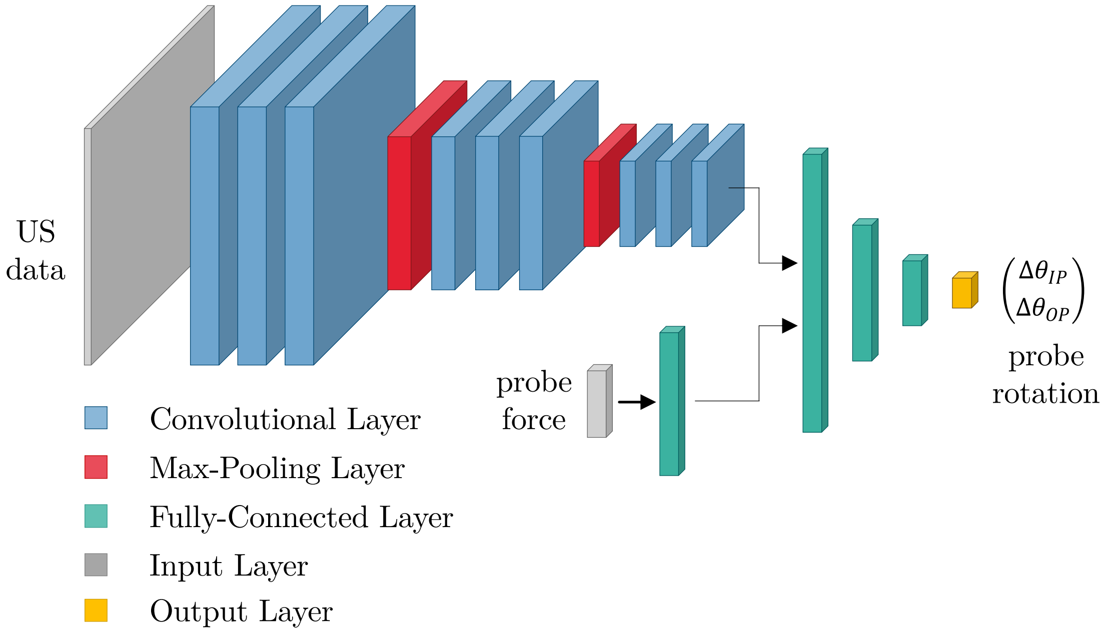

Figure 5.5: Visualization of the CNN architecture. It receives an US volume and a force vector as input and predicts the required rotation angles of the probe $\Delta\theta_{\mathrm{IP}}$ and $\Delta\theta_{\mathrm{OP}}$.

5.1.4 Validation Experiments

For validation, a phantom study is performed where several automated US scans of two different phantoms are executed. For each scan, the probe is positioned by hand at a start position on the phantom and the following scanning procedure is executed as shown in Figure 5.6. First, the contact force of the probe is adjusted to be in a range between 3 and 5 N by adapting the probe pose in the ^{tcp}z-direction (see ① in Figure 5.6). Afterwards, an US volume is acquired and the rotation angles to align the probe are estimated by the CNN. If the absolute values of the predicted angles are greater than 3°, the probe is rotated appropriately (see ② in Figure 5.6). Otherwise, the probe orientation remains constant. This threshold is chosen due to the step size of 3° in the training data acquisition. In the third step, the next path point is approached by moving the probe 5 mm into the ^{tcp}x- direction (see ③ in Figure 5.6). In total, two validation trajectories on the torso phantom and one on the transparent leg phantom are chosen (see black tape in Figure 5.2). At each location, five scans are performed. To evaluate the accuracy of the orientation alignment, the surface normals of the corresponding paths are determined by a laserscan done with an Artec Leo (Artec 3D, Senningerberg, Luxembourg) laserscanner. The path is then divided equally into 24 areas for the scans on the torso phantom (chest and abdomen) and in 16 areas for the scan on the leg phantom. The mean surface normals of these areas are used to calculate the absolute angle error to the probe's ^{tcp}z-axis for each position of the trajectory.

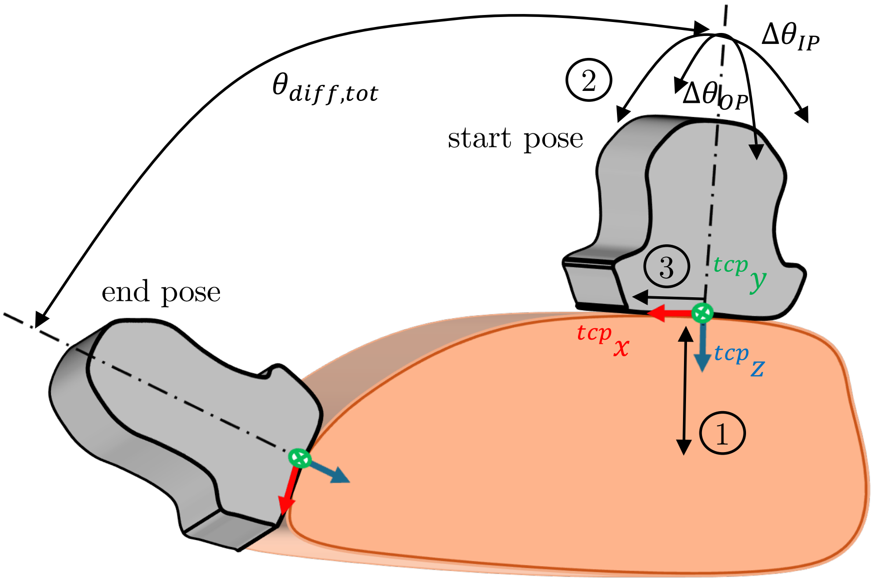

Figure 5.6: Procedure of validation scans: The probe ^{tcp}z-axis is automatically aligned with the surface normal while scanning a curved tissue. $\theta_{\mathrm{diff,tot}}$ is the difference between the surface normal at the start and the end position. Step (1): Probe position is adapted along the probe ^{tcp}z-axis in order to achieve a contact force between 3 and 5 N. Step (2): An ultrasound volume is acquired and the correction angles to align the probe with the surface normal are estimated, and the probe is rotated. Step (3): Move probe 5 mm into ^{tcp}x-direction. The procedure is repeated 24 times for the scans of the torso phantom and 16 times for the scan of the leg phantom.

5.1.5 Alignment Accuracy

For evaluation, the absolute angle errors measured between the mean surface normals and the ^{tcp}z-axis of the US probe are investigated. The measured in-plane and out-of-plane angle errors are summed and considered jointly. In Figure 5.7, the absolute angle errors of all five iterations of the three validation scans are visualized. The mean absolute angle error over all experiments is $5.0° \pm 2.8°$ and in 95 % of the probe positions the angle error is $\leq 9.7°$. However, the results indicate that the accuracy of the leg phantom is higher than of the torso phantom. In the leg experiments, the mean angle error is $3.8° \pm 2.9°$ while the error on the chest and abdomen is $5.3° \pm 2.7°$ and $5.5° \pm 2.6°$, respectively. Altogether, during the scans the probe had to rotate for 61.8°, 30.7° and 74.2° in the chest, abdomen, and leg experiments, respectively. The robot was able to hold the probe in full surface contact the whole time during all experiments. Outliers, meaning probe positions where the angle error is quite high, could always be compensated in the following probe position.

5.1.6 Discussion and Conclusion

The goal of the presented approach is to automatically adjust the probe's orientation during the scan. Based on the US volume and the force acting at the end effector, a target orientation R_{d} is calculated to align the central ^{tcp}z-axis of the probe approximately normal to the surface of the scanned tissue. The results show that trajectories at unknown curved surfaces can be scanned automatically by an

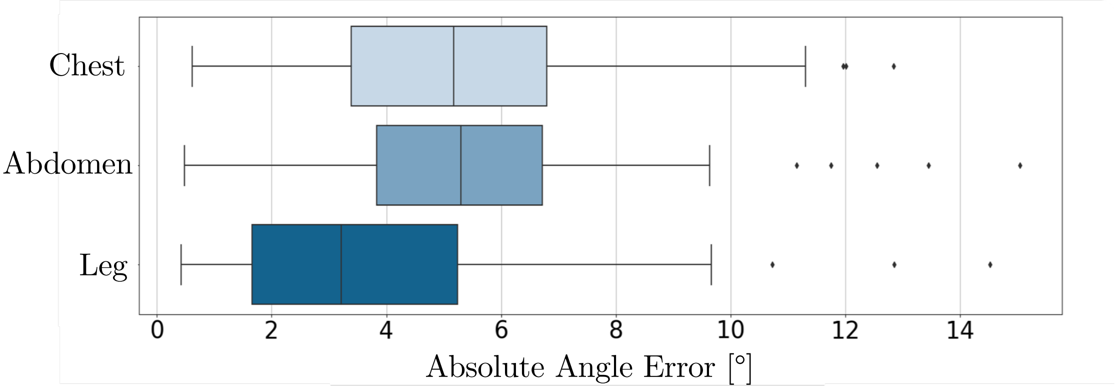

Figure 5.7: Absolute angle error results for chest, abdomen and leg experiments. In each location five iterations are performed. The sum of the in-plane and out-of-plane errors are visualized.

US robot, ensuring full probe contact. The proposed method is applicable even in areas where orientation adaptions of more than 70° are required. The overall mean angle error is $5.0° \pm 2.8°$. Since the probe orientation is only adapted if the estimated rotation is $\geq 3°$, this can be considered as high accuracy. Since the smallest rotation in the training data is 3°, the CNN is not expected to estimate smaller angles accurately. In addition, although the method is validated by measuring the error between the surface normal and the probe orientation, the CNN is not trained to align the probe to the surface normal. When acquiring the training data, the ground truth for the optimal probe orientation was set manually. Thus, the CNN estimates the required rotation to reach US volumes without non-contact artifacts, shown in Figure 5.4. This can be achieved even if the US probe is not optimally aligned to the surface normal, thus, errors are expected when comparing the probe orientation and the surface normal. This effect even increases at higher pressure forces, which makes it necessary to use force information for an accurate rotation angle estimation. Compared to results from [103] the performance of the methods are comparable. Though, in contrast to [103], the presented approach is based on 3D US images so it is not necessary to perform a fan motion pattern for probe alignment. Another benefit of the proposed method is the invariance to the anatomical area of interest. The results show that the CNN generalized for the chest, abdomen and leg areas where the anatomy differs greatly. This was achieved by using the transducer area of the US volumes instead of the whole US volume. These anatomical areas of interest were, however, part of the training data, so the method was not tested on completely unknown areas of interest. Thus, there is still potential for improvement. The training data set should be extended with samples at rotation angles less than 3° as well as data from further areas of interest to extend the data variability. Another approach would be to determine only the direction of the probe's rotation to be aligned correctly, rather than directly predicting the exact optimal orientation. With visual servoing, knowing which way to rotate is sufficient, and calculating a precise angle is not necessary. Thus, instead of a regression network, a classification network could be tested. Moreover, the method should be tested on unknown phantom structures as well as on *in-vivo* data to investigate the practical clinical application of this approach.

5.2 Automatic US Gel Supply[4]

Ultrasound gel is used as a coupling medium in ultrasound procedures, thereby ensuring the entry of sound waves into the body of the patient and providing ultrasound images of high quality. For this purpose, US gel is applied to the body of the patient by therapy staff before the examination starts. However, an automated gel supply system would be required for fully automated US scans. The properties of US gel, though, make automated delivery difficult, as it has a very high viscosity. Despite its practical relevance, this topic is still largely unexplored. One notable exception is the work by [105], where a customized probe holder with an integrated mechatronic US gel dispenser is presented. The system consists of a gel-filled syringe and a linear actuator that pushes the syringe plunger to dispense the gel. In addition, a camera is used to verify the presence of US gel on the contact surface. A neural network processes the input from the camera, providing feedback to ensure that the gel has been sufficiently applied before the ultrasound examination begins. Although the gel dispenser was able to demonstrate its functionality, it leads to considerably increased system complexity due to the external mechatronic components. This additional complexity can lead to problems with system reliability, patient safety, and higher costs. The following approach for the automatic supply of US gel avoids this problem by combining a passive mechanism and advanced motion control to exploit the nullspace of a seven DoF redundant robot. This allows fully automated robotic US investigations without the need of external electronics.

5.2.1 Mechanical Design

The LBR iiwa 14 redundant robot with seven DoF and an EPIQ 7 US station with the X6-1 probe were used. To attach the US probe to the robot's flange, a custom US gel dispenser was developed. The proposed US gel dispenser consists of only a few parts, which can be 3D printed easily. The mechanical design is shown in Figure 5.8. A cosmetic gel tube with a filling quantity of 60 ml was used as reservoir for the US gel. This tube was inserted in a 3D printed gel dispenser, which was directly attached to the US probe holder. To achieve a flow of gel through the nozzle of the gel dispenser, pressure must be applied to the tube. This was done by means of a lever attached to the robot link between the sixth and seventh joints, which acts as a push mechanism. Before the start of the robot-assisted examination, this lever was fixed directly next to the gel reservoir. Thus, appropriate movement of the seventh joint causes the tube to move into the lever and the resulting pressure causes the gel to flow.

5.2.2 Robot Nullspace Control

In Section 4.3.2 of Chapter 4, the application of the Jacobian pseudoinverse method for the probe's motion control has already been described. The respective angular velocities for a desired twist $\boldsymbol{\nu}_\mathrm{d}$ are calculated by Eq. (4.11). However, the robot's redundancy has not been taken into account so far. In the case of redundancy of the

---

[4] Parts of this chapter have been published in [104].

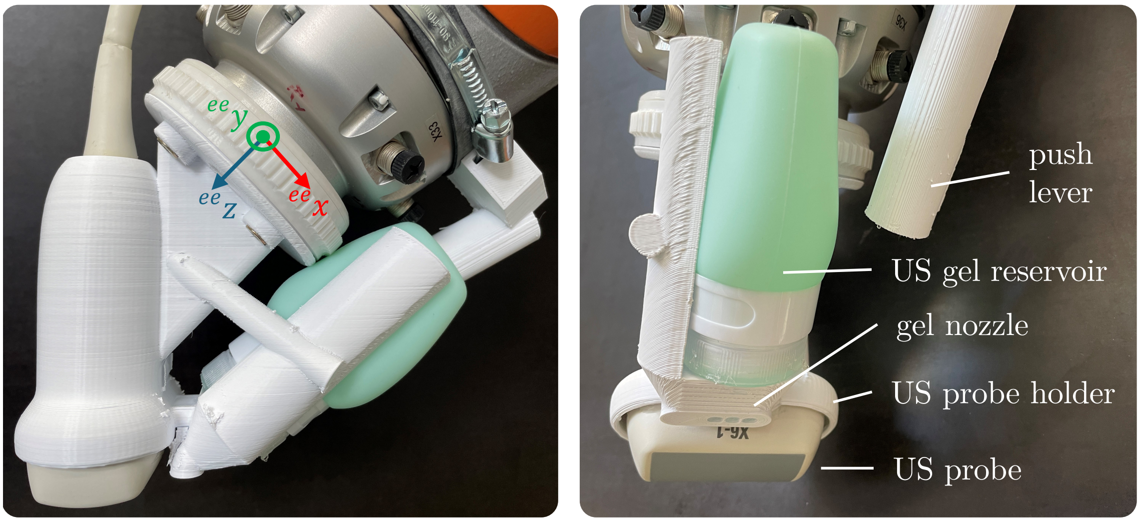

Figure 5.8: Mechanical design of the gel dispenser attached to the end effector of a robot. It consists of a 3D printed probe holder, where a gel reservoir is included. When the tube is pressed in using the push lever, US gel is dispensed through the nozzle.

manipulator, a more general solution of Eq. (4.11) can be provided for simultaneous execution of two Cartesian tasks $T_1 := (\mathbf{J}_1, \boldsymbol{\nu}_{\mathrm{d},1})$ and $T_2 := (\mathbf{J}_2, \boldsymbol{\nu}_{\mathrm{d},2})$ using task prioritization [106]. The joint velocities $\dot{\mathrm{q}}_{\mathrm{mc,p}}$ required to fulfil the two tasks and the prioritization of T_1 over T_2 are calculated by:

$$\dot{\mathbf{q}}_{\mathrm{mc,p}} = \mathbf{J}_1^{\dagger}\boldsymbol{\nu}_{\mathrm{d},1} + [\mathbf{J}_2(\mathbf{I} - \mathbf{J}_1^{\dagger}\mathbf{J}_1)]^{\dagger}(\boldsymbol{\nu}_{\mathrm{d},2} - \mathbf{J}_2(\mathbf{J}_1^{\dagger}\boldsymbol{\nu}_{\mathrm{d},1})). \tag{5.5}$$

In the scenario considered here, the first task T_1 is the Cartesian movement of the US probe to scan a certain area of the body, specified as twist $\boldsymbol{\nu}_{\mathrm{d},1}$. This task is given priority over the second task T_2, which represents the rotational movement $\boldsymbol{\nu}_2$ of the tube into the lever, applying US gel. $\mathbf{J}_1$ is the Jacobian associated with the Cartesian motion of the probe $\boldsymbol{\nu}_{\mathrm{d},1}$ and $\mathbf{J}_2$ is the Jacobian belonging to the corresponding rotational motion $\boldsymbol{\nu}_{\mathrm{d},2}$ of the end effector to push the tube into the lever. Since the US gel feed can be activated and deactivated, the following applies to $\boldsymbol{\nu}_{\mathrm{d},2}$:

$$\boldsymbol{\nu}_{\mathrm{d},2} = \begin{cases} (0,0,0,0,0,-0.5)^{\mathrm{T}}, & \text{gel supply activated} \\ (0,0,0,0,0,0)^{\mathrm{T}}, & \text{gel supply deactivated.} \end{cases} \tag{5.6}$$

Since the calculation in Eq. (5.5) is performed with respect to the end effector coordinate system (see Figure 5.10A), $\boldsymbol{\nu}_{\mathrm{d},2}$ represents a pure rotation with a rotational velocity of $-0.5\ \frac{\circ}{\mathrm{s}}$ around the $^{ee}z-$axis of the end effector in case of a desired gel transport. This corresponds to the movement of the seventh joint in negative direction. In contrast, the position of the tube with respect to the lever remains constant if the gel feed is stopped. Thus, the seventh joint is not moved.
The joint velocities $\dot{\mathbf{q}}_{\mathrm{mc,p}}$ required for the desired movement, calculated according to Eq. (5.5), are transformed into joint positions $\mathbf{q}_{\mathrm{mc,p}}$ by Eq. (4.14). These are commanded to the robot, which is controlled in joint impedance mode with a stiffness of 500 $\frac{\mathrm{Nm}}{\mathrm{rad}}$ and a damping ratio of 0.9, ensuring compliance while moving.

5.2.3 Validation Experiments

Automatic US gel supply is considered as an additional feature, not a core application of the robotic US system developed within this thesis. Thus, two phantom experiments are presented to demonstrate the functionality. In addition to performing a vessel scan, another potential use case for a fully automated long-term examination is also described. The experimental setup is shown in Figure 5.9. During the execution of experiments, the 2D US data and the measured joint positions provided by the robot interface are stored.

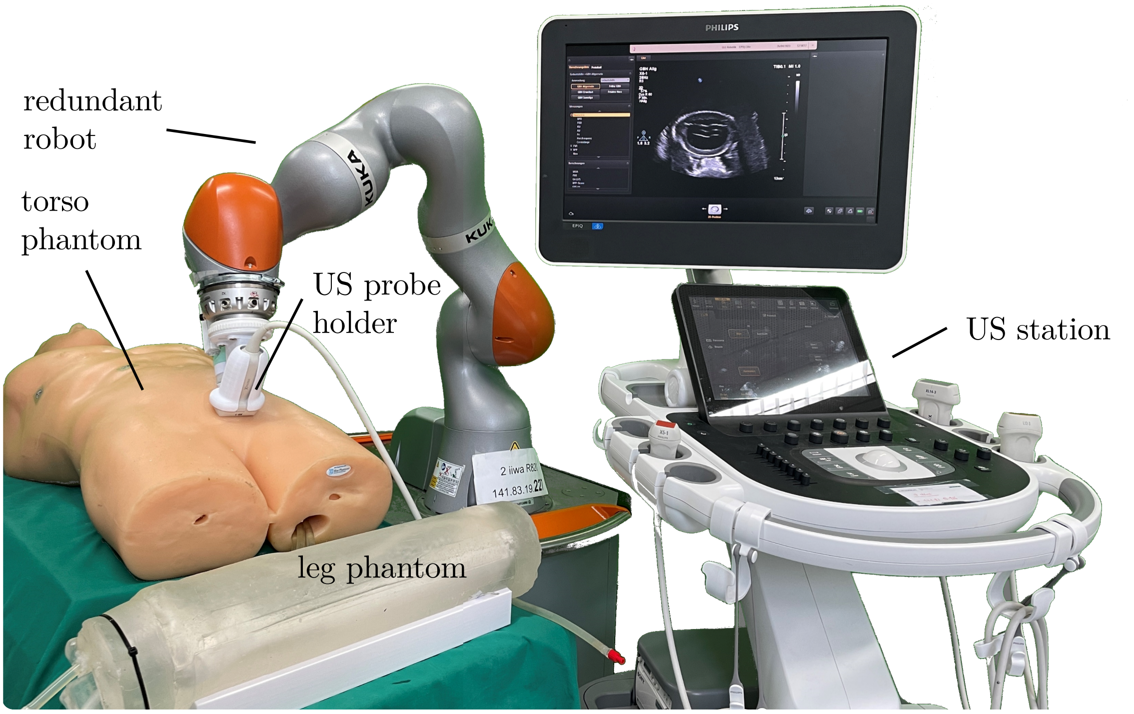

Figure 5.9: Experimental setup, consisting of a robotic manipulator with the gel dispenser, US station, a torso phantom, and a leg phantom.

Vessel Scan

The first experiment represents a linear scan of a vessel inside the leg phantom shown in Figure 5.10A. The US probe was manually positioned on the dry phantom. Then it was moved in the z direction of the probe for 4 mm, ensuring complete probe contact with the surface during the scanning process. The probe was then moved at a velocity of 0.01 $\frac{\mathrm{m}}{\mathrm{s}}$ on a straight path along five equally distributed way points for a distance of 25 cm, whereby the orientation of the probe had to remain constant. The direction of the translational part of $\boldsymbol{\nu}_{\mathrm{d},1}$ was calculated by transforming the difference between the current probe position and the next path point to the end effector frame. As soon as the second path point was reached, the supply of US gel was started. After arriving at the third path point, the gel supply was stopped again. Finally, the robot motion stopped when the last point of the path was reached. This experiment was repeated for five times. Since gel application caused the seventh joint to move slightly into the tube, the initial position of the seventh joint was adjusted accordingly during the repetitions.

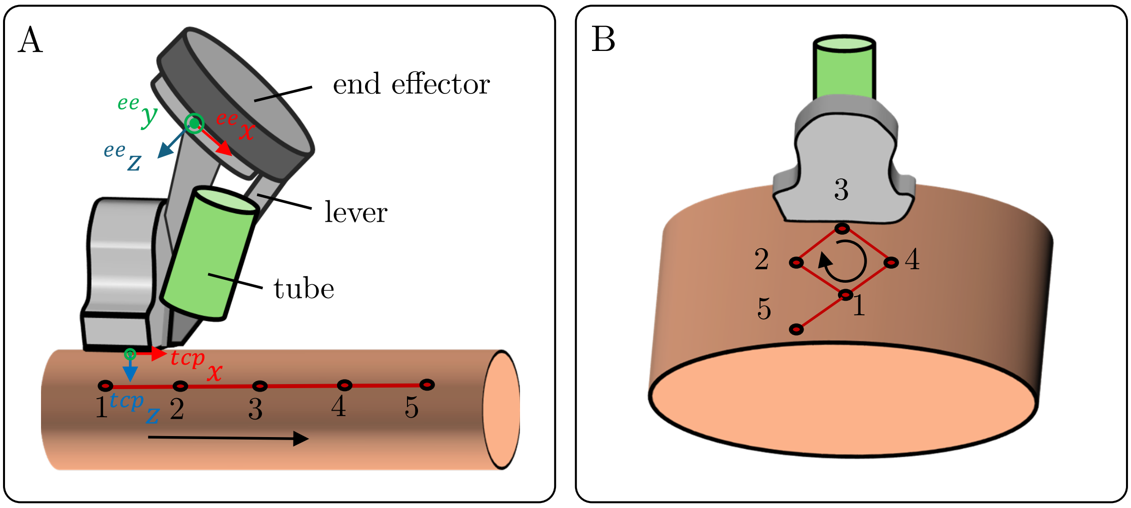

Figure 5.10: Validation experiments. **(A)**: Vessel Scan. **(B)**: Long-term US Examination.

Robotic long-term US Examination

As a second experiment, a robot guided long-term US examination on a torso phantom (see Figure 5.9A) was performed, which represents a suprapubic scan of the prostate and bladder. First, US gel was applied manually, and the probe was positioned accordingly at the target area. Again, it was moved in the z direction of the probe for 4 mm, ensuring complete probe contact with the surface. Then, a rectangular path consisting of four points was repeatedly followed, as shown in Figure 5.10B. The amount of gel between the probe and the phantom surface decreases over time, resulting in a degrading US image. This image quality degradation was detected by determining the mean value of all pixels of all US images of each path round. If this value was lower than 80 % of the value that had been present at the beginning of the experiment, i.e., after the first path round, the US gel feed was activated. This resulted in a movement of the seventh joint by a step of 2°, so that the lever was pressed into the tube and gel was supplied. Since the gel outflow is placed slightly in front of the probe, the probe was moved to a fifth path point (see Figure 5.10B) during gel delivery and lifted 4 mm from the body, which allowed the gel to better reach the observed body region. The experiment was stopped when the total examination time of 45 minutes was reached.

5.2.4 Results

Vessel Scan

As described in section 5.2.2, two tasks with different priorities must be performed simultaneously. This means that the second priority motion of the seventh joint $\boldsymbol{\nu}_{\mathrm{d},2}$ to supply US gel must not influence the first priority movement $\boldsymbol{\nu}_{\mathrm{d},1}$ of the probe to follow the path. This is confirmed by examining the error between the desired and the current probe pose while performing the scan. The norm of the translational error in the ${}^{probe}xy$ plane between the probe position and the path, which is shown in blue Figure 5.11, was always below 3 mm with an average error of 0.8 mm over the whole path. The average angular error of the ${}^{probe}z-$axis was 0.49° and is visualized in green in Figure 5.11. Moreover, the movement of the seventh joint is shown on the second axis on the right. When the second path point P_2 at 6.25 cm was reached, the gel supply was activated, which resulted in a movement of the seventh joint in negative direction. After arriving at the third path point P_3 at 12.5 cm, the supply was stopped again, which resulted in a constant position of the seventh joint. Thus, it can be shown that the two movements could be performed in parallel without causing mutual influence.

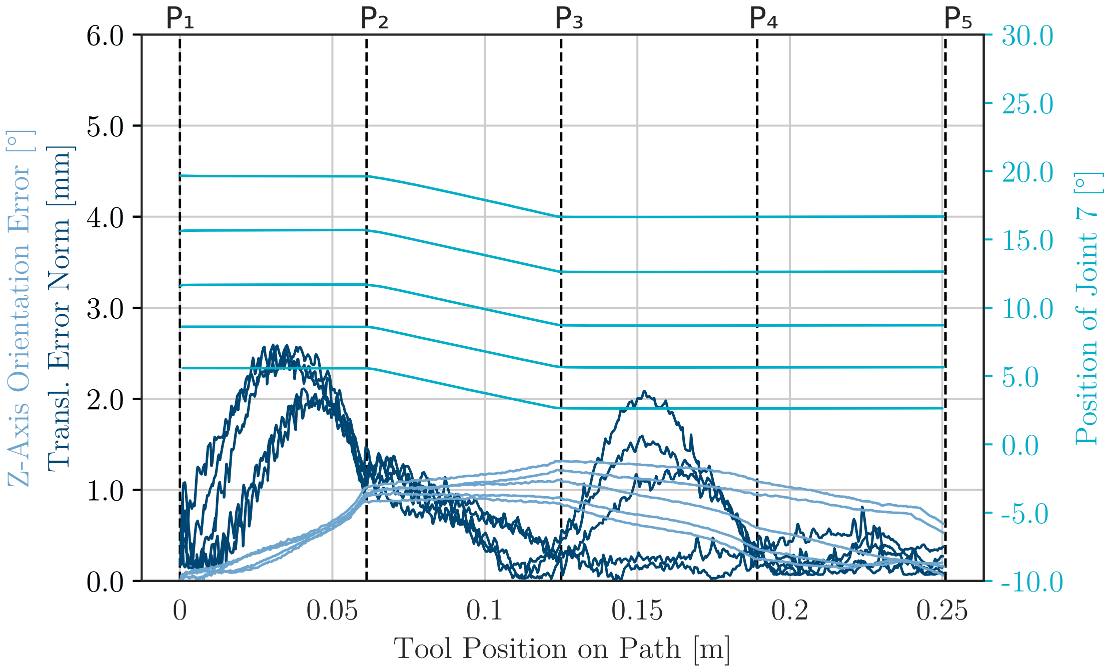

Figure 5.11: Translational error to path in xy plane (dark blue, left axis), $z-$axis angular error (light blue, left axis) and position of seventh joint (turquoise, right axis) of the five vessel scans performed.

The small errors are caused by the compliance of the robot in impedance control mode. Due to unevenness on the surface and friction effects between the probe and the phantom, there may be a slight deviation from the target path. It is interesting to note that the error increased slightly as soon as the gel was applied and distributed. This is probably due to the fact that the friction became lower and the probe could be pushed more easily into one side due to the curvature of the phantom. To show the influence of gel supply on image quality, the mean value of US images acquired during the scan is presented in Figure 5.12. It can be seen that the mean values increased sharply once the gel had been applied and distributed. As an example, US images at the path positions of 11 cm, 13 cm, 15 cm, and 17 cm are also shown in Figure 5.12, where the increase in image quality can be clearly seen.

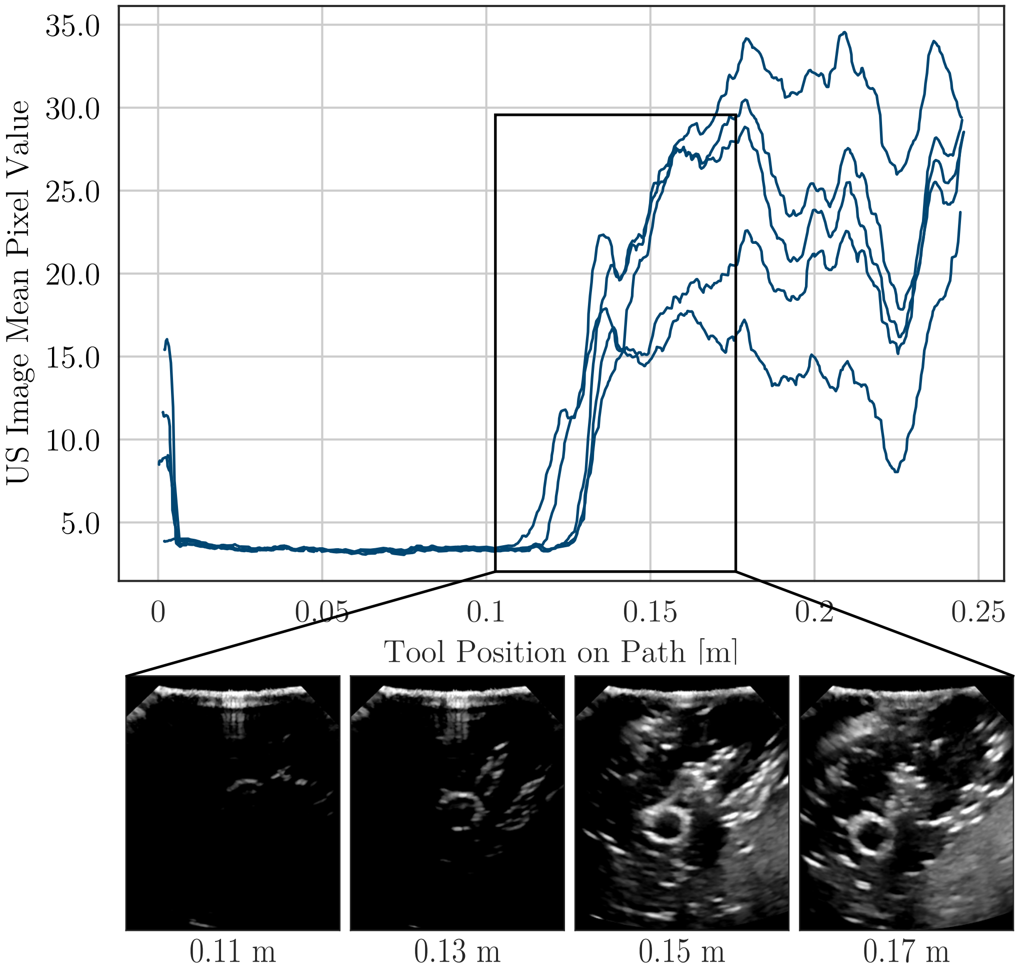

Figure 5.12: Mean of the pixel values of the US images of the five vessel scans performed, plotted as a function of the distance of the probe from the start position. In addition, four exemplary US images at the positions 0.11 m, 0.13 m, 0.15 m, and 0.17 m are shown.

Robotic long-term US Examination

This second experiment was performed to demonstrate the possibility of long-term robotic US investigations without human intervention. Figure 5.13 shows the average of the pixel values of the US images acquired during one path round. It can be seen that after approximately 17 minutes, the amount of gel was reduced to such an extent that the image quality decreased. As soon as the mean pixel value of a path round was below the threshold of 20.7, representing 80 % of the value at the beginning of the experiment, the supply of US gel started and the image quality increased again as the gel was distributed. This was repeated shortly thereafter at the 23 minute time point. The reason for this is that the amount of gel supplied the first time was not large enough. Afterwards, the image quality remained at a constantly high level for about 15 minutes until gel was added for a third time. The experiment clearly shows the potential for prolonging robotic US examinations since without an automated gel supply, the examination would have been interrupted after 17 minutes.

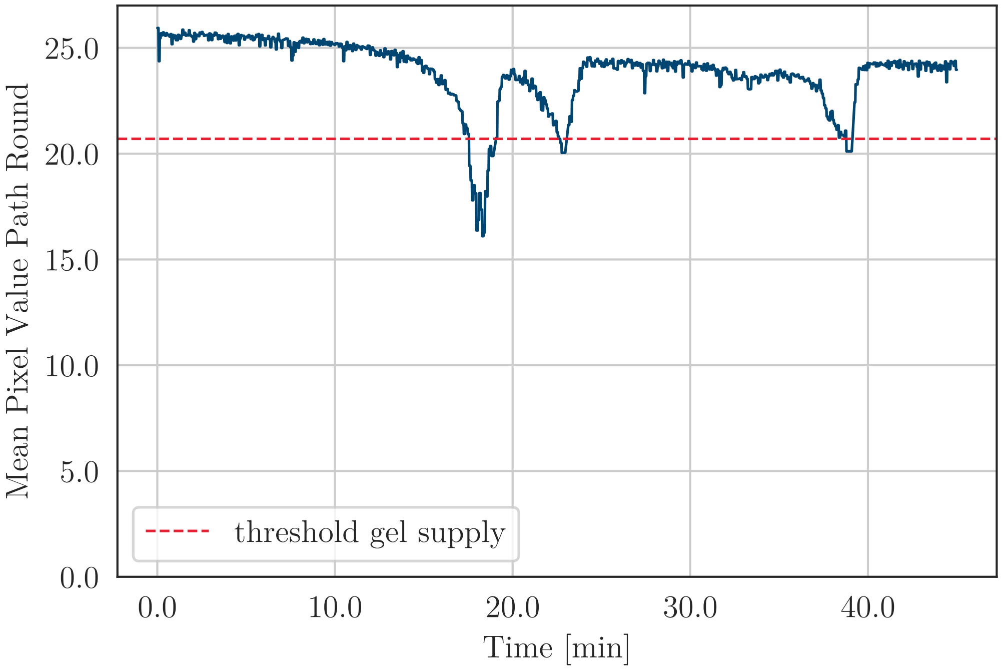

Figure 5.13: Mean of the path round pixel values of the US images of the long-term US examination.

5.2.5 Discussion and Conclusion

Robot guided US is becoming more interesting for a variety of clinical applications. So far, US gel, which is necessary to obtain high-quality images, has been applied manually by clinical staff. The goal of this approach was to automatically supply US gel by appropriately controlling the nullspace of a seven DoF robot in combination with a passive mechanism. This enabled US gel to be dispensed from a tube while the probe is moving. The results showed that long, fully automated US examinations can be made possible. For example, this might be of interest for possible applications in radiation therapy, where no staff can intervene during irradiation. Although the method showed promising results, some challenges remain to be addressed. First, the lever, which serves as a push mechanism, must be positioned and fixed manually before the examination, which is a difficulty in a realistic scenario. It would also be possible to select a fixed position for the lever, but this would result in a limited range of motion, since one degree of freedom less is available for positioning of the probe. Singularities represent another challenge. As described in Eq. (5.5), the pseudoinverse of $\mathbf{J}_2(\mathbf{I} - \mathbf{J}_1^\dagger \mathbf{J}_1)$ must be calculated. This matrix becomes singular if the second prioritized task cannot be performed without affecting the primary task. Thus, the problems that arise from the kinematic singularities, i.e. high joint velocities and oscillations, arise. To overcome this problem, the damped least-squares inverse can be used as described in [107]. The secondary task tracking will then be less accurate, but this is not a problem in the presented application as long as the rotation is in the direction of the lever. In addition, the mechanical design of the gel dispenser, especially the gel nozzle, could be improved. The design should be made in such a way that the probe should not have to be lifted to apply and distribute the US gel in a quasi-static task. Another challenge is the lack of control over the volume of gel dispensed. Each activation of the push mechanism may release a different amount of gel, which can result in uneven or unsufficient coverage. Integrating a dosage-regulated mechanism could provide more consistent and reliable gel application.

6 OPTIMIZATION OF CONTACT WRENCH ESTIMATION[5]

Precise and robust contact wrench measurements at the end effector of the robot are required to ensure that the US probe is guided with a specific contact force. This ensures patient safety and reproducibility of the examination. A higher accuracy of the determined wrench leads to enhanced overall sensitivity of the robot, and therefore allows for more complex applications. Furthermore, errors in the computational model can lead to dangerous and harmful situations for patients. The aim of this chapter is to improve the accuracy of the robot's wrench estimation model without using external sensors (Figure 6.1).

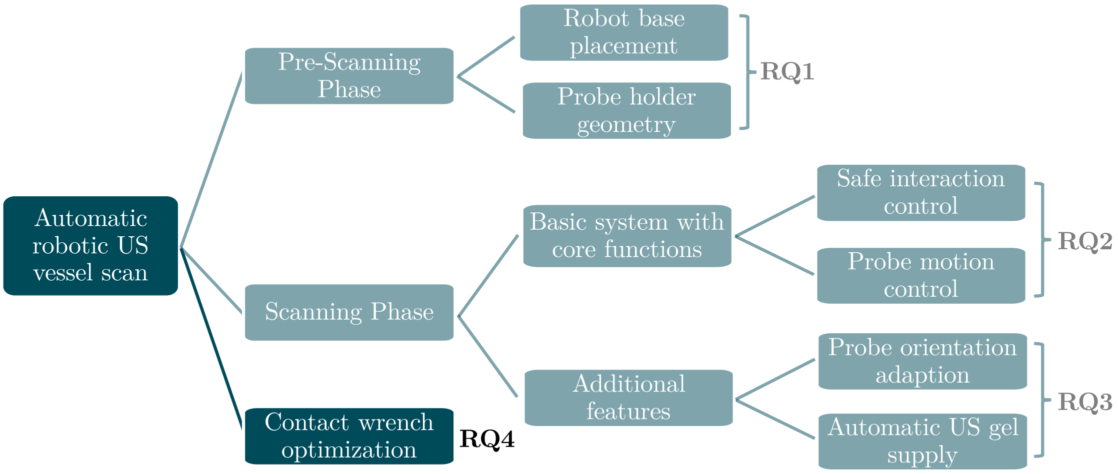

Figure 6.1: Structure of the thesis. The essential topics required for an automatic robotic US examination are addressed in individual chapters, with the content of this chapter highlighted in dark blue.

This is done by focusing on a slow robot movement, i.e. a quasi-static case, as would be used in an US examination. The following research question is to be answered:

> **Research Question 4**
> How can the accuracy of the robot's wrench estimation as well as the robustness be increased in quasi-static scenarios?

---

[5] Parts of this chapter have been published in [108].

In the following, a learning approach is proposed to train the dependencies between joint torques, which are measured in each of the robot's axes, and the end effector contact wrenches. Thus, the accuracy and robustness of the wrench estimation model can be increased. Furthermore, it is proven that the approach could be also transferred to another robot with reasonable prediction accuracy and without the need of acquiring new robot specific training data.

6.1 Related Work - Learning Approaches for Contact Wrench Estimation

Integrated joint torque sensors provide crucial functionalities for safe human-robot-interactions. The end effector wrench can be estimated based on the robot's mechanical model provided by the manufacturer using the torque sensors in the joints (see Eq. (2.8)). However, the computational models use the Jacobian, which loses full-rank at singularities, causing the wrench estimation to fail. In literature, various methods have been proposed to use machine learning in the context of robot control and contact force estimation. Artificial neural networks (ANNs) show impressive capabilities in solving direct [109] and inverse kinematics [110] as well as in dynamic control of redundant manipulators [111]–[113]. Earlier research addressed the calibration of force/torque sensors for serial robotic manipulators, mostly focusing on optimizing linear relations between joint torques and dynamic parameters known as the Inverse Dynamic Identification Model (IDIM) [114]–[116]. Learning approaches to optimize the IDIM were presented in [117]–[119]. In [120], neural networks are used to map measured signals and resulting forces, to calibrate an external force/torque sensor mounted to an end effector. Although the authors show accurate results and provide time-saving routines, unfortunately, instabilities near singularities still exist, or additional external sensors are required. Smith et al. showed interesting results by using a neural-network-based approach to determine contact forces for haptic devices [121]. Unfortunately, the authors have to use biased ground truth data and, therefore, it remains unclear how this affects the calibration accuracy. A method using deep learning for reducing errors in identification of dynamic parameters of a 6-DoF robot is presented in [122]. Moreover, [123] includes physical laws of the system (in the form of the Euler-Lagrange equation) into deep neural network architectures. Thus, more accurate models can be obtained whilst ensuring physical plausibility. In [124], the dynamic behavior of a 7-DoF force sensing robot, focusing on low-velocity, small-scale, and locally isotropic motion, which amplifies friction, joint elasticity, and hysteresis effects beyond the capabilities of standard modeling and regression techniques is investigated. A hybrid model architecture that combines a rigid body dynamics model identified through parametric regression with time-series neural networks and a joint-wise rotational history encoding to capture dynamic hysteresis is proposed. An accurate torque estimation could be achieved even under complex friction and elasticity effects, whereby the explainability by the physical predecessor model was maintained [124]. Another hybrid approach, combining a bootstrap aggregating algorithm with a long short-term memory network, is proposed in [125] to enhance residual prediction accuracy for inverse dynamics models in industrial robots.

However, the papers do not relate to the external force estimation at the end effector. This is done in [126], where deep learning is used to estimate end effector forces as well as joint torques of a 7-DoF robotic manipulator. Even though promising results are shown, a validation of the estimation of end effector forces and moments on a real robot is missing. The use of neural networks for calibrating the robotic system provides several advantages. The system is capable of learning unique mechanical characteristics of the manipulator, and the robot can therefore be calibrated in a highly specialized way. Furthermore, critical arm positions and singularities can be directly learned from the network as training points. Using a sufficient amount of diverse input data, these points can be uniquely identified and integrated into the model, resulting in a more robust calibration.

6.2 Acquisition of Datasets

The aim of this approach is to determine contact wrenches at the end effector. It is investigated whether the contact wrench can be predicted from corresponding joint positions as well as joint torque data. Different datasets, both simulated and real, have been acquired to train and evaluate neural network models. An LBR iiwa 7 robot was used for the experiments and data acquisition. To further validate the generalization capability, the method was also tested on an LBR iiwa 14.

6.2.1 Simulated Training Data

A large simulated dataset is generated, varying the applied forces, the distances of the end effector to the force application point as well as the applied external torques for randomized joint configurations. Thus, randomized end effector contact wrenches are generated and the corresponding joint torques for an ideally static case can be calculated. In the considered scenario, forces between -20 and 20 N are applied at a point with a distance between 0 and 0.15 m to the end effector. The range results from the intended application to measure the force acting on an US probe attached to the end effector of a robot. Moreover, an additional external torque between -2 and 2 Nm is applied at the end effector. The steps of generating the simulated training data are explained as follows: Let ${}^{\mathrm{ee}}\mathbf{w} \in \mathbb{R}^6$ be the wrench at the end effector consisting of contact forces ${}^{\mathrm{ee}}\mathbf{f} \in \mathbb{R}^3$ and contact moments ${}^{\mathrm{ee}}\mathbf{m} \in \mathbb{R}^3$ (see Figure 6.2A). For each data point, a valid joint configuration, a contact force ${}^{\mathrm{ee}}\mathbf{f} \in \mathbb{R}^3$ and distance $\mathbf{r}_{\mathrm{fap}}$ to the force application point as well as an additional external contact torque ${}^{\mathrm{ee}}\mathbf{m}_{\mathrm{ext}}$ are chosen randomly. The resulting moment ${}^{\mathrm{ee}}\mathbf{m}$ applied at the end effector can be calculated by

$$ {}^{\mathrm{ee}}\mathbf{m} = \mathbf{r}_{\mathrm{fap}} \times {}^{\mathrm{ee}}\mathbf{f} \; + \; {}^{\mathrm{ee}}\mathbf{m}_{\mathrm{ext}}. \tag{6.1} $$

By using the transposed geometric Jacobian matrix $\mathbf{J}(\mathbf{q})$ of the end effector, the corresponding external joint torques according to Eq. (2.7) can be calculated, considering an ideally static case. The simulated dataset consisting of 3,000,000 data points is named $dataset_{train,sim}$.

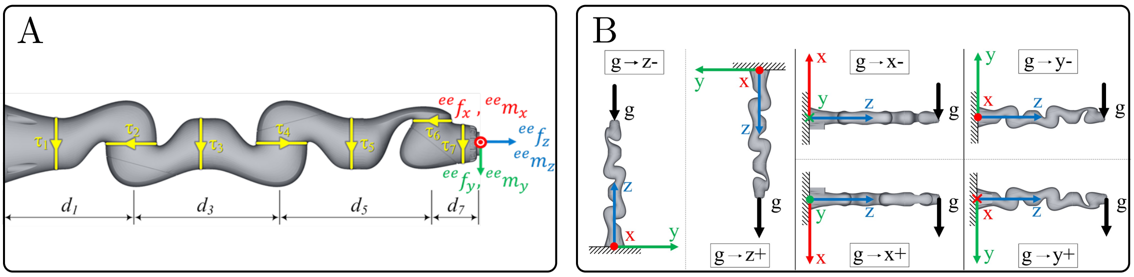

Figure 6.2: **(A)** The end effector contact wrenches ${}^{ee}f_x$, ${}^{ee}f_y$ and ${}^{ee}f_z$ are related to the measured joint torques $\tau_1, ..., \tau_7$. **(B)** The robot was mounted in six different base orientations to record the training data with a homogeneous distribution of gravity vector directions.

6.2.2 Real Training Data

The aim of this work is to precisely determine corresponding contact wrenches at the end effector from given joint positions and torque data. Contact wrenches at the end effector can result from various impacts: by external forces such as pushing or pulling by hand, or while the robot actively pushes against an object with its tool attached to the end effector. From a mechanical point of view, the resulting wrenches are the same for both cases and can be measured via the joint torques. In this study, the wrenches are simulated by mounting different masses on the end effector. Gravity produces an equivalent force, which pulls the mass towards the ground. Obviously, this static force will always point in the same direction in the world coordinate system, but for varying robot positions it will create different contact forces in end effector coordinates. With only one direction in world coordinates, not all contact forces can be represented. Hence, six different base rotations were used to solve this problem. The robot was therefore mounted in different orientations, shown in Figure 6.2B, resulting in a more homogeneous representation of the contact forces in all directions. To determine an exact ground truth for the end effector forces, specially manufactured calibration weights were used. The weights are built from symmetric metallic discs. By appropriately stacking combinations of these calibration weights on a metallic rod, which was attached to the robots tool flange along the z-axis, it was possible to generate 10 equidistantly distributed end effector forces in 2 N steps in the target range from 0-20 N. The precise total weights resulting from the combinations of stacked calibration weights are $m_j \in \{0, 202, 391, 616, 818, 995, 1199, 1401, 1603, 1808, 2002\}$ g , for $j \in \{1, \dots, 11\}$. Examples of how the calibration weights are stacked on the metallic rod to generate specific end effector forces are shown in Figure 6.3. For each mass, 5,000 measurements in newly randomly generated poses were acquired. Thereby, sensor hysteresis is part of the data, as many different poses with different combinations of approach directions are approached for each joint. In total, a dataset of randomized 330,000 data points with varying base rotations and calibration weights was acquired. The force application point is chosen as the resulting center of mass of the metallic rod with the appropriately stacked calibration weights. The centers of mass of the corresponding combinations of the metallic rod and the calibration weights are $com_j \in \{0, 2.5, 25.5, 28.2, 30.9, 33.4, 38.2, 40.7, 43.2, 42.3, 50\}$ mm, for $j \in \{1, \dots, 11\}$. These were determined from an accordingly created CAD

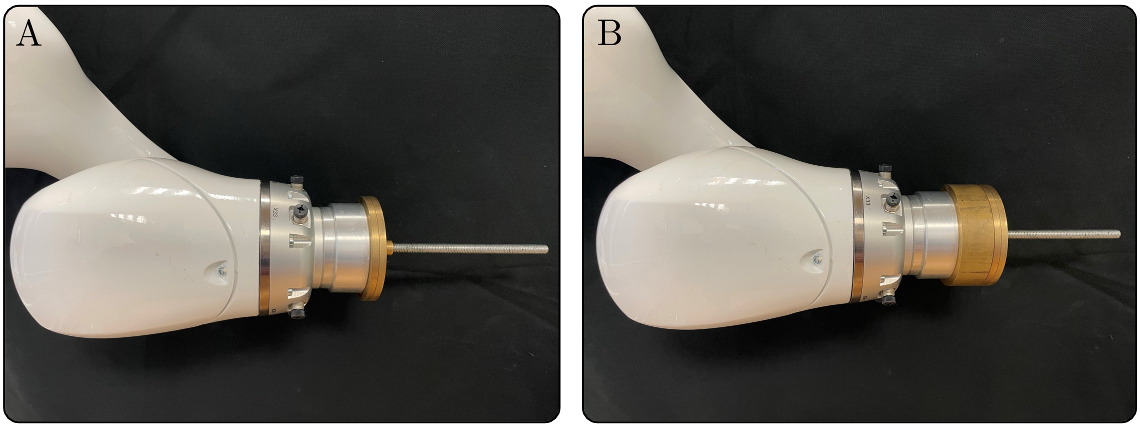

Figure 6.3: Calibration weights were stacked on a metallic rod attached to the end effector of the robot to generate 10 equidistantly distributed end effector forces in the target range from 0-20 N. Examples of appropriately stacked calibration weights to generate an end effector force of 8 N **(A)** and 18 N **(B)** are shown.

Table 6.1: To calculate the six base transformations $^{-1}\mathbf{T}_{0,\mathrm{i}}$ using Eq. (6.3) as shown in Figure 6.2B, different combinations of Tait-Bryan angles are used.

i	Base rotation	Ψ [°]	Θ [°]	Φ [°]
1	g → z−	0	0	0
2	g → z+	0	0	180
3	g → x−	180	−90	0
4	g → x+	0	90	0
5	g → y−	90	0	90
6	g → y+	−90	0	−90

model in SolidWorks, where the different materials as well as their densities were taken into account.

The exact contact forces for the ground truth can be determined as follows: For a serial manipulator, the position and orientation of the end effector can be calculated by coordinate transformations from the base along the joints by:

$$^{0}\mathbf{T}_{7} = {}^{0}\mathbf{T}_{1}{}^{1}\mathbf{T}_{2}{}^{2}\mathbf{T}_{3}\dots{}^{6}\mathbf{T}_{7}\,. \tag{6.2}$$

Using Eq. (6.2), the transformation $^{0}\mathbf{T}_{\mathrm{i}}$, $i \in \{1,\dots,7\}$ to every joint i can be computed as well.
Let $^{-1}\mathbf{T}_{0,\mathrm{i}}$ be the robot base transformation defined by:

$$^{-1}\mathbf{T}_{0,\mathrm{i}} = \mathcal{R}_{\mathrm{z},\Psi_\mathrm{i}}\mathcal{R}_{\mathrm{y},\Theta_\mathrm{i}}\mathcal{R}_{\mathrm{x},\Phi_\mathrm{i}}\,, \tag{6.3}$$

using homogeneous rotations with six different combinations of the three Tait-Bryan angles Ψ_i, Θ_i and Φ_i, $i \in \{1,\dots,6\}$, denoted in Table 6.1.
Let $g_0 = 9.806\ \frac{\mathrm{m}}{\mathrm{s}^2}$ be the gravity constant. The acceleration vector due to gravity is:

$$\mathbf{g} = \begin{pmatrix} 0 & 0 & -g_0 \end{pmatrix}^{\mathrm{T}}. \tag{6.4}$$

Then the forces induced by the calibration masses $\mathrm{m_j}$ acting in the robot base coordinate system (b) can be described by:

$$^{\mathrm{b}}\mathbf{f}_{\mathrm{i,j}} = {}^{-1}\mathbf{T}_{0,\mathrm{i}} \begin{pmatrix} \mathbf{g} \cdot m_{\mathrm{j}} \\ 1 \end{pmatrix}, \tag{6.5}$$

for $i \in \{1, \ldots, 6\}$ and $j \in \{1, \ldots, 11\}$. Now let $^0\mathbf{R}_7$ be the end effector rotation as upper 3×3 rotational matrix based on the homogeneous transformation from Eq. (6.2), i.e.:

$$^0\mathbf{T}_7 = \begin{pmatrix} ^0\mathbf{R}_7 & \mathrm{t} \\ 0 & 1 \end{pmatrix}, \tag{6.6}$$

with vector t as translational part. Let

$$^0\mathcal{R}_7 = \begin{pmatrix} ^0\mathbf{R}_7 & 0 \\ 0 & 1 \end{pmatrix}, \tag{6.7}$$

denote as the end effector rotation as homogeneous transformation with zero translation in the robot base coordinate frame. Then the forces acting in the end effector coordinate system (ee) can be described by

$$^{\mathrm{ee}}\mathbf{f}_{\mathrm{i,j,n}} = {}^0\mathcal{R}_{7_{\mathrm{n}}}^{-1} \cdot {}^{\mathrm{b}}\mathbf{f}_{\mathrm{i,j}}, \tag{6.8}$$

for $i \in \{1, \ldots, 6\}$ base rotations, $j \in \{1, \ldots, 11\}$ calibration masses and $n \in \{1, \ldots, 5000\}$ measurements.

The forces are not acting directly in the end effector coordinate frame, but in the center of mass of the metallic rod with the appropriately stacked calibration weights. Thus, a moment $^{ee}\mathbf{m}$ is generated in the end effector, which can be calculated by

$$^{\mathrm{ee}}\mathbf{m}_{\mathrm{i,j,n}} = \mathbf{r}_{\,\mathrm{com,j,n}} \times^{\mathrm{ee}} \mathbf{f}_{\mathrm{i,j,n}}. \tag{6.9}$$

For every end effector wrench $^{\mathrm{ee}}\mathbf{w}_{\mathrm{i,j,n}} = (^{\mathrm{ee}}\mathbf{f}_{\mathrm{i,j,n}} \quad ^{\mathrm{ee}}\mathbf{m}_{\mathrm{i,j,n}})^{\mathrm{T}}$, the corresponding joint positions $\mathbf{q}_{\mathrm{i,j,n}}$ and joint torques $\boldsymbol{\tau}_{\mathrm{i,j,n}}$ are measured using the robot control software KUKA Sunrise (KUKA, Augsburg, Germany) with the Fast Research Interface (FRI) v1.13 [127]. However, the measured torques include the self-weight of the robot links. The resulting torques depend on the joint positions and, more importantly, on the base orientation and the inherent direction of gravity. To decouple the data, only the torques generated by the specific calibration weights are used for training the neural network. To identify these isolated torques, the gravity torques without mounted calibration weight $\boldsymbol{\tau}_0$ have to be estimated first (see Section 6.3.1) and subtracted from the measured joint torques with mounted calibration weight $\boldsymbol{\tau}_{\mathrm{j}}(m_{\mathrm{j}})$. The torques resulting only from the additional weight can therefore be determined by

$$\Delta\boldsymbol{\tau}_{\mathrm{j}} = \boldsymbol{\tau}_{\mathrm{j}} - \boldsymbol{\tau}_0, \tag{6.10}$$

for $j \in \{1, \ldots, 11\}$ calibration weights. To have a database for the estimation of the gravity torques as well (see Section 6.3.1), two discrete measurements were performed at each of the randomized positions. First, the joint torques without mounted calibration weight $\boldsymbol{\tau}_0(\mathrm{m}_0)$ were recorded. In a second measurement, the torques with mounted calibration $\boldsymbol{\tau}_{\mathrm{j}}(\mathrm{m_j})$ were recorded at the very same positions. Collecting the training data required approximately eleven weeks of continuous operation of the robot. This large training dataset consisting of 330,000 randomized positions is named $dataset_{train,real}$.

Table 6.2: Base orientations of directional generalization $dataset_{gen,dir}$.

data points	Ψ [°]	Θ [°]	Φ [°]	load [kg]
1500	0.0	0.2	0.1	1.0
500	0.0	0.0	31.1	1.0
1500	0.5	29.1	0.2	1.0
1500	0.0	27.8	−14.6	1.0
1500	0.0	−43.3	0.7	1.0
1500	0.0	−31.7	39.4	1.0

6.2.3 Real Generalization Testing Data

As described in Section 6.2.2, six different base orientations are used to generate combinations of contact forces. In a realistic scenario, however, these end effector forces can occur from every direction. Thus, the network must be capable of generalizing intra-directionally. To analyze the directional generalization performance, an additional test dataset was acquired using five varying, unleveled base orientations. Therefore, the manipulator was mounted on a hexapod, as shown in Figure 6.4. This dataset is only used for evaluating the performance of the proposed models (see Figure 6.6 and Figure 6.7 in Chapter 6.4.2) - it is not involved in any form during the training process. Due to the lack of absolute precision of the hexapod, the actually reached Tait-Bryan angles, for calculating the base orientation (see Section 6.2.3), were measured using an inclinometer with an accuracy of 0.1°.

Figure 6.4: The LBR iiwa 7 was mounted on a hexapod to acquire the test data ($dataset_{gen,dir}$), to evaluate the intra-directional generalization performance.

A calibration mass of 1.0 kg (10 N) was used. The first dataset was acquired with a known base orientation (zero rotation) as reference. Afterwards, the measurements for each orientation were acquired. The dataset is named $dataset_{gen,dir}$.

6.2.4 Real Transfer Testing Data

Generating a large robot specific training dataset as described in Section 6.2.2 is quite time-consuming. To examine the transferability of the presented approach to another robot type, an additional testing dataset was acquired. This dataset is only used for evaluation purposes (see Figure 6.8 in Section 6.4.4), it is not involved during the training process of the neural networks. This transfer testing dataset was acquired with the LBR iiwa 14. This robot has similar geometric dimensions and thus is well suited for a transfer experiment. Due to the increased time required as well as the much larger self-weight of this robot, which does not allow mounting on our lab wall or lab ceiling, only a dataset was generated in the ground base orientation $g \rightarrow z-$ (see Figure 6.2B). For each calibration weight (0.2-20 N), 500 randomized positions were recorded in the same way as described in Section 6.2.2. This results in a dataset of 5,000 positions, which is named $dataset_{transf}$. The gravity torques $\boldsymbol{\tau}_0(\mathrm{m}_0)$ of the LBR iiwa 14 are greater than for the smaller LBR iiwa 7 since the robot links are bigger and heavier. Thus, the gravity compensation parameters according to Section 6.3.1 have to be redetermined for the LBR iiwa 14, which is done in the same way as described in Section 6.4.1 using the $dataset_{transf}$.

6.3 Model Learning

The aim of the presented method is to learn the relationship between the external joint torques measured in the individual joints of the robot and the contact wrench at the end effector. Two models are required for this purpose. The gravity compensation model (see Section 6.3.1) first determines the static gravitational joint torques depending on the robot configuration. The difference between the measured torques in the joints and the weight forces then provides the external joint torques, which are used to train a neural network to estimate the wrench (see Section 6.3.2).

6.3.1 Gravity Torque Compensation Model

For training of the neural network, the isolated torques $\Delta\boldsymbol{\tau}_\mathrm{j}$ generated by the specific calibration weight are used. To calculate them according to Eq. (6.10), the joint torques without mounted calibration weight $\boldsymbol{\tau}_0$ have to be estimated first. In a static case, these torques $\boldsymbol{\tau}_0$ depend on the base orientation, the joint configuration and the weight of the robot links. A simple data-driven approach based on linear regression was used, which can be used without any knowledge of the masses as well as the centers of gravity of the robot links. [128] showed that the joint angle and joint driving torque can accurately regress the relationship between barycentric coordinates of the link and the mass of the connecting rod in the cartesian coordinate system. But instead of identifying the masses and centers of gravity of the robot links separately, linear regression was used to directly calculate parameters w_j, which

can be used to approximate the acting gravity torques due to the following joint link masses. The approach is based on the following mechanical relation:
For a 7-DOF manipulator, the relationship between a joint torque $\boldsymbol{\tau}_{\mathrm{j}}$ and the gravity forces $\mathbf{g}_{\mathrm{i}}$ acting in the centers of the following links can be shown to be:

$$\boldsymbol{\tau}_{\mathrm{j}} = \sum_{i=j}^{7} \mathbf{J}_{\mathrm{m,i}}^{\mathrm{T}} \cdot \mathbf{g}_{\mathrm{i}}, \tag{6.11}$$

where

$$\begin{aligned} \mathbf{J}_{\mathrm{m,i}}^{\mathrm{T}} &= (\mathbf{z}_{\mathrm{j}} \times \mathbf{r}_{\mathrm{com,i}})^{\mathrm{T}} \\ &= \begin{pmatrix} \mathbf{J}_{\mathrm{m,x,i}}^{\mathrm{T}} \\ \mathbf{J}_{\mathrm{m,y,i}}^{\mathrm{T}} \\ \mathbf{J}_{\mathrm{m,z,i}}^{\mathrm{T}} \end{pmatrix}^{\mathrm{T}} \\ &= \begin{pmatrix} z_{\mathrm{j,y}} r_{\mathrm{com,i,z}} - z_{\mathrm{j,z}} r_{\mathrm{com,i,y}} \\ z_{\mathrm{j,x}} r_{\mathrm{com,i,z}} - z_{\mathrm{j,z}} r_{\mathrm{com,i,x}} \\ z_{\mathrm{j,x}} r_{\mathrm{com,i,y}} - z_{\mathrm{j,y}} r_{\mathrm{com,i,x}} \end{pmatrix}^{\mathrm{T}}, \end{aligned} \tag{6.12}$$

is the linear velocity part of the transposed Jacobian for the center of mass $\mathbf{r}_{\mathrm{com,i}}$ of link i. Since the calculations are done with respect to the world coordinate system, the force $\mathbf{g}_{\mathrm{i}}$, acting in the center of mass of link i due to the gravity of m_{i}, is described by:

$$\mathbf{g}_{\mathrm{i}} = \begin{pmatrix} 0 \\ 0 \\ -m_{\mathrm{i}} g_0 \end{pmatrix}, \tag{6.13}$$

where m_{i} is the mass of link i and g_0 is the gravity constant.

Taking into account all the joints of the manipulator, the following equation system represents the relationship from Eq. (6.11):

$$\begin{pmatrix} \tau_1 \\ \vdots \\ \tau_7 \end{pmatrix} = \begin{pmatrix} \mathbf{J}_{\mathrm{m,1}}^{\mathrm{T}} & \cdots & \mathbf{J}_{\mathrm{m,7}}^{\mathrm{T}} \\ \vdots & \ddots & \vdots \\ 0 & 0 & \mathbf{J}_{\mathrm{m,7}}^{\mathrm{T}} \end{pmatrix} \begin{pmatrix} g_1 \\ \vdots \\ g_7 \end{pmatrix}. \tag{6.14}$$

Due to Eq. (6.13), the equation system Eq. (6.14) can be simplified since always only the third entry $\mathbf{J}_{\mathrm{m,z,i}}^{\mathrm{T}}$ of the transposed Jacobian in Eq. (6.12) of link i is multiplied by a value not equal to zero. Therefore, Eq. (6.14) can be written as

$$\begin{pmatrix} \tau_1 \\ \vdots \\ \tau_7 \end{pmatrix} = \begin{pmatrix} \mathbf{J}_{\mathrm{m,z,1}}^{\mathrm{T}} & \cdots & \mathbf{J}_{\mathrm{m,z,7}}^{\mathrm{T}} \\ \vdots & \ddots & \vdots \\ 0 & 0 & \mathbf{J}_{\mathrm{m,z,7}}^{\mathrm{T}} \end{pmatrix} \begin{pmatrix} -m_1 g_0 \\ \vdots \\ -m_7 g_0 \end{pmatrix}. \tag{6.15}$$

In order to calculate the gravity torques of a robot according to Eq. (6.15), the masses m_{i} as well as the centers of gravity $\mathbf{r}_{\mathrm{com,i}}$ of the links, which are used to calculate $\mathbf{J}_{\mathrm{m,z,i}}^{\mathrm{T}}$ according to Eq. (6.12), must be known. Since this is not the case without doing an identification of the robot, the distance $\mathbf{r}_{\mathrm{com,i}}$ to the center of mass of the link i in Eq. (6.12) is replaced by the distance $\mathbf{p}_{\mathrm{i+1}}$ to the following joint frames, which can be calculated from the geometric robot parameters for any joint configuration. This results in:

$$\begin{aligned}\tilde{\mathbf{J}}^{\mathrm{T}}_{\mathrm{m,i}} &= (\mathbf{z}_{\mathrm{j}} \times \mathbf{p}_{\mathrm{i+1}})^{\mathrm{T}} \\ &= \begin{pmatrix} \tilde{\mathbf{J}}^{\mathrm{T}}_{\mathrm{m,x,i}} \\ \tilde{\mathbf{J}}^{\mathrm{T}}_{\mathrm{m,y,i}} \\ \tilde{\mathbf{J}}^{\mathrm{T}}_{\mathrm{m,z,i}} \end{pmatrix}^{\mathrm{T}} .\end{aligned} \tag{6.16}$$

Moreover, the unknown link masses m_{i} in Eq. (6.15) are replaced by variables w_{i}. These variables w_{i} can be understood as imaginary point masses, which are directly located in the origin of the following joint frame. For example w_1 would be the imaginary mass of link 1, located in the origin of joint 2. Replacing m_{i} by w_{i} as well as replacing $\mathbf{J}^{\mathrm{T}}_{\mathrm{m,z,i}}$ by $\tilde{\mathbf{J}}^{\mathrm{T}}_{\mathrm{m,z,i}}$ in Eq. (6.15) results in:

$$\begin{pmatrix} \tilde{\tau}_1 \\ \vdots \\ \tilde{\tau}_7 \end{pmatrix} = \begin{pmatrix} \tilde{\mathbf{J}}^{\mathrm{T}}_{\mathrm{m,z,1}} & \cdots & \tilde{\mathbf{J}}^{\mathrm{T}}_{\mathrm{m,z,7}} \\ \vdots & \ddots & \vdots \\ 0 & 0 & \tilde{\mathbf{J}}^{\mathrm{T}}_{\mathrm{m,z,7}} \end{pmatrix} \begin{pmatrix} -w_1 g \\ \vdots \\ -w_7 g \end{pmatrix} . \tag{6.17}$$

This relationship describes the influence of the gravity force of the imaginary masses on the joint torques of the robot. The goal is to determine fitting imaginary masses w_{i}, located in the origin of the following joints, which have the same influence on the joint torques as the original masses m_{i} located in the center of mass $\mathbf{r}_{\mathrm{com,i}}$ of the link. Then, approximated gravity joint torques $\tilde{\tau}_{\mathrm{i}}$ can be calculated according to Eq. (6.17) for any joint configuration.

To determine w_{i}, the equation system in Eq. (6.17) must be solved. This can be done in the least-square sense using N measurements, where $N \gg 7$. For calculating the optimal linear regression solution $\mathbf{x} = (w_1, ..., w_7)^{\mathrm{T}}$, $N = 500$ was selected.

6.3.2 Neural Network Model for Wrench Prediction

External forces applied to a certain point of an attached tool lead to corresponding contact wrenches at the end effector. The aim was to estimate these wrenches ${}^{\mathrm{ee}}\mathbf{w}$ based on the measured joint torques $\Delta\boldsymbol{\tau}$, the current robot pose and the distance to the force application point, given in the input vector I. This estimation was performed by training a regression model on simulated data for a static case (Section 6.2.1) and retraining it with real training data (Section 6.2.2). A dense feed-forward neural network with fully connected layers was used. The optimal network architecture for the problem has been found by doing a hyperparameter optimization varying the number of layers, the regularizer, the loss function as well as the number of neurons. The neurons were modeled with rectified linear unit (ReLU) activation functions [129]. The last layer consists of six neurons to predict the wrench vector ${}^{\mathrm{ee}}\mathbf{f}$ with linear activation. The activation functions g_{ReLU} and g_{linear} are defined as:

$$g_{ReLU}(x) = max(0, x) \tag{6.18}$$

and

$$g_{linear}(x) = x. \tag{6.19}$$

The wrench vector is predicted by propagating the input through the layers of the network [130]. The relationship between ${}^{\mathrm{ee}}\mathbf{w}$ and the measured joint torques $\Delta\boldsymbol{\tau}$ is highly dependent on the robot's current joint configuration as well as the distance to the point of force application $\mathbf{r}_{\mathrm{com}}$ in the end effector coordinate system. One challenge was the identification of a suitable, unique representation of the robot's pose. It could be observed that the joint angles $\mathbf{q}_{\mathrm{i}}, i \in \{1, \dots, 7\}$, alone were not sufficient. Even by adding the end effector rotation and position as inputs, the model was not able to learn the problem and did not converge. The high redundancy of the robotic arm, especially the additional seventh DoF, greatly increases the complexity of the function to be learned. Therefore, the translational and rotational part of the homogenous pose matrices ${}^{ee}\mathbf{T}_{\mathrm{i}}, i \in \{1, \dots, 7\}$, of the individual joints regarding the end effector frame were also fed to the network model. This resulted in 12 additional parameters per joint, i.e. the nine rotational parameters $r_{\mathrm{i}}^{1}, \dots, r_{\mathrm{i}}^{9}$ and three translational parameters $\mathrm{t}_{i}^{1}, ..., \mathrm{t}_{i}^{3}$ for the i-th joint. The vector ${}^{0}\mathbf{M}'_{\mathrm{i}}$ was defined as the element-wise representation of the pose matrix ${}^{0}\mathbf{T}_{\mathrm{i}}$:

$$ {}^{0}\mathbf{M}'_{\mathrm{i}} = (r_{\mathrm{i}}^{1}, \dots, r_{\mathrm{i}}^{9}, \mathrm{t}_{\mathrm{i}}^{1}, \dots, \mathrm{t}_{\mathrm{i}}^{3}) \in \mathbb{R}^{12}, i \in \{1, \dots, 7\}. \tag{6.20} $$

Hence, the input I and the output O of the neural network can be written as:

$$ \begin{aligned} I =& (\mathbf{q}_{1}, ..., \mathbf{q}_{7}, \Delta\boldsymbol{\tau}_{1}, ..., \Delta\boldsymbol{\tau}_{7}, {}^{\mathrm{ee}}\mathbf{M}'_{1}, ..., {}^{\mathrm{ee}}\mathbf{M}'_{7}, \\ & r_{\mathrm{com,x}}, r_{\mathrm{com,y}}, r_{\mathrm{com,z}}) \in \mathbb{R}^{101}, \end{aligned} \tag{6.21} $$

$$ O = ({}^{\mathrm{ee}}\mathbf{f}_{\mathrm{x}}, {}^{\mathrm{ee}}\mathbf{f}_{\mathrm{y}}, {}^{\mathrm{ee}}\mathbf{f}_{\mathrm{z}}, {}^{\mathrm{ee}}\mathbf{m}_{\mathrm{x}}, {}^{\mathrm{ee}}\mathbf{m}_{\mathrm{y}}, {}^{\mathrm{ee}}\mathbf{m}_{\mathrm{z}}) \in \mathbb{R}^{6}. \tag{6.22} $$

The input I was normalized to have zero mean and a unified variance of 1 (zero centering). The model was implemented in *Python* using *Keras* [131] with the *Theano*-Backend [132].

Optimal network architecture

Firstly, a deep feed forward neural network was trained with the idealized simulated $dataset_{train,sim}$. To find an optimal network architecture for the problem of predicting end effector wrenches, an autonomous hyperparameter optimization was done using the *optuna* toolbox [133] and the LAMB optimizer [134]. In Table 6.3 the static as well as the varied neural network parameters and their ranges are listed. The loss function for training a particular neural network is an optimization parameter and can vary between mean squared error and mean absolute error (see Table 6.3). In order to compare the different tested network architectures with an equal metric to find the neural network with the highest prediction accuracy, a separate evaluation error using the root mean squared error was calculated. Training was done on four GPUs of a DGX-2. The resulting optimal neural network model with the highest prediction accuracy is named NN_{sim}.

Retraining with real training data

The optimized neural network model NN_{sim} resulted from a training process only done with simulated data representing an idealized static case. In a real scenario,

Table 6.3: Hyperparameter optimization - static and dynamic parameters

Parameter	Type	Value / Value range
layers	dynamic	1-20
neurons	dynamic	1-1000
L2 regularization	dynamic	$1e^{-20} - 1e^{-3}$
loss	dynamic	mean squared error, mean absolute error
epochs	static	500
batch size	static	6000
early stopping patience	static	1000

different inaccuracies like dissipative effects and measurement inaccuracies occur. In addition, the exact isolated torques $\Delta\boldsymbol{\tau}_{\mathrm{j}}$ generated by the specific calibration weights are unknown. Thus, the torques without mounted calibration weight $\boldsymbol{\tau}_0$ must be estimated first, using the proposed gravity compensation model from Section 6.3.1. Afterwards $\Delta\boldsymbol{\tau}_{\mathrm{j}}$ can be calculated according to Eq. (6.10).

To take into account the described inaccuracies, the model based on simulated data NN_{sim} was retrained with the real training $dataset_{train,real}$. This was done on a regular desktop PC, with an Intel core i7 CPU and an nVidia GeForce GTX 1060 GPU. The resulting model is named $NN_{retrain}$.

6.4 Evaluation of Accuracy

The goal is to precisely estimate gravity joint torques as well as contact wrenches at the end effector from given joint positions and torque data. A data-driven method based on linear regression is used to approximate the static gravity torques without any knowledge of the link masses nor the centers of gravity of the links. To estimate the end effector contact wrench, an extensive database, consisting of both simulated and real data, was acquired to develop and evaluate artificial neural network models. For generating real ground truth contact wrenches, ten specially manufactured weights in the range of 0-2 kg (0-20 N) were mounted to the end effector. By using the constant gravity force and different robot base orientations, a homogeneous representation of contact forces in all directions was realized. Due to various combinations of base orientations, calibration weights and robot poses, the database consists of 330,000 randomized data points. See Section 6.2.2 for more details. For evaluation purposes, the testing datasets (see Section 6.2.3 and Section 6.2.4) were used, which were not included in the training of the neural networks.

Firstly, the performance of the proposed gravity compensation model is evaluated in Section 6.4.1. Afterwards the capabilities of the neural network models to precisely estimate contact wrenches at the end effector are illustrated (Section 6.4.2) - even if another robot is used (Section 6.4.4).

6.4.1 Accuracy of Gravity Compensation Model

To determine the imaginary masses w_{i} by solving the overdetermined equation system in Eq. (6.17) 500 data points out of the $dataset_{train,real}$ without mounted calibration weights are used. Increasing the number of data points had not shown any relevant change of the results. The datapoints are taken in equal parts from the 6 different base orientations. The optimal solution is (values in N):

$$\begin{aligned}\mathbf{x} &= -g_0 \begin{pmatrix} w_1 & w_2 & w_3 & w_4 & w_5 & w_6 & w_7 \end{pmatrix}^{\mathrm{T}} \\ &= \begin{pmatrix} 0 & 0 & 74.56 & 0 & 47.1 & 0 & 7.85 \end{pmatrix}^{\mathrm{T}}.\end{aligned} \tag{6.23}$$

Dividing this through the negative gravity constant g_0 results in

$$\tilde{\mathbf{x}} = \begin{pmatrix} 0 & 0 & 7.6 & 0 & 4.8 & 0 & 0.8 \end{pmatrix}^{\mathrm{T}}, \tag{6.24}$$

for the imaginary masses w_{i} (values in kg). The result shows that only the parameters w_3, w_5 and w_7 have values not equal to zero. So in the proposed model, the gravity forces acting on the joint torques of the robot are generated only by three imaginary masses. These are located in joint 4 (robot elbow), joint 6 (robot hand) and in the end effector.

The determined imaginary masses w_{i} are now used to estimate the static gravity torques according to Eq. (6.17). The intra-directionality generalization dataset $dataset_{gen,dir}$ without mounted calibration weights is used for evaluation. Figure 6.5 shows the absolute errors for the estimated static gravity torques of the joints using the model. The absolute errors of the estimation of the robot's integrated proprietary force estimation model (PFEM) are also shown in Figure 6.5. The robot firmware does not directly output the estimated gravity torques, but the measured joint torques as well as the calculated external joint torques. So for a comparison with the proposed gravity compensation model, the external joint torques are used to calculate the absolute error. For a robot without any weight attached to the end effector, the external joint torques are lower the better the integrated model of the gravity compensation is. Figure 6.5 shows that the proposed gravity compensation model fits the zero torques in a static experiment slightly better than the integrated model of the robot manufacturer. Especially the median error of the zero torques for the second joint can be reduced from 1.0 N to 0.54 N (46 %). Moreover, the variability could be reduced, except for joint 5. For joint 5 also the median of the prediction error is 34 % higher using the proposed gravity compensation model. The proposed model seems to have difficulties in estimating the torque in joint 5 induced by the masses of the following links 5, 6, and 7. Theoretically there would be two imaginary masses m_5 and m_7 unequal to zero, which are located in joint 6 and the end effector and thus are taken into account for the computation of the fifth joint torque. But considering the equation to approximate $\tilde{\tau}_5$ in Eq. (6.17), the corresponding entry $\widetilde{\mathbf{J}}^{\mathrm{T}}_{\mathrm{m,z,5}}$, which is multiplied by m_5, equals zero. So only w_7 has an influence on approximating the gravity torque $\tilde{\tau}_5$, which explains the prediction inaccuracy.

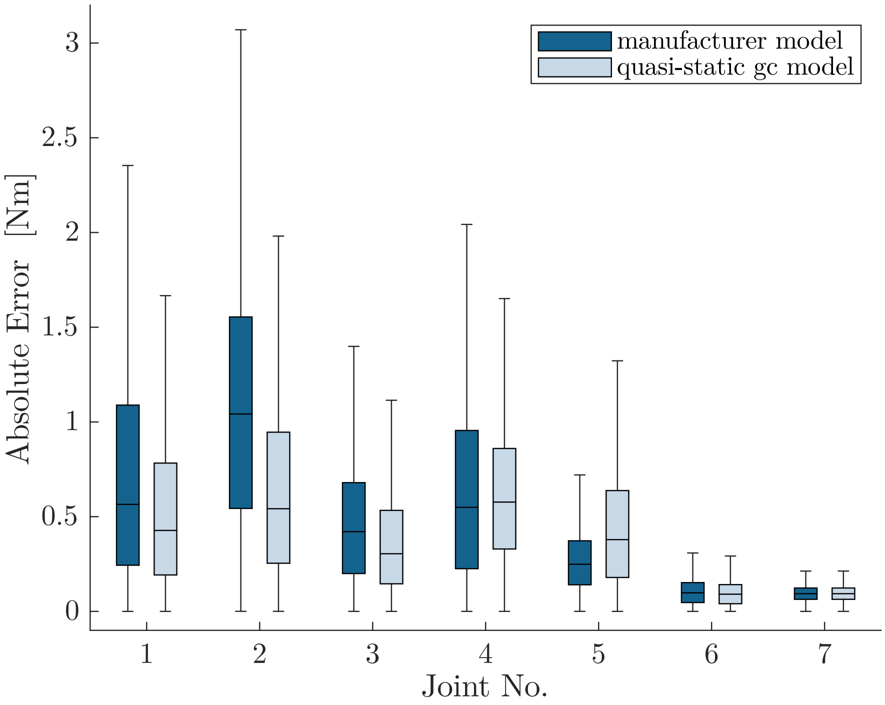

Figure 6.5: Absolute error of the proposed gravity compensation model compared to the model of the robot manufacturer, evaluated on the $dataset_{gen,dir}$.

The obtained results show the applicability of the presented approach to determine static gravity torques of a robot without knowing the inertial parameters of the links. It represents a simple to implement and time-saving option, since only joint torque data of a few randomly generated poses need to be acquired.

6.4.2 Accuracy of Contact Wrench Estimation

For evaluation purposes, the contact forces and moments acting at the end effector are considered separately. The prediction accuracies of the NN_{sim}, which was only trained with the simulated data for an ideal static case and the $NN_{retrain}$, which was retrained with the real $dataset_{train,real}$ are compared with the robot manufacture's PFEM model.

Optimal neural network architecture

To find the optimal network architecture for the estimation of contact wrenches, an autonomous hyperparameter optimization was done using the *optuna* toolbox [133] and the LAMB optimizer [134]. The simulated training dataset was divided into training (95 %) and validation data (5 %). In total, 700 different architectures were tested, which needed a computing time of approximately 19 days. After 514 iterations, the lowest validation error was found for a network architecture, consisting of 14 hidden layers with 681 neurons and an L2 regularization of 1.23e-06. The mean absolute error was used as loss function. The created network is referred to as NN_{sim}. On a regular desktop PC, with an Intel core i7 CPU and a low-cost GPU (nVidia GeForce GTX 1060), one evaluation step takes 21.5 ms. The evaluation time is thus quite high, which can be explained by the large size of the neural network. Depending on the application, this might have to be taken into account when choosing a network architecture. In the current setup assuming a static scenario, where is no or almost no movement of the robot when the force is estimated, the long evaluation time can be handled. Since slow movements are expected, the reaction time is not critical in this context. Moreover, when using a more recent mid-range GPU (nVidia GeForce RTX 3060), the evaluation time drops to 12.8 ms. This illustrates the considerable advances in hardware performance over time and suggests that inference delays may become less relevant for future applications.

Contact forces

Figure 6.6A shows the overall accuracy of the proposed calibration compared to the PFEM based on all measurements of the $dataset_{gen,rob}$ in a linear scale. The absolute error was calculated for the contact forces ${}^{\mathrm{ee}}\mathbf{f}$ for each axis separately. The calculation was based on the absolute difference between the ground truth (see Section 6.2.2) and the output of the trained neural network ${}^{\mathrm{ee}}\mathbf{f}_{\mathrm{ann}}$, as well as the measured contact forces given by the PFEM ${}^{\mathrm{ee}}\mathbf{f}_{\mathrm{fw}}$. By using the neural network model NN_{sim}, the median absolute error could be reduced by 0.53 N (26.0 %) for ${}^{\mathrm{ee}}f_{\mathrm{x}}$, 0.56 N (27.5 %) for ${}^{\mathrm{ee}}f_{\mathrm{y}}$, and 0.56 N (30.8 %) for ${}^{\mathrm{ee}}f_{\mathrm{z}}$. The retrained model $NN_{retrain}$ shows even better results. Here the median absolute error could be reduced by 1.32 N (65.0 %) for ${}^{\mathrm{ee}}f_{\mathrm{x}}$, 1.32 N (64.8 %) for ${}^{\mathrm{ee}}f_{\mathrm{y}}$, and 0.75 N (41.5 %) for ${}^{\mathrm{ee}}f_{\mathrm{z}}$.

Contact moments

Figure 6.6B shows the accuracy of the NN models compared to the PFEM. Again, the absolute error was calculated for the three axis separately. By using the neural network model NN_{sim}, the median absolute error could be slightly reduced by

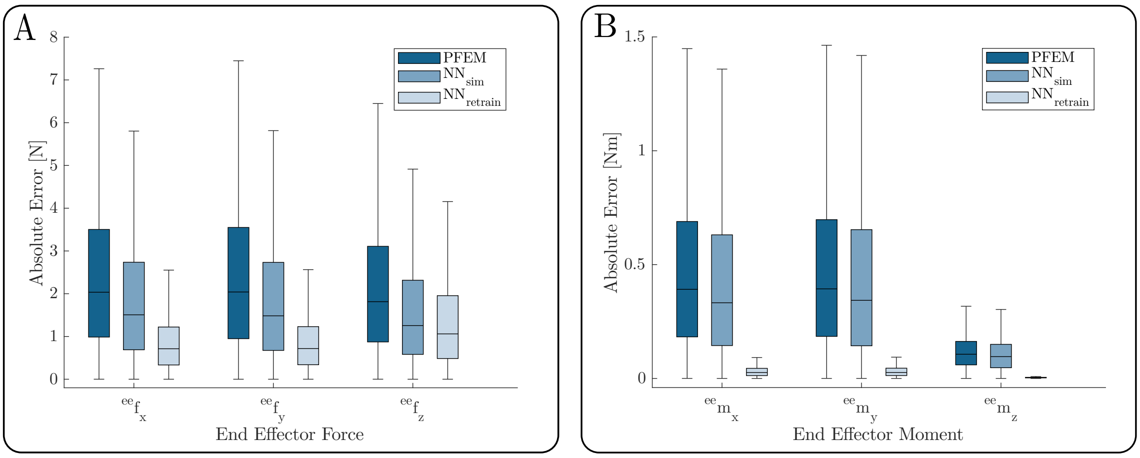

Figure 6.6: **(A)** Absolute end effector force error of the ANN approach compared to the PFEM given for each axis in linear scale evaluated on the $dataset_{gen,dir}$. The median error could be largely reduced by the ANN, which was retrained with real robot data. **(B)** Absolute end effector moment error of the ANN approach compared to the PFEM given for each axis in linear scale evaluated on the $dataset_{gen,dir}$.

0.06 Nm (15.1 %) for ${}^{ee}m_{\mathrm{x}}$, 0.05 Nm (12.7 %) for ${}^{ee}m_{\mathrm{y}}$ and 0.01 Nm (9.7 %) for ${}^{ee}m_{\mathrm{z}}$. In contrast, the retrained model $NN_{retrain}$ leads to a strong reduction of the end effector moment prediction errors. A reduction of 0.37 Nm (93.4 %) for ${}^{ee}m_{\mathrm{x}}$, 0.37 Nm (93.3 %) for ${}^{ee}m_{\mathrm{y}}$, and 0.10 Nm (96.4 %) for ${}^{ee}m_{\mathrm{z}}$ was achieved. The great difference to the predictions of the NN_{sim} as well as the PFEM could result from the corresponding scenario, where the moments acting at the end effector in the $dataset_{real}$ are solely generated by the contact-forces and the distance to the force application point. This is due to the experimental setup, where contact wrenches were induced by masses, which were pulled towards the ground by gravity. Thus, no additional external end effector moments were applied. As the neural network $NN_{retrain}$ was retrained with these experimental data, it shows a better prediction accuracy for the end effector moment as long as no additional external moments are applied.

It must also be noted that the ground truth for the contact moments is based in the center of mass of the metallic rod with the mounted calibration weights. These were determined from an appropriately created CAD model, so small uncertainties can possibly result. Nevertheless, it could be shown that the relationship between end effector forces, the distance to the force application point and corresponding end effector moments can be learned and precisely predicted by the neural network.

Due to the problematic issues pointed out regarding the contact moment, in the following chapters the accuracy of contact forces acting at the end effector is investigated in more detail. These are also of higher relevance for the intended application of precisely estimating the force acting on an US probe attached to the robot end effector.

6.4.3 Outlier Reduction

As shown in Figure 6.7A, a high number of large outliers in the PFEM data with maximum errors in the range of 10^4 N could be observed. These high errors are caused by numerical instabilities of the computational model used by the PFEM near singular configurations. In contrast, the proposed solution provides much more stable results than the integrated model.

In order to analyze the problems of incalculable contact forces at singular positions and numerical instabilities close to these positions in more detail, the contact force errors were considered as a function of the arm position. To acquire this, the manipulator's reach was used as a relevant parameter. The reach indicates how far the end effector is displaced from the shoulder. At maximum reach, the arm is therefore fully extended and in a singular configuration. Figure 6.7B shows the contact force root mean square error (RMSE) as a function of increasing reach. With an increasing reach over 700 mm, the error grows dramatically. In addition, the number and magnitude of outliers also rises massively. In contrast, the ANN data shows much more stable results. The outcome indicates that different arm positions have less impact on the model accuracy and, furthermore, that the model is capable of robustly handling singularities. Clearly, this is counterintuitive: Fundamental mathematical laws render contact forces incalculable at singularities since the matrix **J** from Eq. (2.8) becomes singular. Nevertheless, this does not mean that contact forces in singularities cannot be detected at all, it only means that specific contact forces may not generate torques in all joints, which, in turn, will result in large errors when trying to compute the contact forces. Given that the collected training data was generated randomly, it is exceedingly unlikely that the robot was ever moved to an *exactly* singular position, but rather that it often came *close* to one. This means that the model has learned to deal with close-to-singular matrices **J** and, obviously, is capable of compensating adequately. Nevertheless, this does not mean that the model can overcome mathematical impossibilities, it rather means that it is less susceptible to numerical instabilities occurring close to singular positions.

6.4.4 Transfer to another Robot

To examine the transferability of the approach to another robot, the accuracy of contact force estimation of the additional testing dataset, which has been acquired with the LBR iiwa 14, is shown in Figure 6.8A. By using the neural network model NN_{sim}, which was solely trained on simulated data for the robot geometry of the LBR iiwa 7, the median absolute error could be slightly reduced by 0.23 N (12.3 %) for ${}^{\mathrm{ee}}f_{\mathrm{x}}$, 0.21 N (10.9 %) for ${}^{\mathrm{ee}}f_{\mathrm{y}}$, and 0.16 N (9.5 %) for ${}^{\mathrm{ee}}f_{\mathrm{z}}$. By using the network $NN_{retrain}$, which was retrained with the real data of the LBR iiwa 7, the force errors could be reduced by 0.92 N (49.2 %) for ${}^{\mathrm{ee}}f_{\mathrm{x}}$, 0.95 N (49.4 %) for ${}^{\mathrm{ee}}f_{\mathrm{y}}$, and 0.79 N (47.3 %) for ${}^{\mathrm{ee}}f_{\mathrm{z}}$. Furthermore, the accuracy of the estimation of the contact moments can also be improved (Figure 6.8B). The retrained model $NN_{retrain}$ leads to a reduction of the end effector moment prediction errors. It must be noted that for the prediction of the contact moments, the same drawbacks as described in Section 6.4.2 arise due to the experimental setup used, which require further investigations.

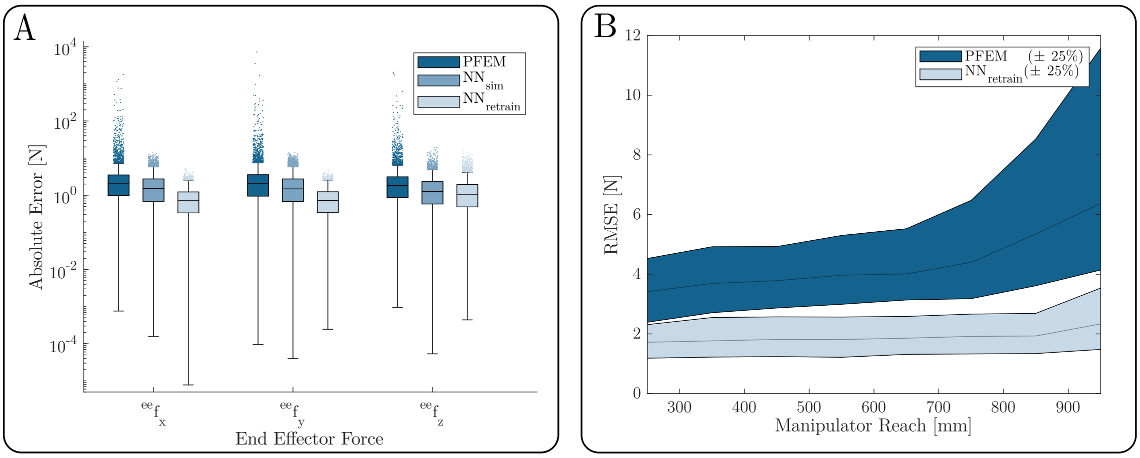

Figure 6.7: **(A)** Absolute end effector force error of the ANN approach compared to the PFEM given for each axis in logarithmic scale, evaluated on the $dataset_{gen,dir}$. The outliers could be largely reduced by the ANN approaches. **(B)** Contact force RMSE as a function of increasing manipulator reach in linear scale. A strongly rising error can be observed in the PFEM data from a reach above 700 mm.

However, it is shown that the estimation of the contact forces could be improved by the neural network models - even if another robot type is used. Especially the $NN_{retrain}$ can greatly reduce the force prediction errors. Once again it should be emphasized that no additional training data, neither simulated nor real, of the LBR iiwa 14 were used. Retraining on a small real calibration dataset acquired on this different robot would probably reduce the errors even more so that an accuracy similar to the experiments with the LBR iiwa 7 in Section 6.4.2 could be achieved. In this context, it must be noted that the experiments were done on a robot with the same degrees of freedom and thus the same size of input data. For a transfer to a robot with different degrees of freedom, the changed size of input data must be taken into account. It might be an option to just replace the input layer of the network for retraining.

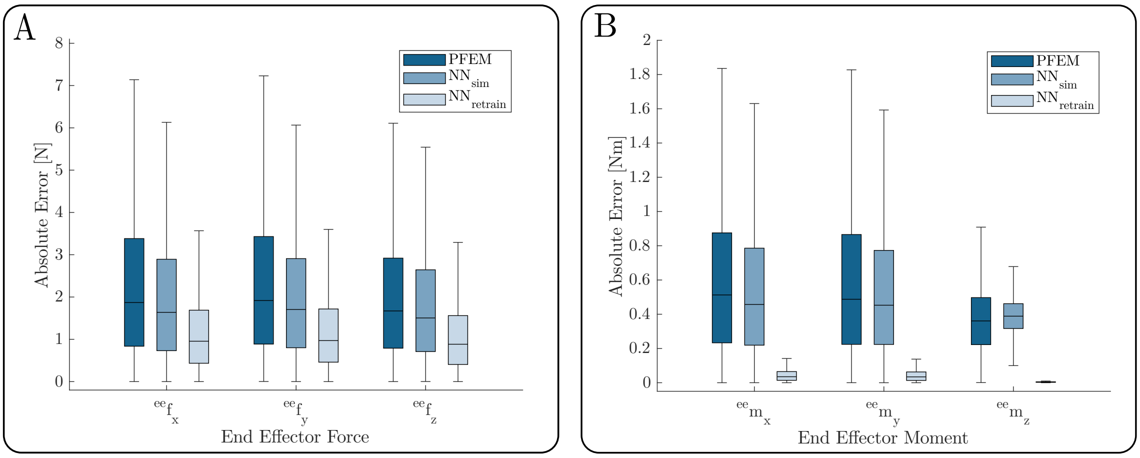

Figure 6.8: Absolute end effector force error **(A)** and moment error **(B)** of the ANN approach compared to the PFEM given for each axis in linear scale, evaluated on the transfer data of the LBR iiwa 14 $dataset_{transf}$.

6.5 Conclusion

The aim of this Chapter was to precisely determine corresponding contact wrenches at the end effector from given joint position and torque data of a redundant serial lightweight manipulator LBR iiwa 7. The results showed advantages of the proposed neural learning approach compared to the PFEM. Firstly, the new calibration method could increase the accuracy of end effector contact forces by 57.2 % and the accuracy of end effector contact moments by 90 % compared to the manufacturer's proprietary force estimation model. Secondly, it could be shown that the calibration stability could also be strongly increased with the proposed approach. In contrast to the PFEM, which revealed high outliers near singularities, the ANN approach showed robust results. The evaluation indicated that different arm positions do not affect the accuracy and, furthermore, the proposed model can robustly handle singularities.

After the promising results of this work, minor limitations remain. The calibration was performed in a limited force range of 0-20 N, which is far below the maximum loads of the manipulator. However, compliant robots are often used in specialized practical applications within limited load ranges. Moreover, the results show good generalization performance, even for estimation of the neural network, which was soley trained with simulated data. Thus, using a huge simulation dataset with an increased force range and a small real calibration dataset with larger distances between the calibration weights could be used. In addition, to further investigate the transferability of the method model to robots from other manufacturers, which have a more different geometry, should be tested. In this context, a transfer to a robot with different degrees of freedom and thus an input of a different size must also be considered. A robot specific simulated dataset could be generated easily for any robot whose geometric data are known. Afterwards, a few robot specific new recorded data points could be acquired and used for retraining and thus the prediction performance could be improved.

7

CONCLUSIONS, CHALLENGES & OUTLOOK

In this thesis, a robotic ultrasound system was developed, capable of performing automatic scans of the femoral artery for the diagnosis and therapy of PAD. Given the increasing prevalence of PAD and the growing burden on healthcare systems, particularly in industrialized nations with an aging population, such a system could increase diagnostic efficiency and reduce staff workload. The work addressed four research questions, with each question dealt with in a separate chapter (see Figure 7.1).

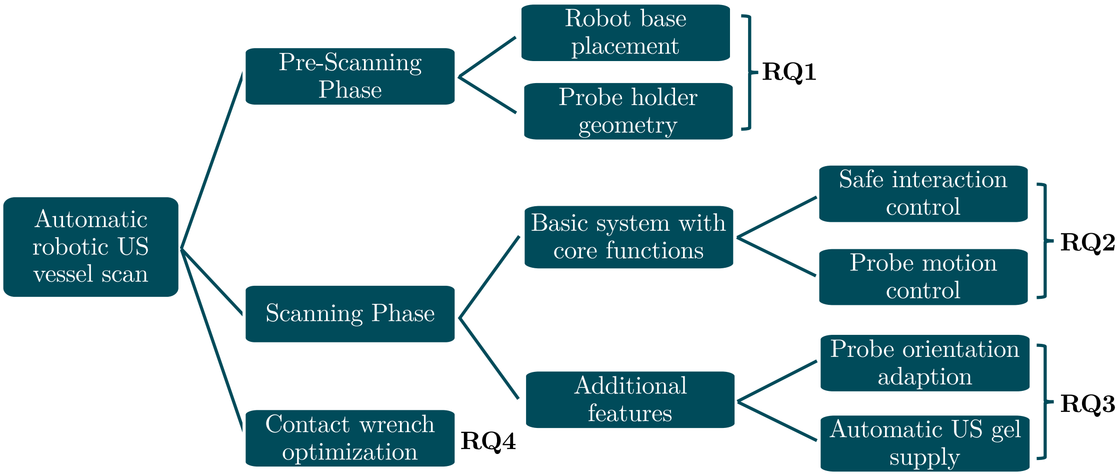

Figure 7.1: Structure of the thesis. The essential topics required for an automatic robotic US examination were addressed in individual chapters.

7.1 Robot-Patient Positioning

Firstly, in Chapter 3 the relationship between the geometry of the probe holder and the positioning of the robot in relation to the patient was investigated by **RQ1**.

> **Research Question 1**
> How can a probe holder be designed to maximize the reachability of target poses?

By determining adapted use-case specific probe holder geometries, it was ensured that the anatomical regions to be examined could be optimally reached. The design of the probe holder geometry was optimized by compensating for oblique orientations of the robot's base, which led to a higher reachability of target poses. The use of an appropriate probe holder geometry strongly increased the number of potential base placements with high reachability, especially in scenarios where the sixth joint of the robot works close to its limit to reach the target pose. This effect was particularly noticeable when the target position had to be reached from the opposite side of the patient. However, the optimal design of the probe holder geometry is highly dependent on the poses and environment of the target. Thus, an optimized one-size-fits-all solution is not possible. Rather, there is a trade-off between general flexibility of probe alignment on the one hand and maximum range and specific probe alignment on the other: A pure extension provides the greatest achievable flexibility for probe orientations. In contrast, angling the probe increases the translational reach. In addition, target orientations that require a large inclination angle aligned with the tool's angulation direction can be achieved more easily, while those oriented in the opposite direction are more difficult to reach. Consequently, it can be concluded that an adapted probe holder geometry for US robots that always perform the same procedure (e.g. scan of the leg artery) could be feasible and useful. Alternatively, a mechanism could also be considered where the mounting angle can be changed manually depending on the application, e.g. with a screw that can be tightened and loosened by hand. However, this requires the operator to correctly assess the target poses and the most suitable mounting angle, which is difficult in daily clinical practice. Another option for maximum flexibility in probe alignment and simultaneous enlargement of the workspace could be a motorized remote center mechanism [135] integrated into the probe holder. This would allow the probe orientation to be set independently of the robot's configuration. However, this is also associated with greatly increased system complexity and hence increased costs, which in turn represent barriers to implementation in clinics.

7.2 Automatic Robotic Doppler Sonography of Leg Arteries

In order to perform a successful automatic scan of a vessel, requirements for the robotic ultrasound system were categorized into mandatory core functions and additional features. The second research question focused on the development and validation of the core functions and was addressed in Chapter 4.

> **Research Question 2**
> How can the essential core functions of the robotic system be realized to enable a straightforward automatic US examination of the femoral artery?

A volunteer study was performed, demonstrating the feasibility of straightforward robotic US scans of leg arteries by fulfilling the core functions. An adapted interaction control scheme with an applied probe contact force was realized to ensure patient safety. To keep the artery centered while scanning, Doppler US has proven to be an effective option for artery tracking. Due to the ease of differentiation between veins and arteries based on the visualized blood flow color, false detection as occurring with purely image-based methods (e.g. template matching, or neural networks trained on US images) because of the similarity between veins and arteries can be avoided. For future work, it could be useful to combine Doppler Signal tracking with image-based methods of the US images. Thus, the respective advantages of the different approaches could be combined. In some cases, a Doppler signal may not be detected even if the vessel is clearly visible because the probe is not optimally aligned. In patients with occlusive arterial disease, the femoral arteries may also be insufficiently perfused, making it difficult or even impossible to detect a Doppler signal. The combination of image-based methods and Doppler signal tracking could enhance the resilience of vessel tracking under challenging visual conditions. The safe interaction control, employed in the experiments, delivered acceptable results for contact force accuracy, although no Cartesian force feedback was used. Integrating Cartesian force feedback could further increase the accuracy. This could be achieved by attaching an external force/torque sensor to the end effector. However, the associated increase in system complexity and costs may impact the feasibility of clinical integration. Alternatively, contact forces could be estimated based on measured external joint torques and the robot's dynamics model. To ensure safety and reliability, an improved contact wrench estimation model should be considered, as discussed in Chapter 6.

7.3 Additional Features for Robotic Ultrasound

The feasibility of robotic ultrasound scans of leg arteries by fulfilling the core functions was shown by the volunteer study. However, potential for improvement was identified to extend the application field of the robotic US system and increase the degree of automation. This requires the development of advanced approaches, which were in focus of research question **RQ3**.

> **Research Question 3**
> How can the additional features of automatic probe orientation adaption and US gel supply be integrated into the robotic US system?

Methods for a potential integration of the additional features have been developed in Chapter 5. Firstly, in Section 5.1 an approach to automatically adjust the probe's orientation was presented. Autonomous scanning of highly curved surfaces could be enabled. This would be necessary, for example, if the femoral artery was also to be examined down to the lower leg. For automatic probe orientation adaption, a CNN was trained to estimate the inclination of the probe's orientation towards the surface normal by analyzing the acquired 3D US volume as well as the end effector wrench. It was shown that unknown, highly curved surfaces can be scanned, and the probe orientation automatically adjusted in the direction of the approximate surface normal. However, it should be noted that the method was only tested on several known phantoms. Validation on unknown US phantoms and, in a second step, on volunteers in the form of a study, must be carried out. The generalizability of the approach was improved by cropping the data used to train CNN to the area of the US volume directly below the transducer. However, the appearance of this area differs considerably in phantoms and humans. In addition, the settings of the US device (e.g. probe model, depth, gains) as well as the amount of US gel applied, have a major influence. The reproducibility and hence the safety of the approach are therefore only guaranteed to a limited extent. A huge amount of training data with varying anatomies and US settings would have to be collected first to ensure safe use on humans.

In Section 5.2, a method for the automatic supply of US gel was proposed. The elbow rotation in the robot's nullspace was exploited in combination with a passive mechanism to automatically dispense US gel from a tube. The method was validated by two phantom experiments, which demonstrated that the movement for applying US gel did not affect the probe's target movement. Thus, the examination time for automatic long-term US examinations, where no staff can enter, could be greatly increased. The major advantage of this approach is that it is based on a simple and cheap 3D printable design, where no additional electronics are required, which would increase the system's complexity and cost. The seventh degree of freedom of the robot can be used effectively in combination with the push mechanism to dispense the US gel. However, there are also some drawbacks. The fixed attachment of the push mechanism to the link between joint 6 and joint 7 reduces the robot's maneuverability. This is particularly critical if free movement of the end effector around its z-axis is required. The presented method for automatic gel supply is therefore primarily suitable for previously known short, repetitive paths. Consequently, a potential useful application would be the automatic robotic acquisition of extensive US data sets, which are necessary for the training of neural networks, for instance. Challenging data acquisitions like this no longer depend on repeated manual renewal of the US gel, allowing for long-term studies and the generation of large datasets without human monitoring. For use in a realistic clinical setting, the strongly limited maneuverability of the robot is likely to be an issue. The simple design of the dispenser could principally be used well here with minor improvements - however, the lever for delivering the gel should be decoupled from the robot kinematics by an actuator to maintain the full flexibility of the robot.

7.4 Optimization of Contact Wrench Estimation

Accurate measurements of the wrench at the end effector of the robot are essential, not only for robotic US but any interaction task of the robot with its environment. The end effector wrenches are estimated using internal models of the robot manufacturers. Large errors can occur here, particularly in the proximity of singular configurations. Thus, Chapter 6 addressed the following research question, **RQ4**.

> **Research Question 4**
> How can the accuracy of the robot's wrench estimation as well as the robustness be increased in quasi-static scenarios?

A learning approach was proposed to train the dependencies between joint torques, which are measured in each of the robot's axes, and the end effector contact wrenches in Chapter 6. Thereby, the accuracy and robustness of the robot wrench estimation model could be increased. In particular, extreme outliers that occurred in the manufacturer's estimation model when the robot was close to singularities were greatly reduced. These errors could have drastic consequences, such as instability of the interaction controller or the application of mistakenly excessive contact forces, which can lead to patient injury. The proposed learning approach can therefore be used for more reliable redundant wrench estimation and increase the overall safety of the robotic system. However, some limitations remain here as well. The training data were acquired in a limited force range of 0-20 N, which is considerably lower than the maximum load capacity of the manipulator. However, for applications involving contact with humans, such as in ultrasound robotics, this range is typically sufficient, as only low interaction forces are required. For a broader applicability of the approach with a larger force range, the variance of the training data must be increased accordingly.

7.5 Outlook

Overall, the methods developed in this thesis represent a step towards future fully automated US examinations. However, a number of challenges still need to be overcome before such a system can be introduced into clinical practice.

Correct robot-patient positioning proved to be necessary before US scanning to completely and reliably cover the target area. In a clinical setting, the challenge arises to realize the calculated optimal robot-patient positioning. This requires either moving the robot base or instructing the patient to adjust their position relative to the robot accordingly. Both options involve further difficulties and need to be tested in a clinical setting. The smooth interaction between the robot and the patient or hospital staff is of particular importance here, as this has a major influence on the acceptance of such a system in daily clinical practice.

For the robotic US scan itself, it was demonstrated that a basic configuration incorporating core functions of the system provides effective results for the considered application of a femoral vessel scan. By developing additional features, the system can be further improved for specific applications, but it must always be critically assessed whether the benefits outweigh the associated risks of the features in terms of increased system complexity, comprehensibility, and therefore patient safety.

In addition, a fully automated US examination must also include a diagnosis after the US data acquisition, which needs to be developed in the next steps. The standardization of the movement sequence of the probe made possible by the robot might be advantageous, as it facilitates the use of data-driven methods, such as artificial intelligence, to evaluate the acquired data. Finally, by combining automatic US image acquisition and automatic evaluation for diagnosis, a fully autonomous US robot could be realized, which would greatly improve future patient care.

BIBLIOGRAPHY

[1] M. H. Criqui, K. Matsushita, V. Aboyans, *et al.*, “Lower Extremity Peripheral Artery Disease: Contemporary Epidemiology, Management Gaps, and Future Directions: A Scientific Statement From the American Heart Association”, *Circulation*, vol. 144, no. 9, 2021. DOI: `10.1161/CIR.0000000000001005`.

[2] H. Lawall, P. Huppert, and G. Rümenapf. “S3-leitlinie zur diagnostik, therapie und nachsorge der peripheren arteriellen verschlusskrankheit (pavk)”. Accessed: 2025-05-21. (2020), [Online]. Available: `https://register.awmf.org/de/leitlinien/detail/065-003`.

[3] M. S. Kim, J. Hwang, D. K. Yon, *et al.*, “Global burden of peripheral artery disease and its risk factors, 1990–2019: A systematic analysis for the Global Burden of Disease Study 2019”, *The Lancet Global Health*, vol. 11, no. 10, e1553–e1565, 2023. DOI: `10.1016/S2214-109X(23)00355-8`.

[4] James Paget University Hospitals NHS Foundation Trust, *Doppler ultrasound patient information*, Accessed: 2024-06-03, 2022. [Online]. Available: `https://www.jpaget.nhs.uk/media/116918/22-Doppler-Ultrasound.pdf`.

[5] D. Won, J. Walker, R. Horowitz, S. Bharadwaj, E. Carlton, and H. Gabriel, “Sound the Alarm: The Sonographer Shortage Is Echoing Across Healthcare”, *Journal of Ultrasound in Medicine*, vol. 43, no. 7, pp. 1289–1301, 2024. DOI: `10.1002/jum.16453`.

[6] OpenAI, *Chatgpt, version gpt-4o*, `https://chat.openai.com/`, KI-generiertes Bild, erstellt mit ChatGPT, 2025.

[7] M. R. Zemaitis, J. M. Boll, and M. A. Dreyer, “Peripheral Arterial Disease”, in *StatPearls*, Treasure Island (FL): StatPearls, 2023. [Online]. Available: `https://www.ncbi.nlm.nih.gov/books/NBK430745/` (visited on 10/29/2024).

[8] V. Aboyans, J.-B. Ricco, M.-L. E. L. Bartelink, *et al.*, “2017 ESC Guidelines on the Diagnosis and Treatment of Peripheral Arterial Diseases, in collaboration with the European Society for Vascular Surgery (ESVS)”, *European Heart Journal*, vol. 39, no. 9, pp. 763–816, 2018. DOI: `10.1093/eurheartj/ehx095`.

[9] C. Rammos, M. Steinmetz, J. Lortz, *et al.*, “Peripheral artery disease in Germany (2009-2018): Prevalence, frequency of specialized ambulatory care and use of guideline-recommended therapy - A population-based study”, *The Lancet Regional Health. Europe*, vol. 5, p. 100 113, 2021. DOI: `10.1016/j.lanepe.2021.100113`.

[10] P. S. Sidhu, C. Ewertsen, M. Piskunowicz, *et al.*, “Diversity of current ultrasound practice within and outside radiology departments with a vision for 20 years into the future: A position paper of the ESR ultrasound subcommittee”, *Insights into Imaging*, vol. 14, p. 202, 2023. DOI: `10.1186/s13244-023-01548-w`.

[11] T. L. Szabo, *Diagnostic Ultrasound Imaging: Inside Out.* Oxford, UK: Academic Press, 2013, ISBN: 978-0-12-396542-4.

[12] S. Afzal, M. Zahid, Z. A. Rehan, *et al.*, “Preparation and Evaluation of Polymer-Based Ultrasound Gel and Its Application in Ultrasonography”, *Gels*, vol. 8, no. 1, p. 42, 2022. DOI: `10.3390/gels8010042`.

[13] T. D. Mast, “Empirical relationships between acoustic parameters in human soft tissues”, *Acoustics Research Letters Online*, vol. 1, no. 2, pp. 37–42, 2000. DOI: `10.1121/1.1336896`.

[14] F. Mohamed and C. V. Siang, “A survey on 3d ultrasound reconstruction techniques”, in *Artificial Intelligence - Applications in Medicine and Biology*, 2019. DOI: `10.5772/intechopen.81628`.

[15] A. Fenster and D. Downey, “3-d ultrasound imaging: A review”, *IEEE Engineering in Medicine and Biology Magazine*, vol. 15, no. 6, pp. 41–51, 1996. DOI: `10.1109/51.544511`.

[16] P. Magee, “Essential notes on the physics of Doppler ultrasound”, *BJA Education*, vol. 20, no. 4, pp. 112–113, 2020. DOI: `10.1016/j.bjae.2020.01.003`.

[17] M. E. Cheung, V. Singh, and M. S. Firstenberg, “Duplex Ultrasound”, in *StatPearls*, Treasure Island (FL), USA: StatPearls, 2022. [Online]. Available: `https://www.ncbi.nlm.nih.gov/books/NBK459266/` (visited on 11/29/2024).

[18] D. Kohlman-Trigoboff, “Utility of the hand-held continuous wave Doppler in the vascular examination: A review”, *Journal of Vascular Nursing*, vol. 34, no. 4, pp. 160–162, 2016. DOI: `10.1016/j.jvn.2016.09.002`.

[19] B. Hoffmann, “5 Erweiterte Knopfologie (Farb-, PW-, CW-Doppler)”, in *Kursbuch Notfallsonografie*, 2., aktualisierte und erweiterte Auflage, Stuttgart, Germany: Georg Thieme Verlag KG, 2019. DOI: `10.1055/b-0039-168232`.

[20] Labster, *Continuous doppler - theory*, `https://theory.labster.com/continuous_doppler/`, Accessed: 2025-02-13.

[21] D. C. Taylor, “Duplex ultrasound in the assessment of vascular disease in clinical hypertension”, *American Journal of Hypertension*, vol. 4, no. 6, pp. 550–556, 1991. DOI: `10.1093/ajh/4.6.550`.

[22] A. Shah and A. Irshad, “Sonography Doppler Flow Imaging Instrumentation”, in *StatPearls*, Treasure Island (FL), USA: StatPearls, 2023. [Online]. Available: `http://www.ncbi.nlm.nih.gov/books/NBK580539/` (visited on 10/16/2024).

[23] E. Montini, F. Daniele, L. Agbomemewa, *et al.*, “Collaborative Robotics: A Survey From Literature and Practitioners Perspectives”, *Journal of Intelligent & Robotic Systems*, vol. 110, no. 3, p. 117, 2024. DOI: `10.1007/s10846-024-02141-z`.

[24] S. Haddadin, A. De Luca, and A. Albu-Schäffer, “Robot Collisions: A Survey on Detection, Isolation, and Identification”, *IEEE Transactions on Robotics*, vol. 33, no. 6, pp. 1292–1312, 2017. DOI: `10.1109/TRO.2017.2723903`.

[25] A. Albu-Schäeffer, S. Haddadin, C. Ott, A. Stemmer, T. Wimböck, and G. Hirzinger, “The DLR Lightweight Robot – Design and Control Concepts for Robots in Human Environments”, *Industrial Robot: The International Journal of Robotics Research and Application*, vol. 34, pp. 376–385, 2007. DOI: `10.1108/01439910710774386`.

[26] V. Chawda and G. Niemeyer, “Toward torque control of a KUKA LBR IIWA for physical human-robot interaction”, in *Proceedings of the 2017 IEEE/RSJ International Conference on Intelligent Robots and Systems (IROS)*, 2017, pp. 6387–6392. DOI: `10.1109/IROS.2017.8206543`.

[27] The MathWorks, Inc., *Robotics System Toolbox, Version R2024a*, `https://de.mathworks.com/products/robotics.html`, 2024.

[28] A. Albu-Schäffer, C. Ott, and G. Hirzinger, “A Unified Passivity Based Control Framework for Position, Torque and Impedance Control of Flexible Joint Robots”, *The International Journal of Robotics Research*, vol. 26, no. 1, pp. 23–39, 2007. DOI: `10.1177/0278364907073776`.

[29] R. Featherstone and D. E. Orin, “Dynamics”, in *Springer Handbook of Robotics*, B. Siciliano and O. Khatib, Eds., Berlin, Germany: Springer, 2016, pp. 35–65. DOI: `10.1007/978-3-540-30301-5_3`.

[30] Z. Ying and S. S. Iyengar, “Robot reachability problem: A nonlinear optimization approach”, *Journal of Intelligent and Robotic Systems*, vol. 12, no. 1, pp. 87–100, 1995. DOI: `10.1007/BF01258308`.

[31] T. Yoshikawa, “Manipulability of robotic mechanisms”, *The International Journal of Robotics Research*, vol. 4, no. 2, 1985. DOI: `10.1177/027836498500400201`.

[32] M. J. Tsai and Y. H. Chiou, “Manipulability of manipulators”, *Mechanism and Machine Theory*, vol. 25, no. 5, pp. 575–585, 1990. DOI: `10.1016/0094-114X(90)90071-Q`.

[33] F. Zacharias, C. Borst, and G. Hirzinger, “Capturing robot workspace structure: Representing robot capabilities”, in *Proceedings of the 2007 IEEE/RSJ International Conference on Intelligent Robots and Systems (IROS)*, 2007. DOI: `10.1109/IROS.2007.4399105`.

[34] A. Makhal and A. K. Goins, “Reuleaux: Robot base placement by reachability analysis”, in *Proceedings of the 2018 IEEE International Conference on Robotic Computing (IRC)*, 2018. DOI: `10.1109/IRC.2018.00028`.

[35] P. Nayyeri, K. Zareinia, and H. Bougherara, “MATLAB Toolbox for Reachability Analysis and Visualization of Robotic Manipulators”, in *Proceedings of the 2024 8th International Conference on Robotics and Automation Sciences (ICRAS)*, 2024, pp. 49–54. DOI: `10.1109/ICRAS62427.2024.10654471`.

[36] N. Vahrenkamp, T. Asfour, G. Metta, G. Sandini, and R. Dillmann, "Manipulability analysis", in *Proceedings of the 2012 IEEE-RAS International Conference on Humanoid Robots (Humanoids)*, 2012, pp. 568–573. DOI: `10.1109/HUMANOIDS.2012.6651576`.

[37] I. Kuhlemann, P. Jauer, F. Ernst, and A. Schweikard, "Robots with seven degrees of freedom: Is the additional DoF worth it?", in *Proceedings of the IEEE 2016 2nd International Conference on Control, Automation and Robotics (ICCAR)*, 2016. DOI: `10.1109/iccar.2016.7486703`.

[38] S. Stradovnik and A. Hace, "Workpiece Placement Optimization for Robot Machining Based on the Evaluation of Feasible Kinematic Directional Capabilities", *Applied Sciences*, vol. 14, no. 4, p. 1531, 2024. DOI: `10.3390/app14041531`.

[39] B. Balci, J. Donovan, J. Roberts, and P. Corke, "Optimal Workpiece Placement Based on Robot Reach, Manipulability and Joint Torques", in *Proceedings of the 2023 IEEE International Conference on Robotics and Automation (ICRA)*, 2023, pp. 12 302–12 308. DOI: `10.1109/ICRA48891.2023.10161031`.

[40] J. Osburg, N. T. Nguyen, and F. Ernst, "Increasing Reachability in Robotic Ultrasound Through Base Placement and Tool Design", *The International Journal of Medical Robotics and Computer Assisted Surgery*, vol. 21, no. 1, e70037, 2025. DOI: `10.1002/rcs.70037`.

[41] N. Vahrenkamp, T. Asfour, and R. Dillmann, "Robot placement based on reachability inversion", in *Proceedings of the 2013 IEEE International Conference on Robotics and Automation (ICRA)*, 2013, pp. 1970–1975. DOI: `10.1109/ICRA.2013.6630866`.

[42] O. Porges, R. Lampariello, J. Artigas, A. Wedler, C. Borst, and M. A. Roa, "Reachability and Dexterity: Analysis and Applications for Space Robotics", in *Workshop on advanced space technologies for robotics and automation-ASTRA*, 2015.

[43] F. Burget and M. Bennewitz, "Stance selection for humanoid grasping tasks by inverse reachability maps", in *Proceedings of the 2015 IEEE International Conference on Robotics and Automation (ICRA)*, 2015. DOI: `10.1109/ICRA.2015.7139993`.

[44] J. Dong and J. C. Trinkle, "Orientation-based reachability map for robot base placement", in *Proceedings of the 2015 IEEE/RSJ International Conference on Intelligent Robots and Systems (IROS)*, 2015. DOI: `10.1109/IROS.2015.7353564`.

[45] T. Birr, C. Pohl, and T. Asfour, "Oriented surface reachability maps for robot placement", in *Proceedings of the 2022 International Conference on Robotics and Automation (ICRA)*, 2022, pp. 3357–3363. DOI: `10.1109/ICRA46639.2022.9811600`.

[46] M. Sereinig, P. Manzl, and J. Gerstmayr, "Task-Dependent Comfort Zone, a Base Placement Strategy for Mobile Manipulators Based on Manipulability Measures", *Robotics*, vol. 13, no. 8, p. 122, 2024. DOI: `10.3390/robotics13080122`.

[47] A. Wachter, C. Hartl-Nesic, and A. Kugi, "Robot Base Placement Optimization for Pick-and-Place Sequences in Industrial Environments", *IFAC-PapersOnLine*, vol. 58, no. 19, pp. 19–24, 2024. DOI: `10.1016/j.ifacol.2024.09.080`.

[48] D. Spensieri, J. S. Carlson, R. Bohlin, J. Kressin, and J. Shi, "Optimal Robot Placement for Tasks Execution", *Procedia CIRP*, vol. 44, pp. 395–400, 2016. DOI: `10.1016/j.procir.2016.02.105`.

[49] C.-V. Ince, J. Schönburg, and A. Raatz, "Approach of Automated Robot Arrangement in Manufacturing Cells", *Procedia CIRP*, vol. 128, pp. 286–291, 2024. DOI: `10.1016/j.procir.2024.06.023`.

[50] K. Zbiss, A. Kacem, M. Santillo, and A. Mohammadi, "Automatic Optimal Robotic Base Placement for Collaborative Industrial Robotic Car Painting", *Applied Sciences*, vol. 14, no. 19, p. 8614, 2024. DOI: `10.3390/app14198614`.

[51] M. Toussaint, J.-S. Ha, and O. S. Oguz, "Co-optimizing robot, environment, and tool design via joint manipulation planning", in *Proceedings of the 2021 IEEE International Conference on Robotics and Automation (ICRA)*, 2021. DOI: `10.1109/ICRA48506.2021.9561256`.

[52] A. Filippeschi, P. Griffa, and C. A. Avizzano, "Kinematic optimization for the design of a collaborative robot end-effector for tele-echography", *Robotics*, vol. 10, no. 1, p. 8, 2021. DOI: `10.3390/robotics10010008`.

[53] S. Gerlach and A. Schlaefer, "Robotic systems in radiotherapy and radiosurgery", *Current Robotics Reports*, vol. 3, pp. 9–19, 2022. DOI: `10.1007/s43154-021-00072-3`.

[54] J. Schlosser, R. Gong, R. Bruder, *et al.*, "Robotic intrafractional us guidance for liver sabr: System design, beam avoidance, and clinical imaging", *Medical Physics*, vol. 43, no. 11, pp. 5951–5963, 2016. DOI: `10.1118/1.4964454`.

[55] SketchUp 3D Warehouse, *3d modell of linear accelerator (varian truebeam stx)*, `https://3dwarehouse.sketchup.com/model/u9d9c8922-fce6-4f94-8483-0c0b7bad6c39/Linear-Accelerator`, Accessed: July, 2023, 2023.

[56] E. B. Saff and A. B. J. Kuijlaars, "Distributing many points on a sphere", *The Mathematical Intelligencer*, vol. 19, 1997. DOI: `10.1007/BF03024331`.

[57] I. Kuhlemann, A. Schweikard, P. Jauer, and F. Ernst, "Robust inverse kinematics by configuration control for redundant manipulators with seven dof", in *Proceedings of the 2016 2nd International Conference on Control, Automation and Robotics (ICCAR)*, 2016. DOI: `10.1109/ICCAR.2016.7486697`.

[58] X.-Y. Zeng, Y.-H. Chuang, and C.-W. Chen, "Automatic instrument changer for robotic microsurgical systems", *IFAC-PapersOnLine*, vol. 53, no. 2, pp. 15 910–15 915, 2020, 21st IFAC World Congress. DOI: `10.1016/j.ifacol.2020.12.289`.

[59] J. Osburg, A. Scheibert, M. Horn, R. Pater, and F. Ernst, "Automatic robotic doppler sonography of leg arteries", *International Journal of Computer Assisted Radiology and Surgery*, vol. 19, no. 10, pp. 1965–1974, 2024. DOI: `10.1007/s11548-024-03235-7`.

[60] K. Li, Y. Xu, and M. Q.-H. Meng, "An overview of systems and techniques for autonomous robotic ultrasound acquisitions", *IEEE Transactions on Medical Robotics and Bionics*, vol. 3, no. 2, pp. 510–524, 2021. DOI: `10.1109/TMRB.2021.3072190`.

[61] F. von Haxthausen, S. Böttger, D. Wulff, J. Hagenah, V. García-Vázquez, and S. Ipsen, "Medical robotics for ultrasound imaging: Current systems and future trends", *Current Robotics Reports*, vol. 2, pp. 55–71, 2021. DOI: `10.1007/s43154-020-00037-y`.

[62] Z. Jiang, S. E. Salcudean, and N. Navab, "Robotic ultrasound imaging: State-of-the-art and future perspectives", *Medical Image Analysis*, vol. 89, p. 102 878, 2023. DOI: `10.1016/j.media.2023.102878`.

[63] Q. Huang, J. Zhou, and Z. Li, "Review of robot-assisted medical ultrasound imaging systems: Technology and clinical applications", *Neurocomputing*, vol. 559, 2023. DOI: `10.1016/j.neucom.2023.126790`.

[64] H. Du, X. Zhang, Y. Zhang, F. Zhang, L. Lin, and T. Huang, "A review of robot-assisted ultrasound examination: Systems and technology", *The International Journal of Medical Robotics and Computer Assisted Surgery*, vol. 20, no. 4, e2660, 2024. DOI: `10.1002/rcs.2660`.

[65] Y. Bi, Z. Jiang, F. Duelmer, D. Huang, and N. Navab, "Machine Learning in Robotic Ultrasound Imaging: Challenges and Perspectives", *Annual Review of Control, Robotics, and Autonomous Systems*, vol. 7, no. 1, pp. 335–357, 2024. DOI: `10.1146/annurev-control-091523-100042`.

[66] S. Merouche, L. Allard, E. Montagnon, G. Soulez, P. Bigras, and G. Cloutier, "A robotic ultrasound scanner for automatic vessel tracking and three-dimensional reconstruction of b-mode images", *IEEE Transactions on Ultrasonics, Ferroelectrics, and Frequency Control*, vol. 63, pp. 35–46, 2015. DOI: `10.1109/TUFFC.2015.2499084`.

[67] F. von Haxthausen, J. Hagenah, M. Kaschwich, M. Kleemann, V. García-Vázquez, and F. Ernst, "Robotized ultrasound imaging of the peripheral arteries - a phantom study", *CoRR*, vol. abs/2007.06278, 2020. DOI: `10.48550/arXiv.2007.06278`.

[68] F. von Haxthausen, T. Aust, H. Schwegmann, *et al.*, "Visual servoing for semi-automated 2d ultrasound scanning of peripheral arteries", in *Proceedings on Automation in Medical Engineering (AUTOMED)*, 2020. DOI: `10.18416/AUTOMED.2020`.

[69] A. Scheibert, M. Preuss, J. Osburg, F. Ernst, M. Kleemann, and M. Horn, “Robotic Assisted Ultrasound-Guided Endovascular Stent Implantation in a Vascular Model”, *The International Journal of Medical Robotics and Computer Assisted Surgery*, vol. 20, no. 6, e70005, 2024. DOI: `10.1002/rcs.70005`.

[70] Z. Jiang, Z. Li, M. Grimm, *et al.*, “Autonomous robotic screening of tubular structures based only on real-time ultrasound imaging feedback”, *IEEE Transactions on Industrial Electronics*, vol. 69, no. 7, pp. 7064–7075, 2022. DOI: `10.1109/TIE.2021.3095787`.

[71] Y. Huang, W. Xiao, C. Wang, H. Liu, R. Huang, and Z. Sun, “Towards fully autonomous ultrasound scanning robot with imitation learning based on clinical protocols”, *IEEE Robotics and Automation Letters*, vol. 6, no. 2, pp. 3671–3678, 2021. DOI: `10.1109/LRA.2021.3064283`.

[72] J. Xia, F. Deng, G. Yun, Q. Zhang, and Z. Liu, “Automatic ultrasound scanning for the Carotid Artery by robotic system”, in *Proceedings of the 2022 International Conference on Service Robotics (ICoSR)*, 2022, pp. 170–174. DOI: `10.1109/ICoSR57188.2022.00039`.

[73] X. Zhu, S. Lyu, X. Wang, and Q. Zhao, “TPH-YOLOv5: Improved YOLOv5 Based on Transformer Prediction Head for Object Detection on Drone-captured Scenarios”, in *Proceedings of the 2021 IEEE/CVF International Conference on Computer Vision Workshops (ICCVW)*, 2021. DOI: `10.1109/ICCVW54120.2021.00312`.

[74] Q. Huang, B. Gao, and M. Wang, “Robot-Assisted Autonomous Ultrasound Imaging for Carotid Artery”, *IEEE Transactions on Instrumentation and Measurement*, vol. 73, pp. 1–9, 2024. DOI: `10.1109/TIM.2024.3353836`.

[75] Z. Wang, Y. Han, B. Zhao, *et al.*, “Autonomous Robotic System for Carotid Artery Ultrasound Scanning With Visual Servo Navigation”, *IEEE Transactions on Medical Robotics and Bionics*, pp. 1436–1447, 2024. DOI: `10.1109/TMRB.2024.3464109`.

[76] D. Huang, C. Yang, M. Zhou, A. Karlas, N. Navab, and Z. Jiang, “Robot-Assisted Deep Venous Thrombosis Ultrasound Examination Using Virtual Fixture”, *IEEE Transactions on Automation Science and Engineering*, pp. 1–12, 2024. DOI: `10.1109/TASE.2024.3351076`.

[77] K. Su, J. Liu, X. Ren, *et al.*, “A fully autonomous robotic ultrasound system for thyroid scanning”, *Nature Communications*, vol. 15, no. 1, p. 4004, 2024. DOI: `10.1038/s41467-024-48421-y`.

[78] M. Chen, Y. Huang, J. Chen, T. Zhou, J. Chen, and H. Liu, “Fully robotized 3d ultrasound image acquisition for artery”, in *Proceedings of the 2023 IEEE International Conference on Robotics and Automation (ICRA)*, 2023, pp. 2690–2696. DOI: `10.1109/ICRA48891.2023.10161148`.

[79] A. I. Chen, M. L. Balter, T. J. Maguire, and M. L. Yarmush, “Deep learning robotic guidance for autonomous vascular access”, *Nature Machine Intelligence*, vol. 2, no. 2, pp. 104–115, 2020. DOI: `10.1038/s42256-020-0148-7`.

[80] Z. Jiang, F. Duelmer, and N. Navab, “Dopus-net: Quality-aware robotic ultrasound imaging based on doppler signal”, *IEEE Transactions on Automation Science and Engineering*, pp. 1–14, 2023. DOI: `10.1109/TASE.2023.3277331`.

[81] F. von Haxthausen, S. Ipsen, H. Schwegmann, R. Bruder, F. Ernst, and V. García-Vázquez, “A 3d slicer module for calibration of spatially tracked 3d ultrasound probes”, *International Journal of Computer Assisted Radiology and Surgery*, vol. 15, pp. 14–16, 2020. DOI: `10.1007/s11548-020-02171-6`.

[82] C. Wu, T. fu, X. Chen, *et al.*, “Automatic spatial calibration of freehand ultrasound probe with a multilayer n-wire phantom”, *Ultrasonics*, vol. 128, p. 106 862, 2022. DOI: `10.1016/j.ultras.2022.106862`.

[83] B. Mathieu, C. Claire, L. Lorenzo, and V. Arturo, “Temporal and spatial calibration of a freehand 3d ultrasound reconstructions system by using an n-wire phantom”, in *Proceedings of the 2015 12th International Conference on Electrical Engineering, Computing Science and Automatic Control (CCE)*, 2015, pp. 1–7. DOI: `10.1109/ICEEE.2015.7357966`.

[84] J. Schlosser, C. Kirmizibayrak, V. Shamdasani, S. Metz, and D. Hristov, “Automatic 3d ultrasound calibration for image guided therapy using intramodality image registration”, *Physics in medicine and biology*, vol. 58, pp. 7481–7496, 2013. DOI: `10.1088/0031-9155/58/21/7481`.

[85] P. Jauer, I. Kuhlemann, R. Bruder, A. Schweikard, and F. Ernst, “Efficient registration of high-resolution feature enhanced point clouds”, *IEEE Transactions on Pattern Analysis and Machine Intelligence*, vol. 41, no. 5, pp. 1102–1115, 2019. DOI: `10.1109/TPAMI.2018.2831670`.

[86] Piur Imaging, *Piur tus infinity*, Accessed: 2024-01-08. [Online]. Available: `https://piurimaging.com/piur-tus-infinity/`.

[87] S. R. Buss and J.-S. Kim, “Selectively Damped Least Squares for Inverse Kinematics”, *Journal of Graphics Tools*, vol. 10, no. 3, pp. 37–49, 2005. DOI: `10.1080/2151237X.2005.10129202`.

[88] A. Deo and I. Walker, “Robot subtask performance with singularity robustness using optimal damped least-squares”, in *Proceedings of the 1992 IEEE International Conference on Robotics and Automation (ICRA)*, 1992, pp. 434–441. DOI: `10.1109/ROBOT.1992.220301`.

[89] A. Lasso, T. Heffter, A. Rankin, C. Pinter, T. Ungi, and G. Fichtinger, “PLUS: Open-source toolkit for ultrasound-guided intervention systems”, *IEEE transactions on bio-medical engineering*, vol. 61, no. 10, pp. 2527–2537, 2014. DOI: `10.1109/TBME.2014.2322864`.

[90] Bon Secours Health System, *Peripheral artery ultrasound*, Accessed: 2024-06-03, 2024. [Online]. Available: `https://www.bonsecours.com/health-care-services/heart-care-cardiology/treatments/peripheral-artery-ultrasound`.

[91] J. Osburg, D. Wulff, and F. Ernst, “Generalized Automatic Probe Alignment based on 3D Ultrasound”, *Current Directions in Biomedical Engineering*, vol. 8, no. 1, pp. 58–61, 2022. DOI: `10.1515/cdbme-2022-0015`.

[92] M. R. Burcher, J. A. Noble, L. Han, and M. Gooding, “A system for simultaneously measuring contact force, ultrasound, and position information for use in force-based correction of freehand scanning”, *IEEE Transactions on Ultrasonics, Ferroelectrics, and Frequency Control*, vol. 52, no. 8, pp. 1330–1342, 2005. DOI: `10.1109/TUFFC.2005.1509791`.

[93] A. Scorza, S. Conforto, C. D’Anna, and S. A. Sciuto, “A comparative study on the influence of probe placement on quality assurance measurements in b-mode ultrasound by means of ultrasound phantoms”, *The Open Biomedical Engineering Journal*, vol. 9, pp. 164–178, 2015. DOI: `10.2174/1874120701509010164`.

[94] B. Ihnatsenka and A. P. Boezaar, “Ultrasound: Basic understanding and learning the language”, *International Journal of Shoulder Surgery*, vol. 4, no. 3, pp. 55–62, 2010. DOI: `10.4103/0973-6042.76960`.

[95] P. Chatelain, A. Krupa, and N. Navab, “Confidence-driven control of an ultrasound probe”, *IEEE Transactions on Robotics*, vol. 33, no. 6, pp. 1410–1424, 2017. DOI: `10.1109/TRO.2017.2723618`.

[96] Z. Jiang, H. Wang, Z. Li, *et al.*, “Motion-Aware Robotic 3D Ultrasound”, in *Proceedings of the 2021 IEEE International Conference on Robotics and Automation (ICRA)*, 2021, pp. 12 494–12 500. DOI: `10.1109/ICRA48506.2021.9561487`.

[97] G. Ma, S. R. Oca, Y. Zhu, P. J. Codd, and D. M. Buckland, “A Novel Robotic System for Ultrasound-guided Peripheral Vascular Localization”, in *Proceedings of the 2021 IEEE International Conference on Robotics and Automation (ICRA)*, 2021, pp. 12 321–12 327. DOI: `10.1109/ICRA48506.2021.9561924`.

[98] X. Ma, Z. Zhang, and H. K. Zhang, “Autonomous Scanning Target Localization for Robotic Lung Ultrasound Imaging”, in *Proceedings of the 2021 IEEE/RSJ International Conference on Intelligent Robots and Systems (IROS)*, 2021, pp. 9467–9474. DOI: `10.1109/IROS51168.2021.9635902`.

[99] X. Ma, W.-Y. Kuo, K. Yang, A. Rahaman, and H. K. Zhang, “A-SEE: Active-Sensing End-Effector Enabled Probe Self-Normal-Positioning for Robotic Ultrasound Imaging Applications”, *IEEE Robotics and Automation Letters*, vol. 7, no. 4, pp. 12 475–12 482, 2022. DOI: `10.1109/LRA.2022.3218183`.

[100] P. Chatelain, A. Krupa, and N. Navab, “Optimization of ultrasound image quality via visual servoing”, in *Proceedings of the 2015 IEEE International Conference on Robotics and Automation (ICRA)*, 2015, pp. 5997–6002. DOI: `10.1109/ICRA.2015.7140040`.

[101] Z. Jiang, N. Danis, Y. Bi, *et al.*, “Precise Repositioning of Robotic Ultrasound: Improving Registration-Based Motion Compensation Using Ultrasound Confidence Optimization”, *IEEE Transactions on Instrumentation and Measurement*, vol. 71, pp. 1–11, 2022. DOI: `10.1109/TIM.2022.3200360`.

[102] A. Karamalis, W. Wein, T. Klein, and N. Navab, “Ultrasound confidence maps using random walks”, *Medical Image Analysis*, vol. 16, no. 6, pp. 1101–1112, 2012. DOI: `10.1016/j.media.2012.07.005`.

[103] Z. Jiang, M. Grimm, M. Zhou, *et al.*, “Automatic normal positioning of robotic ultrasound probe based only on confidence map optimization and force measurement”, *IEEE Robotics and Automation Letters*, vol. 5, no. 2, pp. 1342–1349, 2020. DOI: `10.1109/LRA.2020.2967682`.

[104] J. Osburg and F. Ernst, “Nullspace Control for Automatic Ultrasound Gel Supply”, *Current Directions in Biomedical Engineering*, vol. 10, no. 2, pp. 45–48, 2024. DOI: `10.1515/cdbme-2024-1063`.

[105] D. Raina, Z. Zhao, R. Voyles, J. Wachs, S. K. Saha, and S. H. Chandrashekhara, “UltraGelBot: Autonomous Gel Dispenser for Robotic Ultrasound”, in *Proceedings of the 16th Hamlyn Symposium on Medical Robotics 2024*, 2024, pp. 119–120. DOI: `10.31256/HSMR2024.60`.

[106] H. Hanafusa, T. Yoshikawa, and Y. Nakamura, “Analysis and Control of Articulated Robot Arms with Redundancy”, *IFAC Proceedings Volumes*, vol. 14, no. 2, pp. 1927–1932, 1981. DOI: `10.1016/S1474-6670(17)63754-6`.

[107] S. Chiaverini, “Singularity-robust task-priority redundancy resolution for real-time kinematic control of robot manipulators”, *IEEE Transactions on Robotics and Automation*, vol. 13, no. 3, pp. 398–410, 1997. DOI: `10.1109/70.585902`.

[108] J. Osburg, I. Kuhlemann, J. Hagenah, and F. Ernst, “Using Deep Neural Networks to Improve Contact Wrench Estimation of Serial Robotic Manipulators in Static Tasks”, *Frontiers in Robotics and AI*, vol. 9, 2022. DOI: `10.3389/frobt.2022.892916`.

[109] H. Sadjadian, H. Taghirad, and A. Fatehi, “Neural networks approaches for computing the forward kinematics of a redundant parallel manipulator”, *International Journal of Computational Intelligence*, vol. 2, no. 1, pp. 40–47, 2005.

[110] D. R. Raj, I. J. Raglend, and M. D. Anand, “Inverse kinematics solution of a five joint robot using Feed forward and Elman network”, in *Proceedings of the 2015 International Conference on Circuit, Power and Computing Technologies (ICCPCT)*, 2015, pp. 1–5. DOI: `10.1109/ICCPCT.2015.7159376`.

[111] N. Kumar, V. Panwar, N. Sukavanam, S. Sharma, and J.-H. Borm, “Neural network-based nonlinear tracking control of kinematically redundant robot manipulators”, *Mathematical and Computer Modelling*, vol. 53, no. 9-10, pp. 1889–1901, 2011. DOI: `10.1016/j.mcm.2011.01.014`.

[112] R.-J. Lian, “Adaptive self-organizing fuzzy sliding-mode radial basis-function neural-network controller for robotic systems”, *IEEE Transactions on Industrial Electronics*, vol. 61, no. 3, pp. 1493–1503, 2014. DOI: `10.1109/TIE.2013.2258299`.

[113] S. Li, Y. Zhang, and L. Jin, “Kinematic control of redundant manipulators using neural networks”, *IEEE transactions on neural networks and learning systems*, vol. 28, no. 10, pp. 2243–2254, 2017. DOI: `10.1109/TNNLS.2016.2574363`.

[114] P. K. Khosla and T. Kanade, “Parameter identification of robot dynamics”, in *Proceedings of the 1985 24th IEEE Conference on Decision and Control*, 1985, pp. 1754–1760. DOI: `10.1109/CDC.1985.268838`.

[115] J. M. Hollerbach, W. Khalil, and M. Gautier, “Model identification”, in *Springer Handbook of Robotics*, B. Siciliano and O. Khatib, Eds., Berlin, Germany: Springer, 2008, pp. 321–344. DOI: `10.1007/978-3-540-30301-5_15`.

[116] M. Gautier and A. Jubien, “Force calibration of KUKA LWR-like robots including embedded joint torque sensors and robot structure”, in *Proceedings of the 2014 IEEE/RSJ International Conference on Intelligent Robots and Systems (IROS)*, 2014, pp. 416–421. DOI: `10.1109/IROS.2014.6942593`.

[117] N. Kumar, V. Panwar, N. Sukavanam, S. P. Sharma, and J.-H. Borm, “Neural network based hybrid force/position control for robot manipulators”, *International Journal of Precision Engineering and Manufacturing*, vol. 12, no. 3, pp. 419–426, 2011. DOI: `10.1007/s12541-011-0054-3`.

[118] H.-L. Pei, Q.-J. Zhou, and T. P. Leung, “A Neural Network Robot Force Controller”, in *Proceedings of the 1992 IEEE/RSJ International Conference on Intelligent Robots and Systems (IROS)*, vol. 3, 1992, pp. 1974–1979. DOI: `10.1109/IROS.1992.601929`.

[119] S. Jung, S. B. Yim, and T. C. Hsia, “Experimental studies of neural network impedance force control for robot manipulators”, in *Proceedings of the 2001 IEEE International Conference on Robotics and Automation (ICRA)*, vol. 4, 2001, pp. 3453–3458. DOI: `10.1109/ROBOT.2001.933152`.

[120] T.-F. Lu, G. C. Lin, and J. R. He, “Neural-network-based 3D force/torque sensor calibration for robot applications”, *Engineering Applications of Artificial Intelligence*, vol. 10, no. 1, pp. 87–97, 1997. DOI: `10.1016/S0952-1976(96)00069-3`.

[121] A. C. Smith, F. Mobasser, and K. Hashtrudi-Zaad, “Neural-Network-Based Contact Force Observers for Haptic Applications”, *IEEE Transactions on Robotics*, vol. 22, no. 6, pp. 1163–1175, 2006. DOI: `10.1109/TRO.2006.882923`.

[122] S. Wang, X. Shao, L. Yang, and N. Liu, “Deep learning aided dynamic parameter identification of 6-dof robot manipulators”, *IEEE Access*, vol. 8, pp. 138 102–138 116, 2020. DOI: `10.1109/ACCESS.2020.3012196`.

[123] M. Lutter, C. Ritter, and J. Peters, “Deep lagrangian networks: Using physics as model prior for deep learning”, in *Proceedings of the 7th International Conference on Learning Representations (ICLR)*, 2019. [Online]. Available: `https://openreview.net/pdf?id=BklHpjCqKm`.

[124] T.-C. Çallar and S. Böttger, “Hybrid Learning of Time-Series Inverse Dynamics Models for Locally Isotropic Robot Motion”, *IEEE Robotics and Automation Letters*, vol. 8, no. 2, pp. 1061–1068, 2023. DOI: `10.1109/LRA.2022.3222951`.

[125] Y. Tao, S. Chen, H. Liu, J. Wan, H. Wei, and T. Wang, “Robot hybrid inverse dynamics model compensation method based on the BLL residual prediction algorithm”, *Robotica*, pp. 1–18, 2024. DOI: `10.1017/S0263574724001905`.

[126] S. Kružić, J. Musić, R. Kamnik, and V. Papić, “End-effector force and joint torque estimation of a 7-dof robotic manipulator using deep learning”, *Electronics*, vol. 10, no. 23, 2021. DOI: `10.3390/electronics10232963`.

[127] G. Schreiber, A. Stemmer, and R. Bischoff, “The Fast Research Interface for the KUKA Lightweight Robot”, in *Workshop on IEEE ICRA 2010 Workshop on Innovative Robot Control Architectures for Demanding (Research) Applications - How to Modify and Enhance Commercial Controllers*, 2010, pp. 15–21.

[128] C. Yu, Z. Li, and H. Liu, “Research on gravity compensation of robot arm based on model learning”, in *Proceedings of the 2019 IEEE/ASME International Conference on Advanced Intelligent Mechatronics (AIM)*, 2019, pp. 635–641. DOI: `10.1109/AIM.2019.8868673`.

[129] V. Nair and G. E. Hinton, “Rectified linear units improve restricted boltzmann machines”, in *Proceedings of the 27th International Conference on Machine Learning (ICML)*, 2010, pp. 807–814.

[130] D. E. Rumelhart, G. E. Hinton, and R. J. Williams, “Learning representations by back-propagating errors”, *Nature*, vol. 323, pp. 533–536, 1986. DOI: `10.1038/323533a0`.

[131] F. Chollet *et al.*, *Keras*, `https://keras.io`, 2015.

[132] Theano Development Team, “Theano: A Python framework for fast computation of mathematical expressions”, *arXiv:1605.02688*, 2016. [Online]. Available: `https://doi.org/10.48550/arXiv.1605.02688`.

[133] T. Akiba, S. Sano, T. Yanase, T. Ohta, and M. Koyama, “Optuna: A next-generation hyperparameter optimization framework”, in *Proceedings of the 25rd ACM SIGKDD International Conference on Knowledge Discovery and Data Mining*, 2019. DOI: `10.1145/3292500.3330701`.

[134] Y. You, J. Li, J. Hseu, X. Song, J. Demmel, and C. Hsieh, “Reducing BERT pre-training time from 3 days to 76 minutes”, in *Proceedings of the 8th International Conference on Learning Representations (ICLR)*, vol. abs/1904.00962, 2020. DOI: `10.48550/arXiv.1904.00962`.

[135] S. Aksungur, “Remote Center of Motion (RCM) Mechanisms for Surgical Operations”, *International Journal of Applied Mathematics, Electronics and Computers*, vol. 3, no. 2, p. 119, 2015. DOI: `10.18100/ijamec.84097`.

LIST OF OWN PUBLICATIONS

[1] **J. Osburg**, I. Kuhlemann, J. Hagenah and F. Ernst, ‘Using Deep Neural Networks to Improve Contact Wrench Estimation of Serial Robotic Manipulators in Static Tasks’, *Frontiers in Robotics and AI*, vol. 9, 2022. doi:10.3389/frobt.2022.892916

[2] **J. Osburg**, D. Wulff and F. Ernst, ‘Generalized Automatic Probe Alignment Based on 3D Ultrasound’, *Current Directions in Biomedical Engineering*, vol. 8, no. 1, pp. 58–61, 2022. doi:10.1515/cdbme-2022-0015

[3] **J. Osburg**, F. Ernst, ‘Nullspace Control for Automatic Ultrasound Gel Supply’, *Current Directions in Biomedical Engineering*, vol. 10, no. 2, pp. 45–48, 2024. doi:10.1515/cdbme-2024-1063

[4] F. Ernst, **J. Osburg** and L. Tüshaus, ‘SonoBox: Development of a Robotic Ultrasound Tomograph for the Ultrasound Diagnosis of Paediatric Forearm Fractures’, *Frontiers in Robotics and AI*, vol. 11, 2024. doi:10.3389/frobt.2024.1405169

[5] **J. Osburg**, A. Scheibert, M. Horn, R. Pater and F. Ernst, ‘Automatic Robotic Doppler Sonography of Leg Arteries’, *International Journal of Computer Assisted Radiology and Surgery*, vol. 19, no. 10, pp. 1965–1974, 2024. doi:10.1007/s11548-024-03235-7

[6] A. Scheibert, M. Preuss, **J. Osburg**, F. Ernst, M. Kleemann and M. Horn, ‘Robotic Assisted Ultrasound-Guided Endovascular Stent Implantation in a Vascular Model’, *The International Journal of Medical Robotics and Computer Assisted Surgery*, vol. 20, no. 6, p. e70005, 2024. doi:10.1002/rcs.70005

[7] **J. Osburg**, N. T. Nguyen and F. Ernst, ‘Increasing Reachability in Robotic Ultrasound Through Base Placement and Tool Design’, *The International Journal of Medical Robotics and Computer Assisted Surgery*, vol. 21, no. 1, p. e70037, 2025. doi:10.1002/rcs.70037

LIST OF ABBREVIATIONS

ABI	Ankle Brachial Index.
ANN	Artificial Neural Network.
CAD	Computer Aided Design.
CNN	Convolutional Neural Network.
CTA	Computed Tomography Angiography.
CW	Continous Wave (Doppler US).
DoF	Degrees of Freedom.
IRM	Inverse Reachability Map.
LINAC	Medical Linear Accelerator.
MRI	Magnetic Resonance Imaging.
PAD	Peripheral Arterial Disease.
pAVK	Periphere Arterielle Verschlusskrankheit.
PFEM	Proprietary Force Estimation Model.
PW	Pulsed Wave (Doppler US).
ReLU	Rectified Linear Unit.
RM	Reachability Map.
RMSE	Root Mean Square Error.
RQ	Research Question.
TCP	Tool Center Point.
US	Ultrasound Imaging.

LIST OF FIGURES

LIST OF TABLES

DECLARATION OF GENERATIVE AI

Language support tools such as ChatGPT and DeepL Write were employed to enhance the linguistic quality of this thesis. All resulting content has been critically reviewed and edited and remains the full responsibility of the author.